Intraprotein electron transfer reactions facilitated by aromatic amino acids and their protein microenvironments

by

William Shen

B.Sc. (Hons.), Simon Fraser University, 2018

Thesis Submitted in Partial Fulfillment of the
Requirements for the Degree of
Master of Science

in the
Department of Chemistry
Faculty of Science

SIMON FRASER UNIVERSITY
SUMMER 2021

Declaration of Committee

Name:	**William Shen**
Degree:	**Master of Science (Chemistry)**
Title:	**Intraprotein electron transfer reactions facilitated by aromatic amino acids and their protein microenvironments**
Committee:	**Chair:** **Hogan Yu** Professor, Chemistry
	Jeffrey J. Warren Supervisor Associate Professor, Chemistry
	Dipankar Sen Committee Member Professor, Molecular Biology and Biochemistry
	Tim Storr Committee Member Professor, Chemistry
	Lisa Craig Examiner Professor, Molecular Biology and Biochemistry

Abstract

Intraprotein electron transfer processes are crucial to the maintenance of cellular pathways that enable life as we know. Well-studied and well-characterized proteins such as cytochrome *c* and azurin have long been used to explore these processes. The pathways present in these proteins and others, while varying in length can include covalent bonds, hydrogen bonds, and through-space jumps. Of interest are interactions in yeast cytochrome *c* that are similar to hydrogen bonds. We aimed to explore a pathway where the hydroxyl of Tyr67 interacts with the Met80 sulfur. To probe the importance of the interaction in the context of electron transfer, Tyr67 was replaced with different fluorotyrosines of varying pK_as. We then evaluated a second pathway containing two hydrogen bonds of which were removed by mutating to different amino acids. The elimination of these hydrogen bonds did not influence the rate of intramolecular electron transfer so an alternative pathway was examined. From this pathway, a substitution to Met64 to increase the length of a through-space jump decreased the electron transfer rate by a factor of two suggesting the initial pathway is non-operative. Lastly, the protein, azurin, was used as a model to investigate the properties of unnatural fluorotyrosines. The Trp48 amino acid was replaced with various fluorotyrosines in order to develop a system where the unnatural amino acid properties can be probed in relation to electron transfer processes.

Keywords: electron transfer, hydrogen bonds, cytochrome c, azurin, unnatural amino acids

Dedication

In loving memory of my mom who passed away in 2021. The woman who inspires me every day and whose love and support has afforded me the ability to be sitting here typing this.

Rest in paradise forever.

Acknowledgements

Big shoutout and thank you to my senior supervisor, Dr. Jeff Warren for giving me the opportunity to join the group then as an undergraduate student and now as a graduate student. I can't say that my journey could have been made any easier with all the help and guidance you've given over the many years. From your willingness to answer my periodic bombardment of questions to dropping all your work in the office to come down into the lab to help find something or to help with an experiment. It seems as though your dedication to your students knows no bounds. Your ability to put out metaphorical fires is appreciated. Though I have learned and gained so much in the lab, you encourage me to pursue my dreams and passions outside the walls of the lab as well. Your patience and accommodating nature had allowed me to spend extra time with my mom, time that was priceless and memories of which I will never forget. Here's to you for not teaching your students to sink or swim, but to rather build rafts together.

To my committee members, Prof. Dipankar Sen and Prof. Tim Storr, thank you for your invaluable time and support throughout the years. Your feedback and encouragement has been confidence-inspiring in carrying out the work I do.

To members of the Warren group past and present, thank you for never allowing a moment of dullness in the lab. To Ellan Berdichevsky, who showed me the ropes and everything I needed when I first started all those years ago. Big thanks to Samuel Hanson, Soumalya Sinha, Jessica Miller, David Weber, Femi Olawale, Michael Aaron, Curtis Gibbs, Rui Zhang, Elahe Tajbakhsh, Ana Sonea, Brooklyn Fedoretz-Maxwell, Catherine Shin, Jonathan Hui, Kaitlin Branch, Richard Hoang, Daina Baker, Moumita Ghosh, and Hannah van der Roest for the endless entertainment in the lab.

To Catherine for always being by my side throughout this wild journey and with it, all the ups and all the downs. For being my cheerleading squad during the stressful periods both inside and outside the lab.

To my dad who has sacrificed and given so much to the family in ways I may never fully appreciate. You have afforded me the privilege of not only pursuing an undergraduate degree but a graduate degree.

To my mom, while it seems like our time together was too short and you weren't able to witness the end of this chapter, I couldn't have done any of this without you. I am spoiled to be in a situation where it seems like there wasn't a day that had gone by when you weren't making sure I had everything I needed. I won't forget the early morning rides to the SkyTrain station and the late-night pickups when the busses stopped running even after you finished work late. While I had hoped that you and I would finish our degrees together this year and that you would be afforded the opportunity to pursue your own graduate degree, this degree was just as much yours. You continue to inspire me every day with your selflessness and the countless lives you have changed past, present, and future. May your memory live on forever.

Table of Contents

List of Tables

List of Figures

List of Acronyms

A	Acceptor
aaRS	Aminoacyl-transfer ribonucleic acid synthetase
azu	Azurin gene
bp	Base pair
BeStSel	Beta Structure Selection
CD	Circular dichroism
CDNN	Circular Dichroism analysis using Neural Networks
CM	Carboxymethyl
CV	Cyclic voltammetry
CYC1	Iso-1-cytochrome *c* gene
Cyt *c*	Cytochrome *c*
D	Donor
DNA	Deoxyribonucleic acid
DPV	Differential pulse voltammetry
DTT	Dithiothreitol
e^-	Electron
E. coli	*Escherichia coli*
EDTA	Ethylenediaminetetraacetic acid
EPR	Electron paramagnetic resonance
ET	Electron transfer
3-F-Tyr	3-fluorotyrosine
2,3-F_2-Tyr	2,3-difluorotyrosine
3,5-F_2-Tyr	3,5-difluorotyrosine
2,3,5-F_3-Tyr	2,3,5-trifluorotyrosine
2,3,5,6-F_4-Tyr	2,3,5,6-tetrafluorotyrosine
F_n-Tyr	Fluorotyrosine
FPLC	Fast protein liquid chromatography
H^+	Proton
IPTG	Isopropyl β-D-1-thiogalactopyranoside
ITO	Indium tin oxide
LB	Luria-Bertani broth
LB2YE	Luria-Bertani broth with two times yeast extract broth

MALDI-TOF	Matrix-assisted laser desorption/ionization-time of flight
MCS	Multiple cloning site
MS	Mass spectrometry
NHE	Normal hydrogen electrode
NMR	Nuclear magnetic resonance
P. aeruginosa	*Pseudomonas aeruginosa*
PCR	Polymerase chain reaction
PMSF	Phenylmethylsulfonyl fluoride
Q	Quencher
Redox	Reduction-oxidation
S. cerevisiae	*Saccharomyces cerevisiae*
SDS-PAGE	Sodium dodecyl sulfate-polyacrylamide gel electrophoresis
TA	Transient absorption
TB	Terrific broth
TPL	Tyrosine phenol-lyase
Tris	Tris(hydroxymethyl)aminomethane
TFA	Trifluoroacetic acid
tRNA	Transfer ribonucleic acid
U	Unit
UV	Ultraviolet
UV–Vis	Ultraviolet–Visible
WT	Wild-type
WT*	Pseudo-wild-type

Chapter 1.

Introduction

1.1. Electron transfer (ET) in biological systems

Reduction-oxidation (redox) reactions are responsible for life on Earth. Two excellent examples of this statement are water oxidation (to dioxygen) by photosynthetic plants[1,2] and the reduction of dioxygen to water by respiring cells.[3,4] Both reactions employ large, multi-subunit metalloproteins in reactions that interconvert O_2 and H_2O. The reactions of the substrates are representative redox reactions involving 4 protons (H^+) and 4 electrons (e^-), but there is a cascade of numerous intra- and inter-protein electron transfer steps in each system. Control over each ET event is crucial to function and off-pathway redox reactions can underlie diseases ranging from arthritis to dementia.[5] The central importance of biological ET has spurred numerous investigations involving biomolecules and related models, which is the research area of this thesis.

Our understanding of biological ET has continued to develop in ever-increasing detail during the past 50 years. Cytochrome *c* (cyt *c*) from *Saccharomyces cerevisiae*, a well-studied, soluble, small globular protein that is localized in the mitochondria is an excellent example in this regard. It participates in the eukaryotic electron transport chain by shuttling electrons between cyt *c* reductase and cyt *c* oxidase.[6] Early experiments (in the 1920s and 1930s) showed that the protein was redox-active and by the late 1960's the cyt *c* reduction potential was established.[7] However, it was in the early 1970s when the reactions of cyt *c* with other redox partners were systematically investigated.[8,9] Soon thereafter, interprotein ET reactions began to be investigated in earnest.[10] Similar to cyt c, azurin from *Pseudomonas aeruginosa* is another well-characterized, soluble protein involved in ET. Known as a blue copper protein, it localizes in the periplasmic space and is involved in the denitrification process in bacteria.[11] A summary of some of this very important early work in protein ET is available in Marcus and Sutin's influential review.[12]

1.2. Semi-classical theory of electron transfer and its application to proteins

The starting point for analyzing most ET reactions between a donor (D) and an acceptor (A) is the semi-classical ET rate expression (Equation 1.1, colloquially called "Marcus theory"). Equation 1.1 describes the rate constant for a unimolecular ET reaction in terms of the driving force ($-\Delta G°$), the degree of nuclear reorganization in D, A, and the surrounding solvent (λ), and the amount of coupling between the donor and acceptor (H_{DA}). The value of H_{DA} is dependent upon the D-A distance and the nature of the intervening medium. Equation 1.1 is, in fact, a combination of a modified version of the Arrhenius rate equation and Marcus' description of the activation energy in terms of λ. A concise derivation is given elsewhere.[13]

$$k_{ET} = \sqrt{\frac{4\pi^3}{h^2 \lambda k_B T}} H_{DA}^2 exp\left\{-\frac{(\Delta G° + \lambda)^2}{4\lambda k_B T}\right\} \quad (1.1)$$

One important term in Equation 1.1 is the electronic coupling matrix element, H_{DA}. In many cases, a simple, square-barrier tunneling model is used to understand H_{DA} (Equation 1.2).[14] Here, H_{DA}^0 and r_0 correspond to the close-contact values, typically taken as 3 Å for r_0 (roughly the van der Waals contact distance) and 186 cm^{-1}. The value of r is the net separation between donor and acceptor. The variable β is called the "distance decay constant" and is a characteristic of a homogeneous medium. Most media have a distinct value of β (e.g., Figure 1.1), ranging from ~4$Å^{-1}$ for a resistive medium, like a vacuum, to ~0.5 $Å^{-1}$ for a conductive medium, like oligophenylene "wires."

$$H_{DA} = H_{DA}^0 exp\left\{-\frac{1}{2}\beta(r - r_0)\right\} \quad (1.2)$$

Those early bimolecular reactions of cyt *c* and other proteins, mentioned above, were analysed with a simplified form of equation 1.1 referred to as the Marcus cross relation (Equation 1.3), which is readily derived from the Marcus additivity postulate.[12,15] The cross relation gives the rate constant for D-A ET in terms of the degenerate self-exchange rate constants (k_{DD} and k_{AA}) and the reaction equilibrium constant (K_{DA}). This form of Marcus theory is more appropriate for investigations of bimolecular ET reactions, provided that the transmission coefficients and work terms associated with the component reactions cancel (which is typically the case). The successful application of the cross

relation for protein ET was an early indication that semi-classical theory was applicable to redox reactions of biomolecules and launched an enormous effort focused on understanding ET in proteins.[12]

$$k_{DA} = \sqrt{k_{DD} k_{AA} K_{DA} f} \tag{1.3}$$

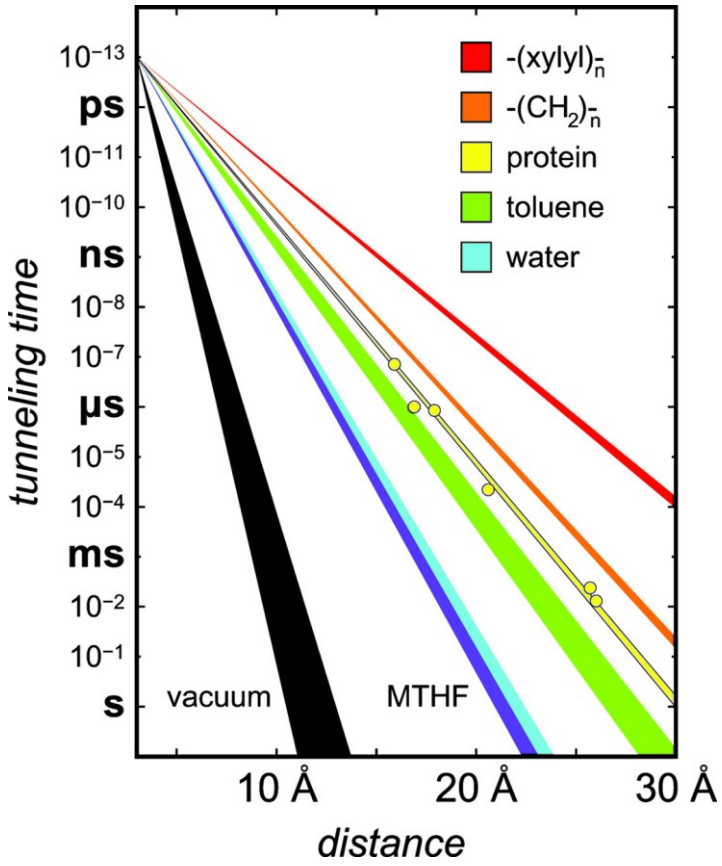

Figure 1.1. Tunneling timetable for activationless ($-\Delta G° = \lambda$) ET through different media. The values of the distance decay constant (β) are: 0.76 $Å^{-1}$ (red, $(xylyl)_n$ bridges), 1.0 $Å^{-1}$ (orange, aliphatic bridges), 1.1 $Å^{-1}$ (yellow, a protein β-strand, each point is a distinct model with different D-A separation), 1.18-1.28 $Å^{-1}$ (green, toluene glass), 1.55-1.65 $Å^{-1}$ (cyan, aqueous glass), 1.57-1.67 $Å^{-1}$ (purple, 3-methyl tetrahydrofuran glass) and 2.9-4.0 $Å^{-1}$ (black, vacuum). Reproduced with permission from Ref. [16]. Copyright 2005 National Academy of Sciences.

A rigorous analysis of ET in proteins requires understanding the separation between D and A. Initial work focused on using observed rate constants to establish D-A distances in the precursor complexes required for bimolecular ET reactions.[17] However, the simplest way in which to investigate ET in proteins at a fixed distance is to develop intraprotein redox probes. Small redox proteins modified with ruthenium redox probes first

emerged in the early 1980s.[18,19] These original models occurred at low driving forces. While this is common in biological systems, testing the relative importance of the variables in Equation 1.1 is difficult and requires many assumptions.

To address the above deficiencies, new protein models were developed. The first used cyt *c* with the iron in the heme substituted with Zn.[20] Zinc-porphyrins are photoactive and can be a strong reductant in its excited state and a strong oxidant as a radical cation. These pioneering experiments, and related ones,[21] suggested that the reorganization energy (λ) of cyt *c* was near 1 eV. The use of Zn porphyrin as a redox reagent is, however, limiting and cannot be extended to other metalloproteins or even many types of heme proteins.

The discovery that $[Ru(bpy)_2]^{2+}$ fragments could selectively bind the surface of histidine in metalloproteins[22] opened the door to a great many experiments.[23,24] Importantly, this labeling strategy could be applied to other proteins and the redox properties of Ru allow access to strong oxidants (via Ru^{3+}) and reductants. Investigation of ET rates in a series of Ru-modified cyt *c* demonstrated the variability in k_{ET} that motivated the development of ET pathway models.[25] Specifically, the inhomogeneity in k_{ET} refers to the deviation in observed rate constants from the expected.

1.3. The flash-quench technique for studying electron transfer

The use of protein-appended photosensitizers has allowed for the investigation of a wide range of intraprotein ET reactions. For the work described here, an “oxidative” flash-quench scheme was used (Figure 1.2). Here, a short pulse of laser light (i.e., from a Nd:YAG laser, ~7 ns) is used to excite a protein-appended ruthenium tris(diimine) photosensitizer (Ru^{2+}). The electronically excited Ru sensitizer (denoted $*Ru^{2+}$) donates an electron to a quencher, Q, that is present in large excess (at least 100-fold for the experiments described here). The large excess of Q ensures that the short-lived $*Ru^{2+}$ is efficiently converted (quenched) to Ru^{3+}. The resultant Ru^{3+} oxidant accepts an electron from the protein-embedded metal site. The Q^- generated in the quenching step can then return an electron to the protein metal site, completing the flash-quench cycle. In cases where the back reaction of Q^- + Ru^{3+} is faster than the intraprotein ET reaction, an irreversible quencher can be used. One common choice is $ClCo(NH_3)_5^{2+}$, which is

irreversible because the Co^{2+} product of the quenching reaction is substitutionally very labile. Note that a cycle employing an electron-donating quencher can be used to generate a reducing (formally) Ru^{1+} reductant as a means to study hole transfer from oxidized protein metal sites.[26]

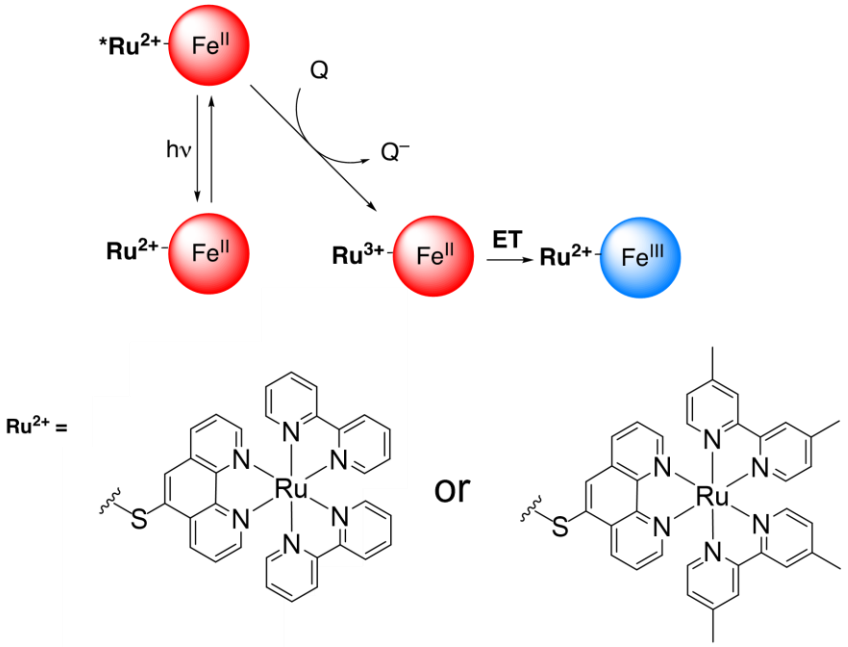

Figure 1.2. Schematic of the flash-quench scheme used in this thesis. The coloured circles represent the protein. Q is an electron-accepting quencher (e.g., $Ru(NH_3)_6^{3+}$ or $ClCo(NH_3)_5^{2+}$).

1.4. Pathway model for electron transfer in proteins

Most D-A ET reactions in proteins do not occur along a continuous protein strand. Once again, the pre-factor term H_{DA} in Equation 1.1 depends on the net distance and the nature of the medium between D and A. This means that for any two distinct points (i.e., D and A), there can be distinct routes with different components and distances along which a transferring electron could travel. Hopfield's square barrier model (see above) assumes that the composition of the medium between a donor and acceptor is uniform. In practice, and especially in proteins, this is not necessarily a good assumption. Halpern and Orgel,[27] and soon thereafter McConnell,[28] put forth a superexchange model where the overall electronic coupling depends on the degree of coupling between the donor and bridge, the acceptor and bridge, between the bridge subunits, and the energy gap between the donor and the bridge. These ideas were foundational and the elaboration of intraprotein ET systems (see above) was instrumental in the development of modern "pathway" models.

Beratan and Ohnuchic developed a self-consistent, parameterized pathway model that describes the electronic coupling matrix elements in terms of the components of the medium between donor and acceptor (Equation 1.3),

$$H_{DA} \propto \Pi_i \epsilon_C(i) \Pi_j \epsilon_S(j) \Pi_k \epsilon_H(k) \quad (1.3)$$

where $\varepsilon_C(i)$ corresponds to the number of covalent bonds, $\varepsilon_S(j)$ corresponds to the number of through-space jumps, and $\varepsilon_H(k)$ corresponds to the number of hydrogen bonds.[29–31] Given a known protein structure, computational search algorithms can be used to find pathways with maximum values of H_{DA}. One example of the success of this model is for ET reactions in different variants of Ru-modified cyt *c* where the Ru-label was located at different distances from the heme. The observed rates were anomalously slow based on predictions using the linear D-A edge-to-edge distance (i.e., a square barrier model). However, application of the pathway model showed that an ET route, and therefore the magnitude of H_{DA}, via through-bond pathways was consistent with the observed rate constants, k_{ET}.[32] More recent work, coupled with dramatic advances in computing power, use a related model and molecular dynamics simulations to probe how protein dynamics influence H_{DA}.[33]

1.5. Instrumental and biochemical techniques

1.5.1. Pyridine hemochromogen assay

The pyridine hemochromogen assay is a technique based on the initial discovery by G.G. Stokes in 1863 where he reduced hemoglobin in blood under the presence of ammonia.[34] Following reduction of heme *b* to the Fe(II) form, he observed intense α and β bands. It was later discovered by R. Hill that the nitrogen from two pyridines can bind axially to the heme forming the pyridine hemochromogen.[35,36] Further research at room temperature and under neutral pH conditions has confirmed that other exogenous ligands with nitrogen donors can substitute with the axially coordinated iron-sulfur from Met80 including imidazole and azide.[37–40]

To carry out the pyridine hemochromogen assay to determine the concentration of a solution of cyt *c*, a solution of pyridine, potassium ferricyanide, and sodium hydroxide is first prepared. Pyridine replaces both axial ligands on the heme iron. Potassium

ferricyanide acts as an oxidant to ensure the cyt *c* is in the Fe(III) form initially while sodium hydroxide is used to stabilize the sodium dithionite later added. To this solution, the yeast cyt *c* of interest is added and the Fe(III) spectra recorded. Upon mixing, the iron's axially ligated His18 and Met80 are replaced by the nitrogenous base, pyridine. Solid sodium dithionite is then added to reduce the heme to Fe(II) and the spectra are again recorded. The absorbance profile of the reduced Fe(II) spectrum is then subtracted from the oxidized Fe(III) spectrum. The new difference spectrum which is based on two pyridines axially ligating to the Fe is then used to calculate the concentration of the protein-based on reported extinction coefficients for the pyridine hemochromogen complex. The composition of the heme's surroundings was found to be negligible despite *c*-type cytochromes being covalently bound to the protein in comparison with *a*-type and *b*-type.[41]

1.5.2. Circular dichroism (CD) spectroscopy

Circular dichroism spectroscopy in relation to proteins is based on the principle of passing left and right-handed circularly polarized light through the sample of interest and determining the differential absorption. The peptide backbone is optically active so depending on their conformation, the CD spectra obtained in the far-ultraviolet (UV) region allow for the interpretation and estimation of protein secondary structure. The profile for α-helices shows a positive band at 193 nm and two negative bands at 208 and 222 nm.[42] With β-sheets, a positive band at 195 nm and a negative band at 218 nm are typical.[43] Seemingly disordered proteins, on the other hand, exhibit a negative band around 195 nm and little ellipticity at wavelengths greater than 210 nm.[44] A wide range of software is available for analyzing CD spectra many of which rely on the assumption that the spectra are a linear combination of all the different secondary structure elements.[45–49]

1.5.3. Electrochemistry

There is a multitude of electrochemical techniques for analyzing electrochemical processes in biological proteins. Cyclic voltammetry (CV), a commonly used technique is based on cycling an applied potential and measuring the current response. Typically, a three-electrode setup is used consisting of a working electrode, reference electrode, and a counter electrode. The working electrode can apply a potential to the system that is measured based on the reference electrode. During this process, the counter electrode completes the circuit with the working electrode. In Figure 1.3, the CV excitation signal is

cycled from more positive to negative potentials linearly with time. At a certain predefined potential, the cycle will reverse the direction of the scan to the initial potential and repeat. The current response is measured throughout the CV excitation signal.

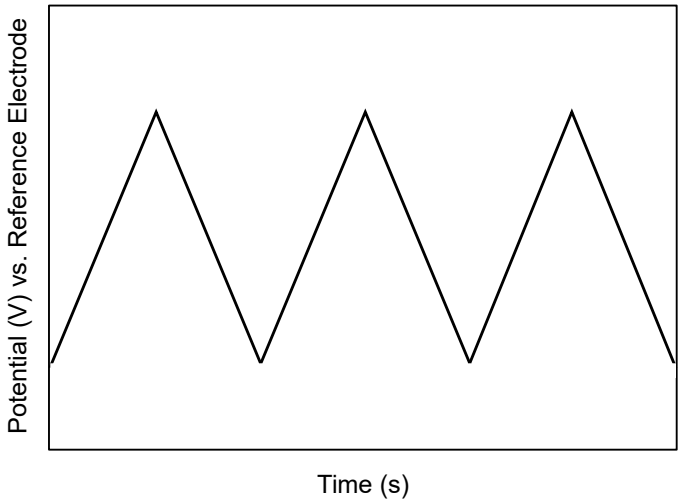

Figure 1.3. Cyclic voltammetry waveform shown with 3 cycles. The current is measured as the potential changes.

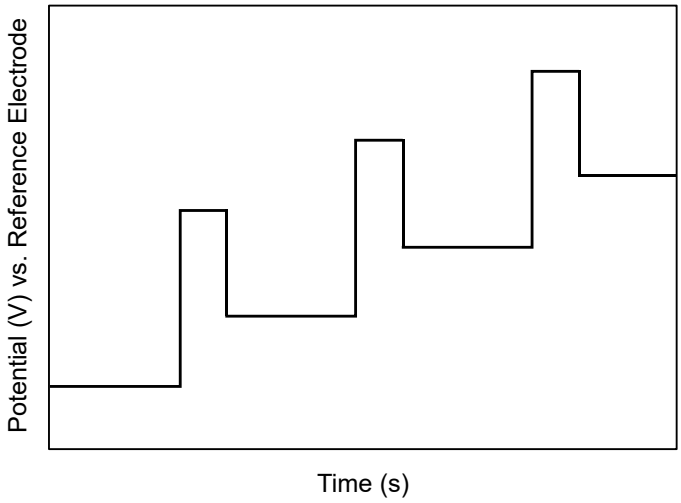

Figure 1.4. Differential pulse voltammetry waveform shown with 3 pulses. The current is measured before and after each pulse and the difference is calculated.

In contrast, differential pulse voltammetry (DPV), another electrochemical technique, while using a similar three-electrode setup, has a different excitation signal. In the DPV excitation signal in Figure 1.4, the current is first measured, then a potential is pulsed and the current measured again. Each pulse will see the potential increase by a certain predefined amount. The reported current then will be the difference between the measured current before and after each pulse at each potential. The main advantage with DPV compared to CV is that with each pulse and delay in measuring the current, non-Faradaic background charging currents have an opportunity to decay. Thus, Faradaic currents are primarily measured resulting in an increase in sensitivity.

1.5.4. Site-directed mutagenesis and subcloning

Developed in the early 1980s, site-directed mutagenesis is an invaluable technique used to purposefully generate deoxyribonucleic acid (DNA) clones with modified sequences.[50] It is typically used in concert with the polymerase chain reaction (PCR) to improve throughput. In contrast, random mutagenesis enables the researcher to produce a library with a large amount of sequence diversity. The modified sequences created from directed mutagenesis are useful as they help researchers understand the specific roles of amino acids and can be further used to generate new proteins with new characteristics. Traditional widely used methods such as the Stratagene QuickChange method utilize two primers complimentary to each other end-to-end which also contains the mutation of interest. However, there are strict requirements when designing the primers including length and melting temperature as dimerization can readily occur. Later techniques developed incorporate the usage of primer pairs but with only partial overlap with each other to achieve greater design flexibility.[51]

Following PCR amplification of the gene with the mutation(s), the original template DNA is removed by digestion with *DpnI*. *DpnI* is a restriction enzyme that cleaves DNA with methylated adenines while leaving unmethylated DNA intact. As PCR is an *in vitro* method of producing DNA, the DNA is not methylated. In contrast, the template DNA that has been produced in *Escherichia coli* dam^+ strains which includes 5-alpha and BL21 strains are methylated and thus removed. Following digestion and purification, the plasmids from the PCR reaction mixture are transformed into an *E. coli* strain for cloning. These cloning strains such as 5-alpha are *endA1* deficient to reduce nonspecific cleavage of double-stranded DNA and *recA1* deficient to reduce recombination events. The *E. coli*

are grown and selected for on growth media supplemented with an antibiotic for which the plasmid confers resistance. After amplification and purification of DNA from a clone, it is sequenced to ensure the mutation(s) are in their desired locations with the rest of the gene unaffected.

It is foreseeable that in cases where multiple plasmids are required but incompatible, antibiotic resistance genes need to be changed, or different promoters are required, the gene of interest can be subcloned into another vector with such features. To remove the gene from the donor plasmid, it can be cut using any available restriction sites that flank the insert. Preferably, the restriction sites should also be found in the receiving vector in the correct orientation. If the appropriate restriction sites are not available, new ones can be created on primers that are complimentary to the beginning and end of the gene sequence and amplified through PCR. The insert and recipient vector are then digested and ligated to each other.

1.5.5. Fluorotyrosine incorporation system

To incorporate fluorotyrosines (F_n-Tyr, n = 1-4) site-specifically within a protein, the amber suppression technique is used. The codon of the amino acid to be replaced is mutated using site-directed mutagenesis to the amber stop codon (TAG). The amber codon is used to minimize disruption of *E. coli* cellular processes during recombinant protein expression. Of the three stop codons which also include ochre (TAA) and opal (TGA), amber is used the least in the *E. coli* genome (~9%).[52] Under normal circumstances, the expression of this gene would yield a truncated protein due to the presence of the nonsense mutation. However, an additional plasmid pEVOL-*F_nYRS-E3* can be transformed to coexpress an evolved orthogonal transfer ribonucleic acid (tRNA) and an aminoacyl-tRNA synthetase (aaRS) from *Methanococcus jannaschii*.[53] The aaRS is selective for F_n-Tyr which then transfers the amino acid to the tRNA. The tRNA can recognize the amber stop codon and site-selectively incorporate a F_n-Tyr at that position. The orthogonal pair has also been evolved to recognize only F_n-Tyr and not natural tyrosine.

Literature reports provide characterization information for monomeric F_n-Tyr in aqueous environments[54] as well as redox and acid/base data in some protein models.[55] The different F_n-Tyr provide acidities with a pK_a range between 5-10 for the hydroxyl group

that can be used to systematically alter the strength of interactions between it and surrounding residues without potentially causing a large disruption in the local structure (Figure 1.5). Another advantage of using F_n-Tyr as a replacement over other naturally occurring amino acids is the ability to incorporate different variants by changing the expression media rather than performing site-directed mutagenesis for each proposed insertion. Further, the pEVOL amber suppression system is flexible and has been evolved in numerous studies to incorporate other unnatural amino acids.[56–58]

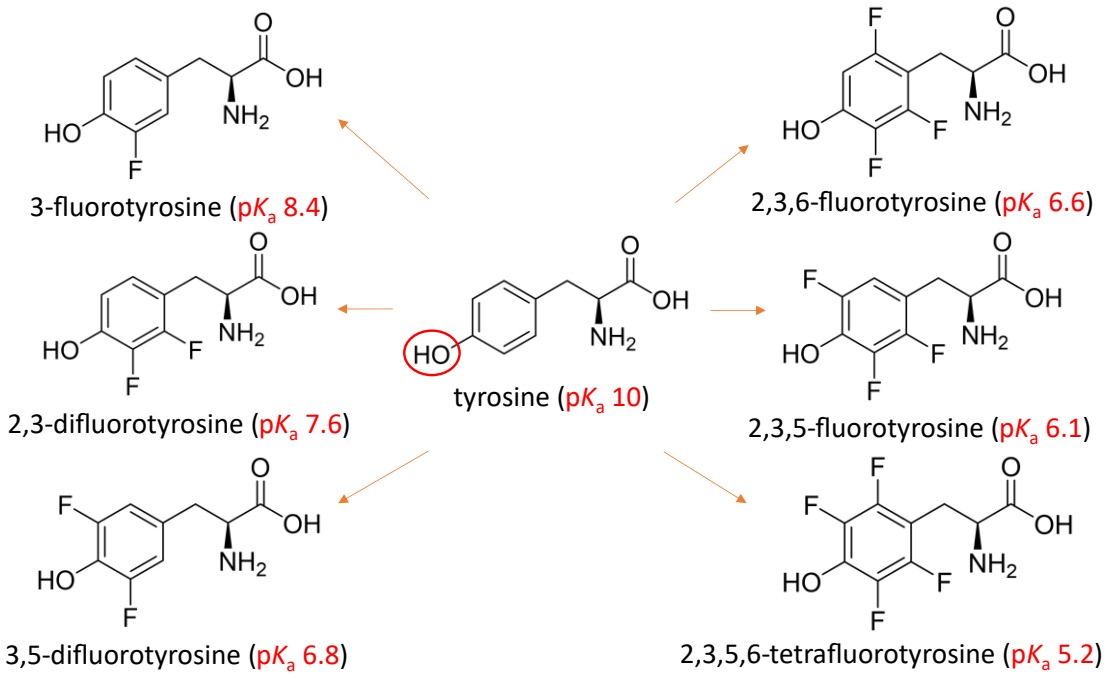

Figure 1.5. Fluorotyrosines to be site-specifically incorporated into proteins of interest using the amber suppression system. The pK_a are reported in Ref. [54] in aqueous media.

1.6. Thesis overview

The work described in this thesis is broadly concerned with (1) investigations of modified ET pathways in proteins and (2) the development of probes for developing a more detailed picture of amino acid microenvironments. Following this introductory chapter, Chapter 2 describes an attempt at the development of new protein models where the energy of a tyrosine residue in a known ET path is modified through incorporation of F_n-Tyr. While protein was obtained, the yields were insufficient for a detailed study. Next, the work in Chapter 3 involves an investigation of an ET pathway along two hydrogen-bonded bridges. Remarkably, this long-standing pathway appears to be only a minor

contributor to the observed ET kinetics and an alternative pathway via a through-space jump is preferred. Then Chapter 4 outlines the generation of mutants of azurin where a tyrosine is selectively modified to F_n-Tyr, which I propose as a new probe of the physical properties of buried protein sites. The final chapter, Chapter 5, provides some unifying conclusions and a forward-looking viewpoint that I hope is useful to future workers in this area.

1.7. Contributions

The work in this thesis was carried out entirely by the author. Jeffrey J. Warren assisted in the design of the research. Curtis A. Gibbs is acknowledged for assistance in operation of the time-resolved spectroscopy apparatus.

Chapter 2.

Electron tunnelling through Tyr67: changing bridge energetics with unnatural amino acids

2.1. Introduction

Cytochrome *c* and related *c*-type cytochromes have served as fruitful platforms for the development and benchmarking of theories of biomolecular electron transfer. The protein's small size, solubility, strong chromophore, stability toward mutagenesis, and well-known structure have made it a popular macromolecule for investigation of inter- and intra-protein redox processes (among a great many other areas). Its primary role in eukaryotes exists to shuttle electrons between cyt *c* reductase and cyt *c* oxidase in the mitochondrial inner membrane.[6] On the other hand, recombinant protein expression of cyt *c* within *E. coli* leads to localization in the cytoplasm. While the intraprotein electron transfer pathways in artificial cyt *c* protein models are well defined and can lead from various surface residues, cyt *c* when interacting with partner proteins through interprotein ET can also do so through direct heme-to-heme electron transfer.[59] Within the cyt *c* protein, the heme prosthetic group is useful in either serving as an electron donor or acceptor for ET studies. It is this heme that gives cyt *c* a characteristic red colour in the Fe(III) form and pink colour in the Fe(II) form. The work described in this Chapter is designed to advance ET models from cyt *c* by probing how the nature of the amino acids that comprise the bridge between donor and acceptor affect ET *without* modifying the pathway.

Several features of modern ET theory are based on studies of long-range ET in mutant forms of cyt *c*. In particular, the development of pathway models for ET has relied on studies involving cyt *c*. These ideas are outlined in more detail in Chapter 1. Importantly, that foundational work was concerned with elucidating how a network of covalent bonds, hydrogen bonds, and through-space jumps affect ET. Analysis of ET rates in five different pathways (Figure 2.1) shows that proteins with 10 Å differences in donor-acceptor distance can have identical observed rates (e.g., ET from heme and acceptor at His72 versus His 39). Accounting for the through-bond distances explains why the rates are similar.

Those studies established the idea that the distinct pathway that an electron travels is a crucial determinant in the rate of ET. However, less is known about how the relative orbital energies of the bridge units affect ET in proteins. Studies of small molecules show that the energy of the bridge with respect to that of the donor and/or acceptor can give rise to different magnitudes of electronic coupling.[60] This idea has never been rigorously tested in proteins because amino acid substitutions can often change the fundamental nature of the pathway, rather than simply the bridge energetics. In the extreme, the electron (or hole) localizes on a bridge unit in a formal redox process known as "hopping."[16,61]

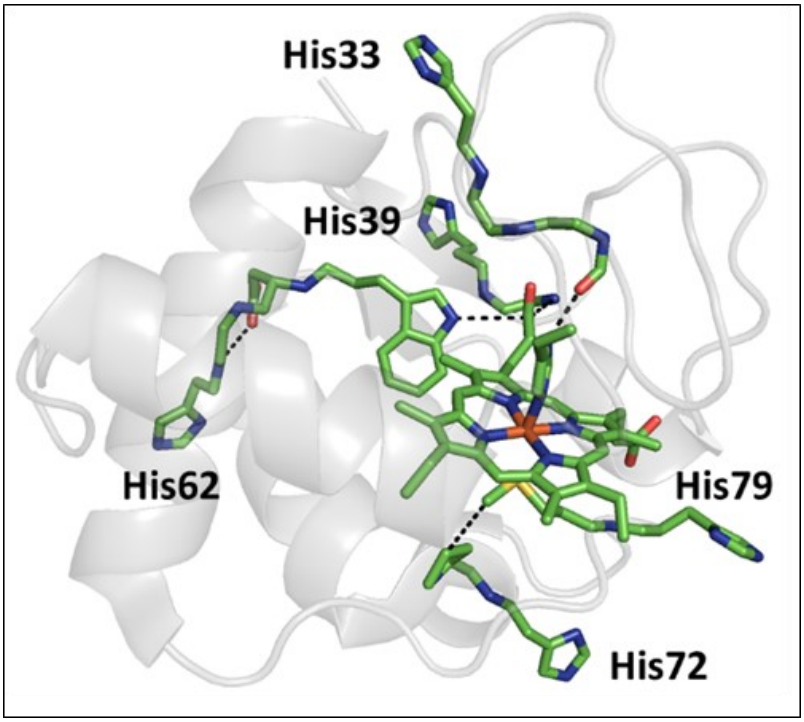

Figure 2.1. The five electron transfer pathways studied in yeast iso-1 cytochrome *c* (PDB ID 1YCC). Dashed lines represent hydrogen bonds or through-space jumps in the pathways.

2.1.1. The Tyr67 electron transfer pathway

Electron transfer in a new "pathway mutant" in cyt *c* was described in 2014.[62] The pathway is set out in Figure 2.2 and involves ET from a Ru-photosensitizer attached to a Cys (in the Glu66Cys mutant) along Tyr67, to the Fe-ligating Met80. That report specifically explored how off-pathway substitutions near Tyr67 affected protein dynamics on the timescale of ET. These substitutions provided new views on how protein dynamics modulate ET, even when the basic parts of the pathway from D to A are unchanged. In

addition, it has been suggested that Tyr67 is essential in maintaining the protein's hydrogen bond network during normal biological redox cycling. Tyr67 also plays a key structural role by triggering controlled cell death known as apoptosis.[63,64] During this process, elimination of Tyr67 leads to the loss of Fe-S coordination between the heme and Met80. The loss causes the formation of a channel to which H_2O_2 can bind and activate the intrinsic peroxidase activity of cyt *c* to trigger the cell death cascade.[65] Other substitutions to Tyr67 result in weakening of the Fe-S bond causing intermediate-level peroxidase activity.[63]

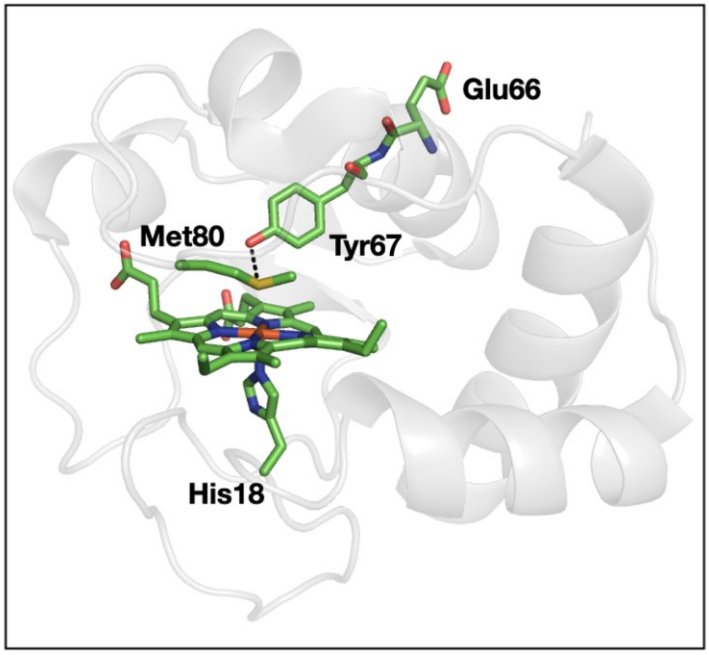

Figure 2.2. Yeast iso-1-cytochrome *c* pathway leading from amino acid 66 to the iron heme. The dashed lines represent the interaction between the hydroxyl group of Tyr67 and Met80 sulfur in the pathway of interest (PDB 1YCC).

In the context of this thesis, the Warren Group has been interested in a class of non-covalent interactions that involve methionine and the aromatic amino acids tyrosine, tryptophan, and phenylalanine.[66,67] In those examples, the Met-sulfur interacts with the face and/or sides of an aromatic group. However, there are other examples of Met-aromatic interactions that are also widely distributed.[68] These interactions have not been well studied, and even less is known about the role(s) they play in protein folding, protein stability, and the redox reactions of metal sites.

Within yeast cyt *c* there exists a Met-Tyr-Met bridging interaction that is widely distributed among related proteins. The pathway is comprised of the highly conserved Tyr67 discussed previously which bridges two methionines at positions 64 and 80 (Figure 2.3). The first interaction is where the sulfur in Met64 interacts side-on with the tyrosyl group of Tyr67. A second interaction is present where the hydroxyl group of Tyr67 interacts strongly with the sulfur of Met80 (O•••S distance of 3.2 Å). Crystal structures show that this sulfur from Met80 is structurally important as it is axially coordinated to the iron. The interaction between Tyr67 and Met80 is, in some way, related to a hydrogen bond, although the dipolar interaction is weaker.

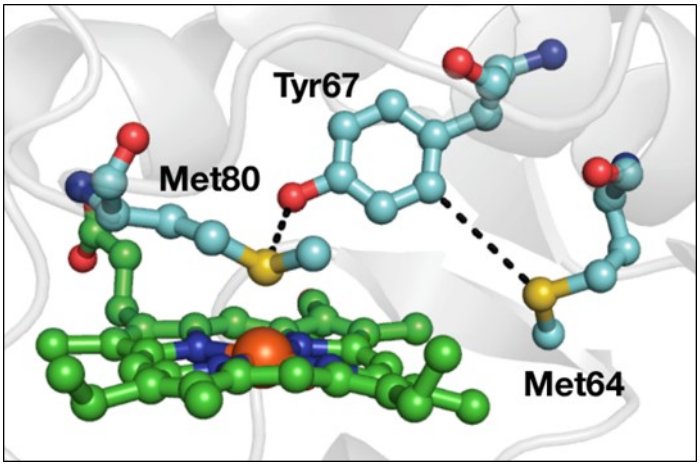

Figure 2.3. Yeast iso-1-cytochrome *c* bridging interaction between Tyr67 hydroxyl and Met80 sulfur lone pair. A second side-on interaction is present between Met64 sulfur lone pair and the tyrosyl group of Tyr67.

2.1.2. Project outline

To explore the importance of the Tyr67:Met80 interaction and ET pathway, we attempted to incorporate a series of fluorinated tyrosines (n = 1-4) site-specifically. As the different F$_n$-Tyr have a pK_a range between 5-10 for the hydroxyl group, the interaction with Met80 can be systematically modified. As Tyr67 is not known to participate in redox reactions, the modification of it would only affect its interaction towards the methionines in theory. An amber stop codon (TAG) was substituted with the codon encoding Tyr67 in the iso-1-cytochrome *c* gene (*CYC1*) using PCR site-directed mutagenesis. An additional substitution on the surface of the protein, Glu66Cys was also made to allow for a ruthenium label to be covalently attached as an electron acceptor. Fluorotyrosines were synthesized from the corresponding fluorophenol, ammonium, and pyruvate using an

enzymatic synthesis by tyrosine phenol-lyase (TPL) and purified following the literature.[54,69,70] Once in possession of the F_n-Tyr67 mutants, the protein, labelled with a Ru(II) photosensitizer at the Cys66 position was to be used to study kinetics with flash-quench experiments. As the pK_a is decreased from one fluorotyrosine to another, the length of the interaction is expected to decrease and thus increase k_{ET}.

2.2. Experimental

2.2.1. Materials

All reagents used were purchased from Sigma-Aldrich without purification unless otherwise noted. Miller Luria-Bertani broth (LB) and L-arabinose were purchased from BioShop. 2-fluorophenol, 2,3-difluorophenol, 2,6-difluorophenol, 2,3,6-trifluorophenol, and 2,3,5,6-tetrafluorophenol were purchased from Tokyo Chemical Industry. Water used was from a Barnstead EASYpure system (18 MΩ cm^{-1}).

2.2.2. Site-directed mutagenesis

S. cerevisiae iso-1-cytochrome *c* mutants encoded by *CYC1* were prepared from pseudo-wild-type (WT*) protein cloned in pET20b (Novagen) between NdeI and BamHI restriction sites. The WT* parent pseudo-wild-type construct contained two substitutions, Lys72Ala and Cys102Ser. The mutants Glu66Cys and Glu66Cys/Tyr67TAG were introduced using site-directed mutagenesis with the Q5 High-Fidelity PCR Kit (New England Biolabs). See Appendix A for forward and reverse primers used (Integrated DNA Technologies). Following the PCR reactions, PCR cleanup was performed with the Qiagen QIAquick PCR Purification Kit and template DNA digested with DpnI restriction enzyme (Thermo Scientific FastDigest). A second PCR cleanup followed the DpnI digestion. The PCR reaction mixtures were transformed into chemically competent 5-alpha *E. coli* cells (New England Biolabs) and selected for on ampicillin-supplemented LB agar plates incubated for 16 hours at 37°C. Isolated colonies were inoculated in liquid LB with 100 µg/mL ampicillin and grown for 16 hours at 37°C with shaking. Plasmid DNA was extracted and purified using the Qiagen QIAprep Spin Miniprep Kit. The *CYC1* plasmid sequences were verified using Eurofins Genomics SimpleSeq Sanger sequencing service.

2.2.3. Subcloning

The pET20b-*CYC1* inserts containing WT*, Glu66Cys, and Glu66Cys/Tyr67TAG were subcloned into pET24a vector (Novagen). Each insert and pET24a was double digested with NdeI and EcoRI (Thermo Scientific FastDigest) and isolated by agarose gel electrophoresis. Gel extraction was then performed with the Qiagen QIAquick Gel Extraction Kit. The insert was ligated to pET24a with T4 DNA ligase (New England Biolabs) and transformed into chemically competent 5-alpha *E. coli* cells. The cells were grown and selected on kanamycin-supplemented LB agar plates for 16 hours at 37°C. Single colonies were inoculated in LB with 50 µg/mL kanamycin and grown for 16 hours at 37°C with shaking. The plasmid DNA was extracted and sequenced using Eurofins Genomics SimpleSeq Sanger sequencing service.

CYC1 WT*, Glu66Cys, and Glu66Cys/Tyr67TAG variants along with *ccmABCDEFGH* genes were also subcloned into pETDuet-1 vector (Novagen). All *ccm* genes were cloned into multiple cloning site (MCS) 1 containing T7 promoter-1 while *CYC1* was cloned into MCS2 containing T7 promoter-2. To enable cloning of each gene into the specific cloning site on pETDuet-1, PCR was performed on pEC86 upstream and downstream of *ccmABCDEFGH* to insert NcoI and HindIII restriction sites (see Appendix A for the primers). PCR was also performed on pET20b to insert NdeI and XhoI upstream and downstream of *CYC1* for the variants WT*, Glu66Cys, and Glu66Cys/Tyr67TAG. Parental DNA was removed with DpnI restriction enzyme. Both pETDuet-1 and the *CYC1* PCR product were double digested with NdeI and XhoI restriction enzymes (Thermo Scientific FastDigest) followed by a PCR cleanup and ligated with T4 DNA ligase. The ligated plasmid was amplified by transforming into chemically competent 5-alpha cells and grown. The plasmid was isolated using previously described techniques. DNA agarose gel electrophoresis was used with a 1.2% agarose gel to determine if the pETDuet-1 contained the *CYC1* gene and was sequenced to verify (Eurofins Genomics).

To insert *ccmABCDEFGH*, a double digest was performed on pETDuet-1-*CYC1* and the *ccmABCDEFGH* PCR product with NcoI and HindIII restriction enzymes (Thermo Scientific FastDigest). The PCR was followed by a PCR cleanup and ligation with T4 DNA ligase to create pETDuet-*ccm-CYC1* containing 9 genes. The plasmid was transformed into chemically competent 5-alpha cells and amplified plasmid was purified using previously described techniques. DNA agarose gel electrophoresis was performed with a

1.2% agarose gel to determine if the pETDuet-1 plasmid contained both the specific *CYC1* mutant at MCS2 and *ccmABCDEFGH* genes at MCS1. Sequencing was used to verify the presence and sequences of both genes (Eurofins Genomics).

2.2.4. Synthesis of fluorotyrosines

E. coli strain SVS 370 containing pTZTPL plasmid was provided as a gift from JoAnne Stubbe from Massachusetts Institute of Technology. *The* expression of TPL was based on literature-reported methods.[69,71,72] A single colony of SVS 370 *E. coli* containing pTZTPL plasmid encoding *tpl* H343A was used to inoculate 30 mL of LB with 100 µg/mL ampicillin and incubated at 37°C with shaking (180 rpm) for 6 hours. Large scale expressions of 8 L of broth composed of 1% (w/v) casein enzymic hydrolysate, 0.5% (w/v) yeast extract, 0.5% (w/v) sodium chloride, and 100 µg/mL ampicillin were inoculated with 16 mL of the starter culture. The cultures were incubated at 37°C for 20 hours with shaking (150 rpm). The cells were harvested by centrifugation (4500 *g*, 10 min, 4°C) and stored at –80°C. The cell pellet (34 g) was resuspended in 115 mL of 0.1 M potassium phosphate buffer (pH 7) containing 1 mM ethylenediaminetetraacetic acid (EDTA), 0.1 mM pyridoxal phosphate, and 5 mM β-mercaptoethanol. The resuspension was sonicated on ice for 3 minutes (Branson Digital Sonifier 250 Cell Disruptor) and clarified lysate collected following centrifugation (25,000 *g*, 30 min, 4°C).

The synthesis of the F_n-Tyr (n = 1–4) including 3-fluorotyrosine (3-F-Tyr), 2,3-difluorotyrosine (2,3-F_2-Tyr), 3,5-difluorotyrosine (3,5-F_2-Tyr), 2,3,5-trifluorotyrosine (2,3,5-F_3-Tyr), and 2,3,5,6-tetrafluorotyrosine (2,3,5,6-F_4-Tyr) were performed based on literature methods.[54,70] For each fluorotyrosine, ≤10 mM of the respective fluorophenol was added to a 2 L solution of 30 mM ammonium acetate, 60 mM sodium pyruvate, and 5 mM β-mercaptoethanol adjusted to pH 8 with ammonium hydroxide. For all fluorotyrosines except 2,3,5,6-tetrafluorotyrosine, 40 µM pyridoxal phosphate and approximately 60 units (U) of TPL were added where one unit is defined as 1 µmol of product per minute. The solution was stirred for 3-4 days at 22°C in the dark. For the synthesis of 2,3,5,6-F_4-Tyr, 40 µM pyridoxal phosphate and 600 units of TPL were added. The solution was stirred for 3-4 weeks at 22°C in the dark. Each week, an additional 40 U of TPL and 1 mM 2,3,5,6-tetrafluorophenol were added.

Following the enzyme-catalyzed reaction, the solution was acidified to pH 2.7 with HCl to precipitate TPL. The precipitate was removed by filtering through a Celite pad. To remove unreacted fluorophenol, a liquid-liquid extraction was performed on the filtrate with 500 mL ethyl acetate and the aqueous layer collected. The solution was further purified with a Dowex 50W-X8 hydrogen form cation exchange column (20-50 mesh) prepared with 2 column volumes of 1 M HCl and equilibrated with water. The solution was loaded on the column, washed with 8 column volumes of water and eluted with 10% (v/v) ammonium hydroxide. Fractions were tested with ninhydrin to determine the presence of free amines. The ninhydrin solution was made from 0.19% (w/v) ninhydrin, 0.5% (v/v) acetic acid, 4.5% (v/v) water, and 95% (v/v) *n*-butanol. A positive ninhydrin test as determined with a pink or purple spot on a thin-layer chromatography plate indicated the presence of a free amine. Positive fractions were combined, the solvent was removed *in vacuo*, and the F_n-Tyr analogue collected. The F_n-Tyr analogues were characterized using ^{1}H and ^{19}F nuclear magnetic resonance (NMR) recorded with a Bruker Ultrashield Plus 500 MHz.

3-F-Tyr. Pale yellow solid. Yield: 94%. ^{1}H NMR (500 MHz, D_2O): δ (ppm) 3.05 (dd, 1H, 7.9, 14.8 Hz), 3.20 (dd, 1H, 5.0, 14.7 Hz), 3.94 (t, 1H, 6.4 Hz), 6.98 (m, 2H), 7.08 (d, 1H, 11.9 Hz); ^{19}F NMR (500 MHz, D_2O): δ (ppm) -136.79 (s, 1F).

2,3-F_2-Tyr. Pale yellow solid. Yield: 72%. ^{1}H NMR (500 MHz, D_2O): δ (ppm) 3.10 (dd, 1H, 7.7, 14.8 Hz), 3.29 (dd, 1H, 5.3, 14.8 Hz), 3.96 (dd, 1H, 5.9, 7.2 Hz), 6.81 (t, 1H, 8.2 Hz), 6.95 (t, 1H, 8.1 Hz); ^{19}F NMR (500 MHz, D_2O): δ (ppm) -161.31 (d, 1F, 20.0 Hz), -141.37 (d, 1F, 20.0 Hz).

3,5-F_2-Tyr. Pale yellow solid. Yield: 76%. ^{1}H NMR (500 MHz, D_2O): δ (ppm) 3.05 (dd, 1H, 7.8, 14.7 Hz), 3.19 (dd, 1H, 5.2, 14.7 Hz), 3.95 (dd, 1H, 5.4, 7.7 Hz), 6.93 (m, 2H); ^{19}F NMR (500 MHz, D_2O): δ (ppm) -133.22 (s, 2F).

2,3,5-F_3-Tyr. Pale yellow solid. Yield: 83%. ^{1}H NMR (500 MHz, D_2O): δ (ppm) 2.94 (dd, 1H, 7.7, 14.0 Hz), 3.19 (d, 1H, 13.3 Hz), 3.87 (t, 1H, 6.5 Hz), 6.68 (t, 1H, 9.3 Hz); ^{19}F NMR (500 MHz, D_2O): δ (ppm) -159.45 (t, 1F, 17.7 Hz), -147.58 (m, 1F), -139.97 (m, 1F).

2,3,5,6-F_4-Tyr. Pale yellow solid. Yield: 24%. ^{1}H NMR (500 MHz, D_2O): δ (ppm) 3.15 (dd, 1H, 7.8, 14.4 Hz), 3.28 (dd, 1H, 4.4, 14.3 Hz), 3.91 (m, 1H); ^{19}F NMR (500 MHz, D_2O): δ (ppm) -165.13 (d, 2F, 17.2 Hz), -148.13 (d, 2F, 17.2 Hz).

2.2.5. Protein expression and purification

The pEVOL-*F_nYRS-E3* plasmid was provided as a gift from JoAnne Stubbe from Massachusetts Institute of Technology.[53] To obtain BL21(DE3) *E. coli* (New England Biolabs) with the appropriate plasmids a series of sequential transformations were performed. Chemically competent BL21(DE3) was transformed with pEC86[73] and pET20b-*CYC1*$_{Glu66Cys}$ or pET20b-*CYC1*$_{Glu66Cys/Tyr67TAG}$. In the case of pET20b-*CYC1*$_{Glu66Cys/Tyr67TAG}$, pEVOL-*F_nYRS-E3* was also transformed as a third plasmid and selected for on LB agar supplemented with 100 µg/mL ampicillin and 25 µg/mL chloramphenicol. A single colony was used to inoculate 35 mL of LB broth with ampicillin and chloramphenicol. The culture was incubated at 37°C, 180 rpm for 16 hours. From the starter culture, 240 µL was used to inoculate 40 mL of LB broth with two times yeast extract (LB2YE) containing 1 mM of an F$_n$-Tyr and 0.05% (w/v) L-arabinose was added concurrently and incubated at 37°C (180 rpm). After 5 hours, the temperature was reduced to 30°C and incubated for 15 additional hours. Alternatively, 0.05% L-arabinose was added 5 hours after seeding with the starter culture, the temperature reduced to 30°C and incubated for an additional 15 hours. From 1 mL of each culture, plasmid minipreps were performed to purify the plasmids and were visualized on a 1.2% agarose gel stained with ethidium bromide. The remainder of the culture was harvested by centrifugation (4500 *g*, 10 min, 4°C).

Expression cultures with pET24a-*CYC1*$_{Glu66Cys/Tyr67TAG}$ were performed similarly as described for pET20b-*CYC1*$_{Glu66Cys/Tyr67TAG}$ with selection by 100 µg/mL ampicillin and 50 µg/mL kanamycin. Induction of the pET24a plasmid was performed with 1 mM isopropyl β-D-1-thiogalactopyranoside (IPTG) added at the same time as 0.05% L-arabinose. Expression cultures with pETDuet-1-*ccmABCDEFGH/CYC1*$_{Glu66Cys/Tyr67TAG}$ were performed similarly after sequentially transforming BL21(DE3) with pEVOL-*F_nYRS-E3* and selecting with 100 µg/mL ampicillin and 25 µg/mL chloramphenicol. To optimize expression levels of cyt *c*, a sodium dodecyl sulfate-polyacrylamide gel electrophoresis (SDS-PAGE) was performed using whole-cell lysate and expression levels of cyt *c* were compared by densitometry using ImageJ software.[74] The theoretical molecular weight of the proteins was calculated based on the DNA sequence using the ExPASy Compute pI/Mw tool.[75–77] Optimized expressions on a preparative scale were as follows. A 35 mL LB culture supplemented with 100 µg/mL ampicillin and 25 µg/mL chloramphenicol was inoculated with a colony and incubated (37°C, 180 rpm, 16 hours). From the initial culture,

6 mL was used to inoculate 1 L of LB2YE supplemented with the antibiotics and 1 mM F_n-Tyr (solubilized with NH_4OH). The culture was incubated at 37°C and 120 rpm. At an OD_{600} of 0.1–0.2, 0.05% (w/v) L-arabinose was added. At an OD_{600} of 0.9, 1 mM IPTG was added and grown for an additional 15 hours.

For purification of cyt *c* Glu66Cys, the *E. coli* pellet was resuspended in 100 mL lysis buffer constituted of 50 mM Tris(hydroxymethyl)aminomethane (Tris), 1 mM EDTA, 1 mM phenylmethylsulfonyl fluoride (PMSF), 10 mM β-mercaptoethanol, 1 mM sodium ascorbate, 1 µg/ml DNase I, and 1 mg/mL lysozyme at pH 8. The resuspension was sonicated for 6 minutes on ice and centrifuged (24,000 *g*, 60 min, 4°C). The clarified lysate was collected and purified with a carboxymethyl (CM) cellulose cation exchange column (Cytiva) equilibrated with 10 mM Tris (pH 8) and 0.1 mM EDTA. The column was washed with 3 column volumes of the lysis buffer without DNase I and lysozyme and a gradient elution was used with 20 mM Tris (pH 8), 0.1 mM EDTA, and 0 to 250 mM NaCl to elute cyt *c*. Fractions containing cyt *c* were combined, concentrated by ultrafiltration (Amicon, 10 kDa) and exchanged into 5 mM sodium phosphate buffer (pH 7) by gel filtration with a PD-10 column (Cytiva).

2.3. Results and discussion

2.3.1. Expression tests

Expression and purification of cyt *c* Glu66Cys with a natural tyrosine at position 67 produced protein in similar amounts as cyt *c* WT*. The WT* protein and all other mutants contained additional substitutions, Lys72Ala and Cys102Ser. Native yeast cytochrome *c* contains a trimethylated lysine at position 72 so the substitution to alanine prevents iron heme misligation. The Cys102Ser substitution removes the only cysteine available on the surface to prevent Cys-Cys dimerization and mislabeling with our Cys-reactive Ru complex (described in Chapter 3).

Expression of any of the F_n-Tyr67 cyt *c* requires transformation of three plasmids into *E. coli* for expression: a plasmid with the cyt *c* gene, the pEC86 plasmid containing cytochrome *c* maturation proteins (*ccmABCDEFGH*) from *E. coli*, and the pEVOL-*F_nYRS-E3* plasmid for the amber tRNA F_n-Tyr incorporation system (Table 2.1). The pEC86 plasmid is essential for expressing the holo-form of cytochrome *c* with covalently attached

heme.[73] The genes are present in the *E. coli* chromosome though are only expressed under anaerobic conditions. Initial expressions with pET20b-*CYC1*$_{Glu66Cys/Tyr67TAG}$ supplemented with 1 mM of any F_n-Tyr gave poor expression yields. The BL21(DE3) cells were transformed sequentially with 3 recombinant plasmids in the order of pEC86, pET20b-*CYC1*$_{Glu66Cys/Tyr67TAG}$, and pEVOL-*F_nYRS-E3*. As both pEVOL-*F_nYRS-E3* and pEC86 encode for the same *CMR* chloramphenicol resistance gene for antibiotic selection, an agarose gel was used to determine if pEVOL-*F_nYRS-E3* had been successfully transformed and retained (Figure 2.4). From each test expression, plasmids were extracted and purified from 1 mL of culture. Calculations of plasmid sizes showed that pET20b-*CYC1*$_{Glu66Cys/Tyr67TAG}$ was expected to be approximately 4000 base pairs (bp) in size, pEVOL-*F_nYRS-E3* with 6000 bp, and pEC86 with 12,000 bp. Discrepancies between calculated and observed sizes were likely due to the supercoiled nature of the plasmid DNA as they were not linearized. The DNA agarose gel showed the presence of a plasmid of similar size to pET20b-*CYC1*$_{Glu66Cys/Tyr67TAG}$. However, pEVOL-*F_nYRS-E3* did not appear to be present in sufficient quantities to be visualized on the agarose gel.

Table 2.1. Summary of expression plasmids used in Chapter 2

Plasmid Name	Bacterial Resistance	Origin of Replication	Purpose
pEC86	Chloramphenicol	*p15A*	Expression of 8 cyt *c* maturation proteins
pEVOL-*F_nYRS-E3*	Chloramphenicol	*p15A*	F_n-Tyr specific tRNA and aaRS
pET20b-*CYC1*	Ampicillin	*pBR322*	Expression of WT* cyt *c*
pET20b-*CYC1*$_{Glu66Cys}$	Ampicillin	*pBR322*	Expression of cyt *c* Glu66Cys
pET20b-*CYC1*$_{Glu66Cys/Tyr67TAG}$	Ampicillin	*pBR322*	Expression of cyt *c* Glu66Cys/Tyr67TAG
pET24a-*CYC1*$_{Glu66Cys}$	Kanamycin	*pBR322*	Expression of cyt *c* Glu66Cys
pET24a-*CYC1*$_{Glu66Cys/Tyr67TAG}$	Kanamycin	*pBR322*	Expression of cyt *c* Glu66Cys/Tyr67TAG
pETDuet-1-*ccmABCDEFGH/CYC1*	Ampicillin	*pBR322*	Expression of WT* cyt *c* and 8 cyt *c* maturation proteins
pETDuet-1-*ccmABCDEFGH/CYC1*$_{Glu66Cys}$	Ampicillin	*pBR322*	Expression of cyt *c* Glu66Cys and 8 cyt *c* maturation proteins
pETDuet-1-*ccmABCDEFGH/CYC1*$_{Glu66Cys/Tyr67TAG}$	Ampicillin	*pBR322*	Expression of cyt *c* Glu66Cys/Tyr67TAG and 8 cyt *c* maturation proteins

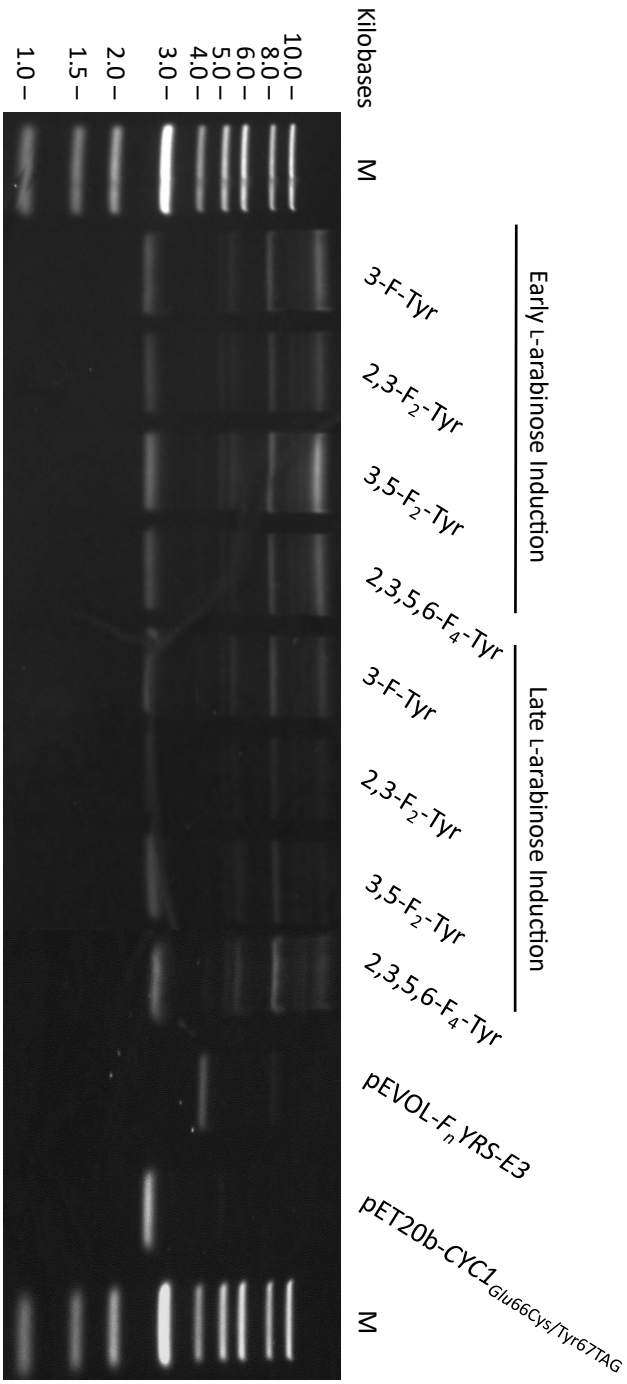

Figure 2.4. **DNA agarose gel of test expressions for F_n-Tyr incorporated cytochrome *c* Glu66Cys/Tyr67TAG to determine transformation and retention of pEVOL-*F_nYRS-E3*. Cells were also transformed with pEC86 and pET20b-*CYC1*$_{Glu66Cys/Tyr67TAG}$. Controls consisting of only pEVOL-*F_nYRS-E3* and pET20b-*CYC1*$_{Glu66Cys/Tyr67TAG}$ were also included. Early induction was performed when inoculating large expression flasks with the starter culture while late induction was performed 5 hours after inoculation and decreasing the incubation temperature to 30°C.**

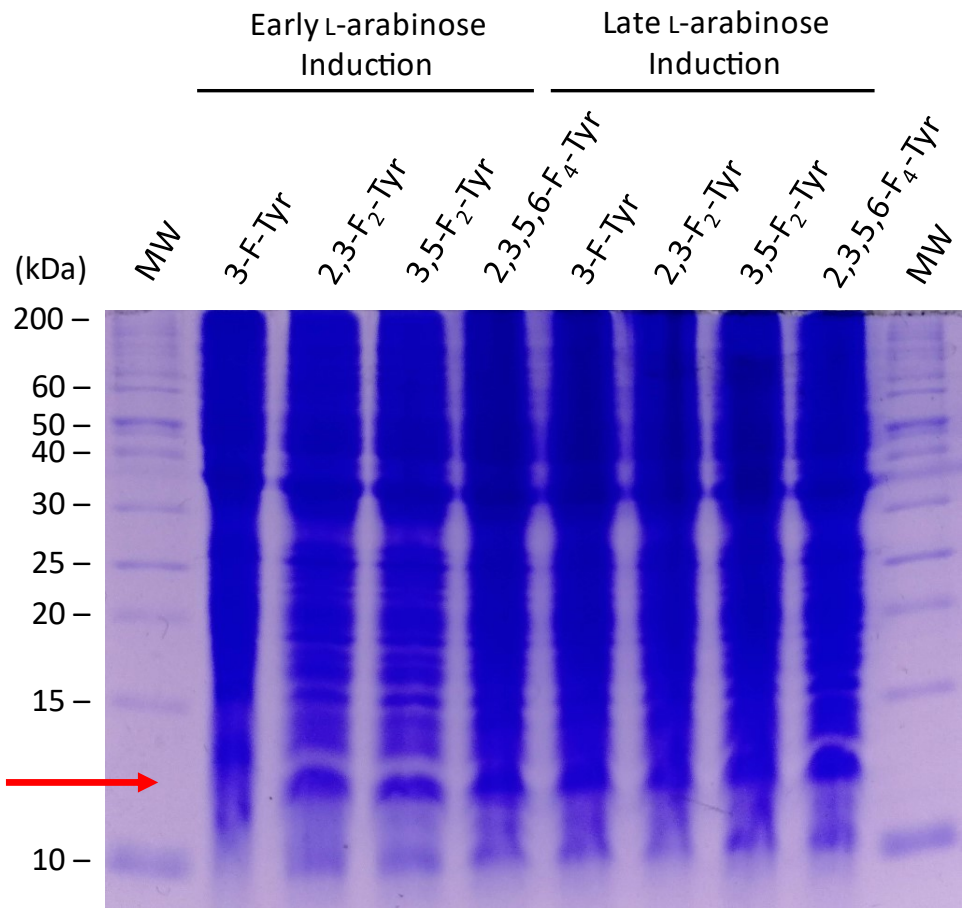

Figure 2.5. Whole-cell lysate SDS-PAGE gel of test expressions for F_n-Tyr incorporated cytochrome *c* Glu66Cys/Tyr67TAG. Early L-arabinose induction was performed when inoculating larger expression cultures containing 1 mM of an F_n-Tyr with the starter culture. Late L-arabinose induction was performed 5 hours after inoculation of the large cultures. The red arrow indicates the band representing cyt *c* (~12.7 kDa).

Using the same test expressions, an SDS-PAGE was also performed to determine overexpression of cyt *c* protein (Figure 2.5). Based on the SDS-PAGE gel, there was no clear overexpression of cyt *c* with different F_n-Tyr analogues at the expected mass of 12.7 kDa (Table 2.2). Test expressions inducing the pEVOL-*F_nYRS-E3* plasmid with L-arabinose at different time points either during inoculation of large cultures or 5 hours after inoculation of large cultures were performed. The differing time points were used to identify the optimal time for the cell to produce F_n-Tyr specific tRNA and aaRS to allow for efficient amber suppression. Densitometry measurements of the SDS-PAGE gel revealed that inducing the BL21(DE3) cells 5 hours after induction increased expression levels of a protein at 12.7 kDa, a mass similar in size to cyt *c*. However, in all cases, there did not

appear to be overexpression of cyt *c.* Assuming there are no issues with the ligation of the heme prosthetic group, a qualitative visual test is possible for intact protein without purification because the *E. coli* pellet is pink in colour, rather than yellow/brown, due to the red colour of the cyt *c* protein. Additionally, SDS-PAGE gels with whole-cell lysates show a more intense band of interest relative to background proteins.

Table 2.2. Calculated and MALDI-TOF collected masses of cytochrome *c* variants[a]

Variant	Expected Average Mass (Da)	Expected Monoisotopic Mass (Da)	Obtained Monoisotopic Mass (Da)
WT*	12657.61	12655.29	12641.17
Glu66Cys	12631.58	12629.26	—
Glu66Cys Truncated[b]	7811.18	7813.83	—
Glu66Cys/Tyr67-(3-F-Tyr)	12649.57	12647.25	—
Glu66Cys/Tyr67-(2,3-F_2-Tyr)	12667.56	12665.25	—
Glu66Cys/Tyr67-(3,5-F_2-Tyr)	12667.56	12665.25	—
Glu66Cys/Tyr67-(2,3,5-F_3-Tyr)	12685.55	12683.24	—
Glu66Cys/Tyr67-(2,3,5,6-F_4-Tyr)	12703.54	12701.23	—

[a]Calculated masses include the mass of heme.
[b]Truncated protein masses calculated based on the cytochrome *c* Glu66Cys sequence up to and including Cys66.

2.3.2. Controlled expression of cytochrome *c*

In an attempt to increase expression levels of cyt *c* Glu66Cys/Tyr67TAG, subcloning was performed with different vectors. The pET20b vector with *CYC1* insert used in initial test expressions contains a T7 promoter upstream of the insert which requires a T7 RNA polymerase for transcription. The BL21(DE3) strain is a λDE3 lysogen that encodes for the necessary T7 RNA polymerase controlled by an IPTG-inducible *lacUV5* promoter. However, even in the absence of IPTG, the cell is able to express some T7 RNA polymerase which ultimately leads to basal level expression of proteins through the pET20b T7 promoter.[78]

As was seen for cases such as cyt *c*, expression without IPTG still enabled overexpression of WT* and Glu66Cys with good levels of protein production. For cases of cyt *c* Glu66Cys/Tyr67TAG expressions, the result is that, without induction of the L-arabinose promoter in pEVOL-*F_nYRS-E3*, the F_n-Tyr specific tRNA and aaRS are not produced and the cells may express prematurely truncated cyt *c* up to the amber stop codon. The phenomenon has been observed in similar amber suppression systems.[56–58] To allow for tighter control over the expression of cyt *c* specifically to eliminate the

possibility of truncated protein, the pET24a vector was used as it contains a *lac* operator downstream of the T7 promoter.[79,80] The *lac* operator requires the presence of IPTG to enable transcription of the target gene. Test expressions with pET24a-*CYC1*$_{Glu66Cys/Tyr67TAG}$ were unsuccessful for overexpression of cyt *c* as the pellets were similar in colour to expressions with pET20b-*CYC1*$_{Glu66Cys/Tyr67TAG}$. Attempts to purify protein were also unsuccessful due to low levels of expression.

2.3.3. Decreasing plasmid incompatibilities

As both the pEC86 cyt *c* maturation proteins plasmid and pEVOL-*F$_n$YRS-E3* plasmid encode for the same chloramphenicol resistance gene, we sought to reduce the number of recombinant plasmids needed to be transformed and maintained by the cells. Further, while pET20b and pET24a vectors use a *pBR322* origin of replication[78,80], both pEC86 and pEVOL-*F$_n$YRS-E3* use a *p15A* origin of replication.[53,73,81] Two plasmids with the same origin are generally incompatible in a cell, so the pETDuet-1 vector was used to eliminate plasmid origin incompatibility, eliminate selection with the same chloramphenicol resistance gene, and reduce the number of recombinant plasmids needed simultaneously. The pETDuet-1 vector harbours a *pBR322* origin of replication, *bla* ampicillin resistance gene, and contains two MCS regions, each with its own T7 promoter and *lac* operator. By cloning the *ccmABCDEFGH* genes from pEC86 into T7 promoter-1 and *CYC1* gene into T7 promoter-2, we were able to reduce the number of recombinant plasmids needed for the expression of cyt *c* Glu66Cys/Tyr67TAG down to two, the pETDuet-*ccm-CYC1* and pEVOL-*F$_n$YRS-E3* plasmids. The system also eliminated origin of replication incompatibilities and allowed for independent antibiotic selection for each plasmid.

To verify the effectiveness of the newly created plasmid, WT* was expressed and purified. Matrix-assisted laser desorption/ionization-time of flight (MALDI-TOF) mass spectrometry analysis showed the obtained mass to be in agreement with the expected mass (Table 2.2 and Figure A.11). Preparative scale expressions of the proteins (1 L) with different F$_n$-Tyr appeared to marginally overexpress cyt *c* with 3-F-Tyr, 2,3-F$_2$-Tyr, 3,5-F$_2$-Tyr, and 2,3,5-F$_3$-Tyr as seen from the presence of 12.7 kDa bands on an SDS-PAGE (Figure 2.6). Purified Glu66Cys protein was included in the gel as a positive control which appeared to have a similar mass to the other lanes. Truncated protein, with a calculated mass of 7811 Da, was not visible on the gel indicating that F$_n$-Tyr incorporation was likely not an issue. Addition of cell lysate onto a CM Sepharose cation exchange column did not

appear to isolate any cyt *c* likely due to poor expression levels. It is possible that changing the Tyr67 to F_n-Tyr causes a significant perturbation in the protein structure preventing it from folding properly and leading to degradation.[82] Alternatively, the protein can aggregate and cause the formation of inclusion bodies. Further, the *E. coli* may have an inability to support the inclusion of several recombinant proteins and machinery required to properly express fluorotyrosine incorporated cyt *c* with good yields.

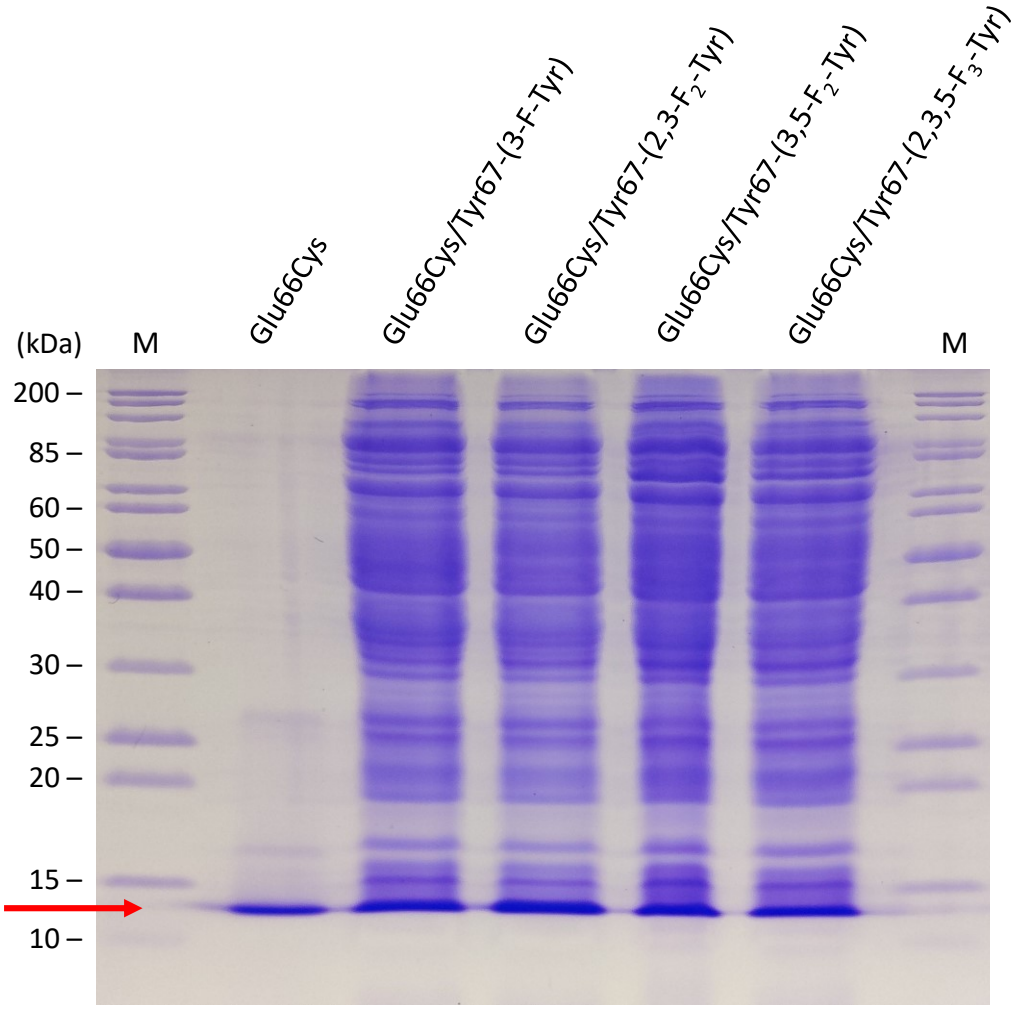

Figure 2.6. **Whole-cell lysate SDS-PAGE gel of expressions for cytochrome *c* Glu66Cys and Glu66Cys/Tyr67TAG incorporated with F_n-Tyr. Cells were transformed with both pETDuet-1-*ccmABCDEFGH/CYC1*$_{Glu66Cys/Tyr67TAG}$ and pEVOL-*F_nYRS-E3* plasmids. The red arrow indicates the band representing cyt *c* (~12.7 kDa).**

2.4. Conclusion

The project was the Warren group's first attempt to incorporate unnatural amino acids into metalloproteins. While cyt *c* is typically a robust platform for mutagenesis and related studies, it proved very challenging to work with in this application. First, the requirement for co-transformation of three plasmids, concomitant with plasmid incompatibilities required the development of a new plasmid system. This new system incorporated the cyt *c* gene, from our existing plasmid, and the cytochrome *c* maturation proteins, from the pEC86 plasmid. This new cyt *c* expression system streamlines and eliminates the need for co-transformation of plasmids for the expression of cyt *c*. I hope that this new plasmid is useful to other workers in the lab for future projects. Concerning the production of F_n-Tyr67 cyt *c*, the timing of induction appears to be important. It appears that proteins can be overexpressed, but the yields are low. If this project is to continue, a great deal of expression optimization will be necessary.

Chapter 3.

Revisiting the His62-Trp59 electron transfer pathway in cytochrome *c*

3.1. Introduction

The use of unnatural amino acids to modify the bridge energetics in the cyt *c* Cys66-Tyr67-Met80-heme ET pathway (Chapter 2) was hindered by very low protein expression levels. However, cyt *c* has other pathways, also highlighted in Chapter 2, that can be better understood using tools that have improved since those first studies. The work in this Chapter probes the effects of strategically placed substitutions that modify a single bond in the bridge. Specifically, I am interested in experimentally assessing how much a hydrogen bond can contribute to donor-acceptor electronic coupling in an intraprotein ET reaction.

3.1.1. Electron transfer pathways in cytochrome *c*

As outlined in Chapter 2, there are a series of well-known ET "pathway mutants" based on variants of cyt *c.* Five of these mutants are shown in Figure 2.1. There is a great diversity in the pathways that have been investigated. For example, the pathways that extend from His33 and His72 largely occur via covalent (σ) bonds and have a through-space jump near the heme. The differences in ET rates can be rationalized based on the arrangement of bonds between the donor and acceptor; the path from His33 is much longer, as enforced by the structure of the protein. Changing either of those pathways in a meaningful way would require an extensive mutagenesis campaign because covalent bonds must be changed. Structural studies would also be needed if stable protein could even be produced. In contrast, the ET pathway that extends from position 62 (His62 in the mutant shown in Figure 2.1 and Figure 3.1) is thought to be mediated via a series of σ bonds and two hydrogen bonds. Altering the nature of the hydrogen bonds along the pathway is more straightforward via conservative substitutions (see below). The work described in this Chapter probes how changing hydrogen bonds affects donor-acceptor coupling along what was thought to be an established ET pathway.

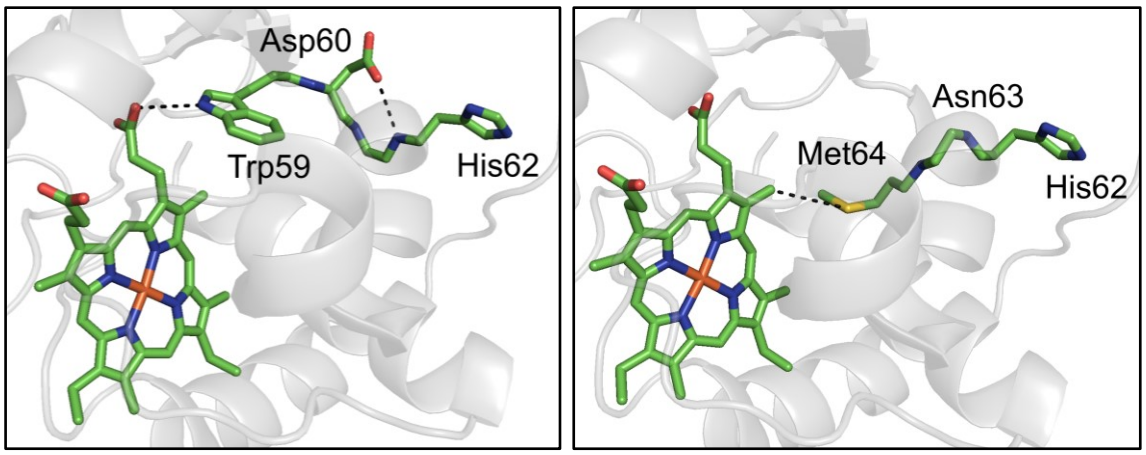

Figure 3.1. Yeast iso-1-cytochrome *c* favoured pathway leading from His62-Asp60-Trp59 to the iron heme with two hydrogen bonds shown as dashed lines (left). An alternative pathway is shown from His62-Asn63-Met64 to the iron heme with a through-space jump shown as a dashed line (right) (PDB 1YCC).

3.1.2. Pathway model recap

As outlined in Chapter 1, the rate of ET depends on the composition of the medium that separates a donor and an acceptor. The metric used to describe the level of electronic coupling via a given pathway is called H_{DA} (see above). Sigma (σ) bonds contribute the most to H_{DA}, which makes sense based on the orbital overlaps involved in forming covalent bonds. Through-spaced jumps are avoided, in general, because such steps are similar to tunneling through a vacuum. Intermediate between those extremes are hydrogen bonds. In pathways involving both covalent and hydrogen bonds, it may be possible to ascertain the importance of single hydrogen bonds by systematically removing them.

3.1.3. Project outline

In cyt *c*, the pathway of interest explores the case where two hydrogen bonds are present. The pathway begins at amino acid position 62 (yeast cyt *c* numbering) at the surface of the heme (Figure 3.1). There is a hydrogen bond between Asp60's carboxyl group to an amide in the peptide backbone and another between the NH group in the indole side chain of Trp59 to a heme propionate group. This pathway is favoured (indicated by computation) over a more direct pathway starting from position 62, via Met64, followed by a through-space jump to the heme.[83,84]

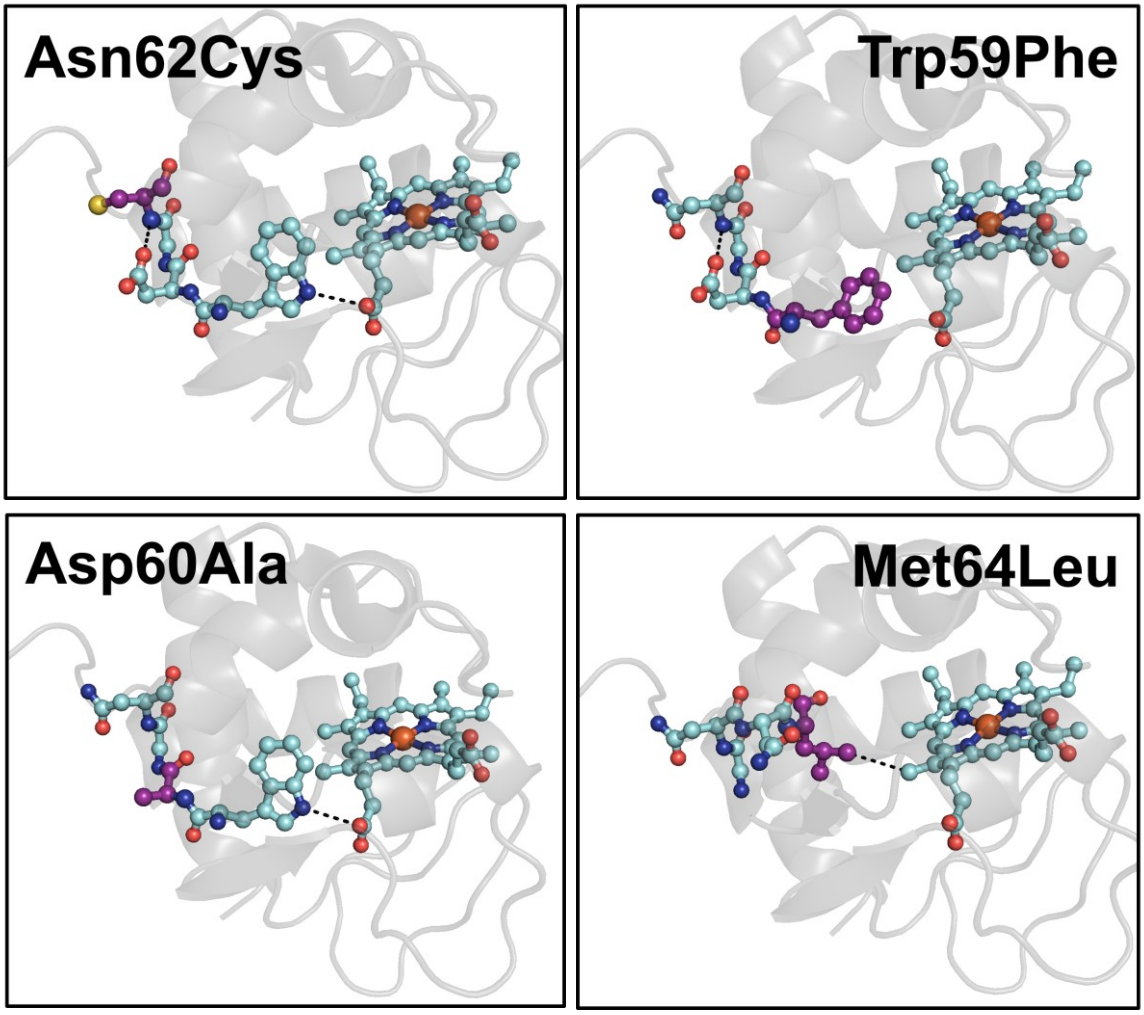

Figure 3.2. Proposed substitutions to yeast iso-1-cytochrome *c*. The surface cysteine created from Asn62Cys allows covalent labelling with a Ru(II) photosensitizer. Both Trp59Phe and Asp60Ala substitutions remove a hydrogen bond in the 62-60-59 pathway. The Met64Leu substitution increases the length of a through-space jump.

To alter the hydrogen bond characteristics, a series of substitutions have been incorporated to modify the residues participating in the interactions using site-directed mutagenesis (Figure 3.2). An Asp60Ala substitution was made which eliminated the carboxyl group of the aspartate side chain with the methyl side chain of alanine so no hydrogen bonding can occur with the backbone. A second set of substitutions were made to Trp59 including Trp59Tyr and Trp59Phe. In the former, changing the tryptophan to a tyrosine causes a change in the side chain from an NH to an OH hydrogen bond donor. For the latter, the phenylalanine contains a relatively unreactive benzyl group that is unable to form a hydrogen bond. The Met64Leu mutant was also produced as a means to confirm that the pathway containing a through-space jump was not operative. Lastly, to

perform flash-quench experiments to determine ET rates, an additional Asn62Cys surface substitution was created in all mutants to enable the covalent attachment of a ruthenium photosensitizer. The photosensitizer acts as an artificial electron acceptor from the donor heme iron, and, by using recently developed Cys reactive Ru complexes, we can investigate reactions that are driving force optimized.[85] This gives the best chance to clearly understanding how one or two hydrogen bonds influence intramolecular ET.

3.2. Experimental

3.2.1. Materials

Luria broth powder, yeast extract, ampicillin, chloramphenicol, and buffer salts were from BioShop Canada. Ruthenium trichloride was from Pressure Chemical, 2,2´-bipyridyl and 5,6-epoxy-5,6-dihydro-[1,10]phenanthroline from Sigma-Aldrich and 4,4´-dimethyl-2,2´-bipyridyl was from Alfa Aesar. Hexaammineruthenium(III) chloride was recrystallized before use from 40°C 1 M HCl. Water used was from a Barnstead EASYpure system (18 MΩ cm^{-1}). Gases were from Praxair Canada.

3.2.2. Synthesis of Ru(II) complexes

The compound [Ru(2,2´-bipyridyl)$_2$(5,6-epoxy-5,6-dihydro-1,10-phenanthroline)](PF_6)$_2$ was prepared following literature methods.[85,86] In 20 mL of 3:1 (v/v) ethanol: water, 400 mg cis-Ru(2,2´-bipyridyl)$_2Cl_2$ and 150 mg 5,6-epoxy-5,6-dihydro-1,10-phenanthroline ligand were added and refluxed in the dark for 3h. Following solvent removal, a saturated solution of NH_4PF_6 was added dropwise to precipitate the product. An orange precipitate was washed and collected by vacuum filtration. The Ru(II) complex was characterized by Ultraviolet–Visible (UV–Vis) spectroscopy, MALDI-TOF, and ^{1}H NMR.

[Ru(2,2´-bipyridyl)$_2$(5,6-epoxy-5,6-dihydro-1,10-phenanthroline)](PF_6)$_2$.
Orange solid. Yield: 570 mg, 82%. MALDI-TOF MS m/z = 609.19 $[M-H]^+$ (calculated: 609.11). ^{1}H NMR (500 MHz, acetone-d_6): δ (ppm) 5.07-5.12 (m, 2H), 7.51 (t, 1H, 6.6 Hz), 7.58-7.63 (m, 3H), 7.68 (dd, 1H, 5.7, 7.8 Hz), 7.74 (dd, 1H, 5.7, 7.7 Hz), 7.97 (d, 1H, 5.5 Hz), 8.07-8.11 (m, 4H), 8.17 (d, 1H, 5.6 Hz), 8.20-8.25 (m, 4H), 8.58 (dd, 2H, 4.3, 7.8 Hz), 8.80-8.85 (m, 4H).

For the preparation of [Ru(4-4´-dimethyl-2,2´-bipyridyl)$_2$(1,10-phenanthroline)](PF_6)$_2$, in 10 mL of 3:1 (v/v) ethanol : water, 100 mg of cis-Ru(4-4´-dimethyl-2,2´-bipyridyl)$_2Cl_2$ and 35 mg 1,10-phenanthroline ligand were added and refluxed in the dark for 3h. Following solvent removal, a saturated solution of NH_4PF_6 was added dropwise to precipitate the product. An orange precipitate was washed and collected by vacuum filtration. The Ru(II) complex was characterized by UV–Vis spectroscopy, MALDI-TOF, and ^{1}H NMR.

[Ru(4-4´-dimethyl-2,2´-bipyridyl)$_2$(1,10-phenanthroline)](PF_6)$_2$. Orange solid. Yield: 91 mg, 75%. MALDI-TOF MS m/z = 651.06 $[M+H]^+$ (calculated: 651.18). ^{1}H NMR (500 MHz, acetone-d_6): δ (ppm) 8.79, 8.78, 8.71, 8.66, 8.43, 8.42, 8.41, 8.39, 7.97, 7.96, 7.93, 7.92, 7.91, 7.90, 7.83, 7.82, 7.66, 7.65, 7.46, 7.45, 7.39, 7.37, 7.20, 7.18, 2.61, 2.56, 2.50.

For the preparation of [Ru(4-4´-dimethyl-2,2´-bipyridyl)$_2$(5,6-epoxy-5,6-dihydro-1,10-phenanthroline)](PF_6)$_2$, in 20 mL of 3:1 (v/v) ethanol : water, 100 mg of cis-Ru(4-4´-dimethyl-2,2´-bipyridyl)$_2Cl_2$ and 40 mg of 5,6-epoxy-5,6-dihydro-1,10phenanthroline ligand were added and refluxed in the dark for 3h. The solvent was removed and a saturated solution of NH_4PF_6 was added dropwise to precipitate the product. A dark orange precipitate was washed and collected by vacuum filtration. The Ru(II) complex was characterized by UV–Vis spectroscopy, MALDI-TOF, and ^{1}H NMR.

[Ru(4-4´-dimethyl-2,2´-bipyridyl)$_2$(5,6-epoxy-5,6-dihydro-1,10-phenanthroline)](PF_6)$_2$. Dark orange solid. Yield: 95 mg, 75%. MALDI-TOF MS m/z = 665.11 $[M-H]^+$ (calculated: 665.17) ^{1}H NMR (500 MHz, acetone-d_6): δ 8.80, 8.69, 8.66, 8.54, 8.24, 8.22, 8.15, 8.14, 8.05, 8.04, 7.89, 7.88, 7.83, 7.82, 7.73, 7.72, 7.71, 7.70, 7.67, 7.65, 7.64, 7.51, 7.41, 7.38, 7.31, 7.30, 5.08, 2.56.

3.2.3. Site-directed mutagenesis

S. cerevisiae iso-1-cytochrome *c* mutants were prepared using *CYC1* WT* cloned in pET20b vector (Novagen) between the NdeI and BamHI restriction sites. WT* contained two additional substitutions, Lys72Ala and Cys102Ser. The mutants Asn62Cys, Asn62Cys/Asp60Ala, Asn62Cys/Trp59Tyr, Asn62Cys/Trp59Phe, Asn62Cys/Asp60Ala/Trp59Tyr, Asn62Cys/Asp60Ala/Trp59Phe, and

Asn62Cys/Met64Leu were introduced into WT* using the Q5 High-Fidelity PCR Kit (New England Biolabs). All mutations were introduced by site-directed mutagenesis with PCR. See Appendix B for the forward and reverse primers used (Integrated DNA Technologies). PCR cleanup was performed using the Qiagen QIAquick PCR Purification Kit and template DNA digested with DpnI restriction enzyme (Thermo Scientific FastDigest) followed by another PCR cleanup. PCR reaction mixtures were transformed into chemically competent 5-alpha *E. coli* cells (New England Biolabs) and selected for on ampicillin-supplemented LB agar plates. Agar plates were incubated for 16 hours at 37°C. Single colonies were then grown with shaking for 16 hours at 37°C in liquid LB media with 100 µg/mL ampicillin. Plasmid DNA was purified from the cultures using the Qiagen QIAprep Spin Miniprep Kit. The sequences were verified using Eurofins Genomics SimpleSeq Sanger sequencing service.

3.2.4. Protein expression and purification

Mutant pET20b-*CYC1* plasmid and pEC86[73] plasmid containing *E. coli ccmABCDEFGH* genes were sequentially transformed into chemically competent BL21(DE3) *E. coli* (New England Biolabs) and incubated on ampicillin and chloramphenicol-supplemented LB agar plates for 16 hours at 37°C. Ten colonies were incubated with shaking in 75 mL LB with 100 µg/mL ampicillin and 25 µg/mL chloramphenicol for 7.5 hours (37°C, 180 rpm). Large-scale expressions of 10.5 L LB2YE, 100 µg/mL ampicillin, and 25 µg/mL chloramphenicol were inoculated with 63 mL of the starter culture. The cultures were incubated with shaking for 4.5 hours (37°C, 120 rpm) before decreasing the temperature and incubating for an additional 14.5 hours (30°C, 85 rpm). Cultures were harvested by centrifugation (4500 *g*, 10 min, 4°C) and pellets stored at –80°C prior to purification.

Cell pellets were resuspended in 100 mL lysis buffer containing 50 mM Tris, 1 mM EDTA, 1 mM PMSF, 10 mM β-mercaptoethanol, 1 mM sodium ascorbate, 1 µg/ml DNase I, and 1 mg/mL lysozyme at pH 8. Resuspension was sonicated for 6 minutes (Branson Digital Sonifier 250 Cell Disruptor) on ice and the supernatant was collected by centrifugation (24,000 *g*, 60 min, 4°C). The cyt *c* in the clarified lysate was purified with a CM Sepharose cation exchange column as follows. The column was pre-equilibrated with 10 mM Tris and 0.1 mM EDTA followed by loading the supernatant. The column was washed with 3 column volumes of lysis buffer containing 50 mM Tris, 1 mM EDTA, 1 mM

PMSF, 10 mM β-mercaptoethanol, and 1 mM sodium ascorbate (pH 8). Gradient elution was performed using a buffer of 20 mM Tris, 0.1 mM EDTA, and 0 to 250 mM NaCl (pH 8). Eluted protein containing cytochrome *c* was combined and exchanged into 5 mM sodium phosphate buffer at pH 7 by gel filtration with a PD-10 column (Cytiva) and concentrated by ultrafiltration (Amicon, 10 kDa). Protein purity was determined using UV–Vis spectrophotometry to compare the ratio between the Soret and 280 nm peaks. A 12% SDS-PAGE was also performed and stained with Coomassie Brilliant Blue R-250.

3.2.5. Mass spectrometry

MALDI-TOF was used to confirm the identity of the mutants. Data collection was performed using a Bruker microFLEX MALDI-TOF instrument. Unlabelled cytochrome *c* and $Ru(bpy)_2(phen)$ and $Ru(Me_2bpy)_2(phen)$ labelled cyt *c* samples were prepared for mass spectrometry (MS) analysis using $ZipTip_{C18}$ (Millipore) and eluted with 1:1 (v/v) acetonitrile : 0.1% trifluoroacetic acid (TFA) in water. Sinapinic acid was used as the MALDI matrix by mixing 1:1 (v/v) $ZipTip_{C18}$ eluted protein to a solution containing 30:70 (v/v) acetonitrile : 0.1% TFA in water saturated with sinapinic acid. The mixture was then deposited onto a Bruker MALDI Biotarget 48 target plate over a dried drop from saturated sinapinic acid in ethanol. Theoretical monoisotopic masses of the protein were calculated based on the DNA sequence using the ExPASy Compute pI/Mw tool.[75–77]

3.2.6. Optical spectroscopy

The pyridine hemochrome assay was performed according to literature methods to determine extinction coefficients.[41] Fe(III) spectra were recorded following the addition of 100 µL of cyt *c* to 2.9 mL of 50 mM NaOH, 20% pyridine, and 6 µL of 0.1 M potassium ferricyanide. Spectra were collected immediately and recollected at 2-minute intervals for 6 minutes. Solid sodium dithionite was then added to reduce Fe(III) to Fe(II)-cyt *c*, and the Fe(II) spectra were recorded similarly at 2-minute intervals for 6 minutes. Spectra were corrected by subtracting the baseline recorded for the solution before the addition of cyt *c*. Fe(III)-cytochrome *c* optical spectra in 5 mM sodium phosphate buffer at pH 7 were recorded using a Cary 100 Bio UV–Visible spectrophotometer. Excess solid L-ascorbic acid was then added to reduce Fe(III) to Fe(II)-cyt *c* and the spectra were recorded.

3.2.7. Circular dichroism spectroscopy

Far–UV circular dichroism spectra were collected using an Applied Photophysics Chirascan spectrometer. Fe(III)-cyt *c* CD spectra were collected at a concentration of 5 μM in 5 mM sodium phosphate buffer at pH 7. Afterwards, solid sodium dithionite was added to reduce Fe(III) to Fe(II)-cyt *c* and CD spectra were collected. The instrument reports circular dichroism in units of mdeg which was converted to molar ellipticity to correct for concentration. Protein secondary structure was estimated using the Beta Structure Selection (BeStSel) tool based on the far–UV CD spectra limited between 190-250 nm.[48,49] Similarly as a comparison, the Circular Dichroism analysis using Neural Networks (CDNN) tool was also used to deconvolute far–UV CD spectra between 185-260 nm.[47]

3.2.8. Electrochemistry

Electrochemical measurements were performed using a CH Instruments 6171B potentiostat. Cyclic voltammetry and differential pulse voltammetry experiments to determine cytochrome *c* $Fe^{3+/2+}$ reduction potentials consisted of a three-electrode cell with a gold disc working electrode (2 mm diameter), Pt wire counter electrode, and Ag/AgCl reference electrode with saturated KCl (CH Instruments). The gold working electrode was freshly treated with 4-mercaptopyridine prior to each CV and DPV experiment following literature methods.[87] Briefly, the gold electrode was immersed in ethanol for 10 minutes followed by polishing with 0.3 μm alumina water slurry for 5 minutes. The electrode was then treated in an ultrasonic pool of water for 10 minutes followed by immersion in a solution of 1 mM 4-mercaptopyridine for 30 seconds. All electrochemical measurements used potassium ferricyanide as an external standard with potentials referenced to the normal hydrogen electrode (NHE). Reduction potentials for cytochrome *c* were measured in 100 mM sodium phosphate buffer at pH 7. The measurement of oxidation potential for $[Ru(4\text{-}4'\text{-dimethyl-2,2}'\text{-bipyridyl})_2(1,10\text{-phenanthroline})](PF_6)_2$ complex by CV was performed using a three-electrode cell setup with an indium tin oxide (ITO) coated glass as the working electrode, basal plane graphite counter electrode, and Ag/AgCl reference electrode with saturated KCl. The compound was dissolved in 0.01 M H_2SO_4 electrolyte and $[Ru(bpy)_3]Cl_2$ was used as the external standard.

3.2.9. Kinetics

Cytochrome *c* mutants were first labelled with either [Ru(2,2´-bipyridyl)$_2$(5,6-epoxy-5,6-dihydro-1,10-phenanthroline)](PF$_6$)$_2$ or [Ru(4-4´-dimethyl-2,2´-bipyridyl)$_2$(5,6-epoxy-5,6-dihydro-1,10-phenanthroline)](PF$_6$)$_2$. For either label, 2.5 mL of 100 μM cyt *c* was exchanged into 100 mM Tris buffer at pH 8.5 by gel filtration. Solid dithiothreitol (DTT) was added in excess and the solution was incubated at 37°C with shaking for 1 hour. DTT was removed by exchanging into 100 mM Tris buffer at pH 8.5 by gel filtration. To this solution, 125 μL of 20 mM of either Ru(II) label dissolved in dimethylformamide was added dropwise and incubated at 20°C with shaking for 3 hours in the dark. The reaction was stopped and excess Ru(II) label was removed by gel filtration into 100 mM sodium phosphate buffer at pH 7. Before purifying, solid potassium ferricyanide was added. The Ru(II) labelled cyt *c* was purified by a fast protein liquid chromatography (FPLC) system (Pharmacia) with a HiTrap sulfopropyl Sepharose high-performance cation exchange column (Cytiva). A linear NaCl gradient was used for elution with 100 mM sodium phosphate buffer, pH 7 (Buffer A) and 100 mM sodium phosphate buffer with 500 mM NaCl, pH 7 (Buffer B). Fractions containing Ru-cyt *c* were combined and 15 equivalents of K_2CO_3 added. The solution was incubated for 1 hour at 20°C with shaking in the dark before being concentrated by ultrafiltration. Labelled protein was characterized with UV–Vis and MALDI-TOF. Yields were calculated based on comparing the amount of cyt *c* prior to the labelling reaction with labelled cyt *c* obtained following FPLC purification.

Before flash-quench experiments, (2,2´-bipyridyl)$_2$(5-cysteinyl-1,10-phenanthroline)Ru(II)-modified cyt *c* and (4-4´-dimethyl-2,2´-bipyridyl)$_2$(5-cysteinyl-1,10-phenanthroline)Ru(II)-modified cyt *c* solutions were reduced from Fe(III) to Fe(II) cyt *c* with excess L-ascorbic acid and desalted into 100 mM sodium phosphate buffer, pH 7 by gel filtration. Solutions of 1.5 mL of approximately 15 μM Ru-cyt *c* with or without 100 μL of 150 mM Ru(NH$_3$)$_6$Cl$_3$ quencher in 1 cm quartz cuvettes with a high vacuum valve sidearm were degassed with N_2 using pump/fill cycles. Time-resolved fluorescence spectroscopy was performed with and without quencher using a Nd:YAG laser pump pulse at 460 nm. Fluorescence emission was monitored for (2,2´-bipyridyl)$_2$(5-cysteinyl-1,10-phenanthroline)Ru(II)-cyt *c* samples at 620 nm and (4-4´-dimethyl-2,2´-bipyridyl)$_2$(5-cysteinyl-1,10-phenanthroline)Ru(II)-cyt *c* samples at 610 nm. Transient absorption (TA) spectroscopy experiments were performed with a Nd:YAG laser pump pulse at 460 nm

and probe at 550 nm with a Xe arc lamp. Rate constants were determined using MATLAB's Curve Fitting Toolbox following a two-exponential fit.

3.3. Results and discussion

3.3.1. Protein expression

Four new mutants of yeast cyt *c* and their Ru-modified variants were produced and characterized. Mutations were introduced using standard site-directed mutagenesis techniques to known WT* protein which included additional substitutions Lys72Ala and Cys102Ser. Sequencing was performed to verify mutations were present at the intended locations. As the wild-type yeast iso-1 cyt *c* protein contains a trimethyllysine post-translational modification at position 72, Lys72Ala prevents lysine coordination to the heme iron. Cys102Ser eliminates a surface cysteine, a site of potential cysteine-linked dimerization and prevents Ru(II) mislabelling. The successful expressions yielded pink *E. coli* pellets, an indication of cyt *c* overexpression as Fe(III) and Fe(II)-cyt *c* are red and pink, respectively. We attempted to investigate the Asn62Cys/Trp59Tyr and Asn62Cys/Asp60Ala/Trp59Phe mutants, but the proteins proved to be unstable and expression yields were modest. Attempts to express triple mutant Asn62Cys/Asp60Ala/Trp59Tyr were unsuccessful as *E. coli* growth slowed significantly. The origin of the dramatic decrease in protein stability in these mutants is not known.

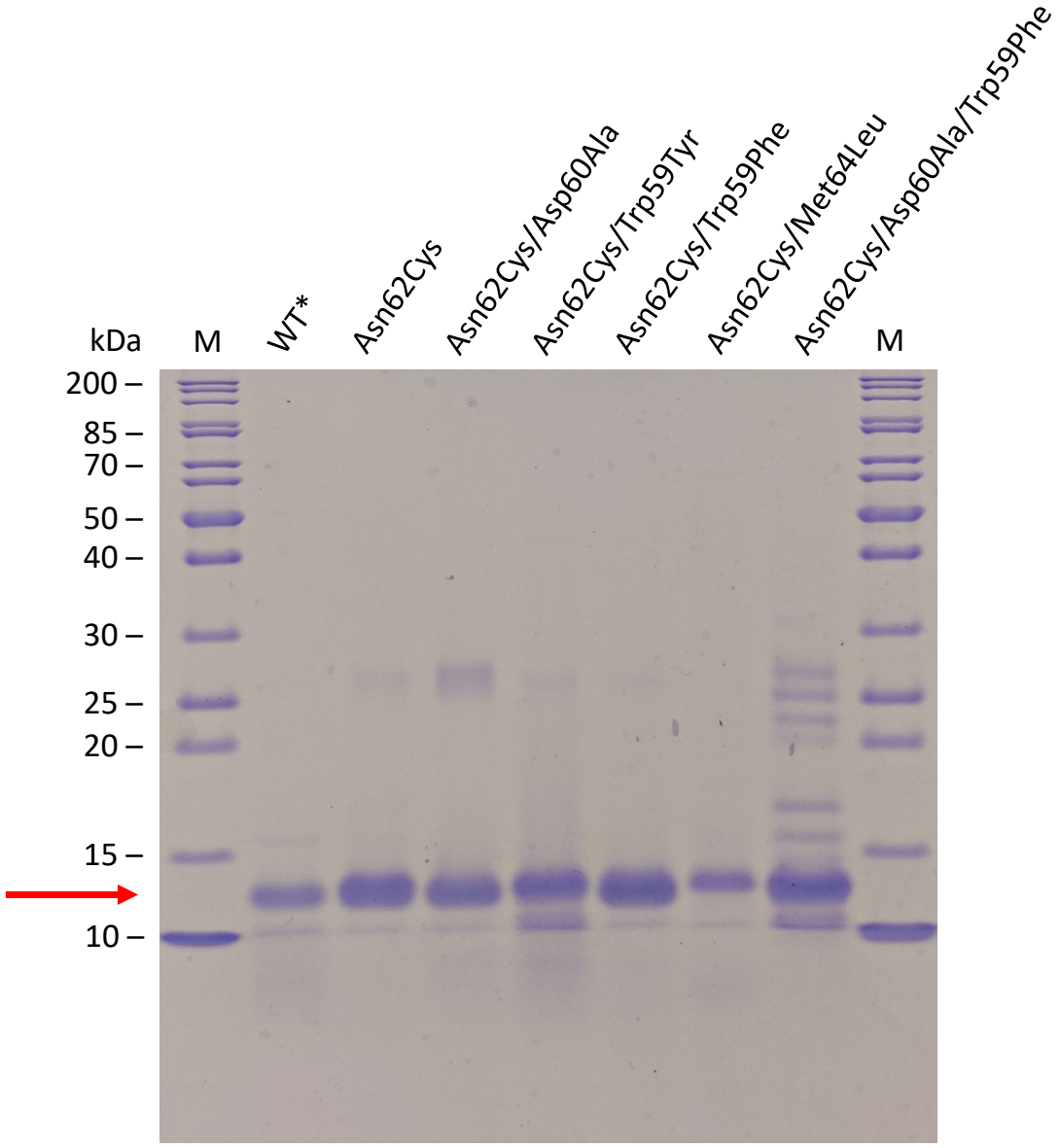

Figure 3.3. SDS-PAGE of purified Fe(II) yeast iso-1 cytochrome *c* WT* and variants. The red arrow indicates the band representing cyt *c* (~12.6 kDa).

Following purification using cation exchange chromatography, the identity and purity of each of the variant proteins were confirmed using SDS-PAGE (Figure 3.3) and MALDI-TOF mass spectrometry (Figure B.1 to B.7). The gel indicated the presence of a strong band at approximately 12.6 kDa, the expected average cyt *c* mass factoring in both the protein sequence and post-translational modifications. Further, MALDI-TOF mass-to-charge values were also in good agreement with calculated monoisotopic masses for all variants (Table 3.1).

Table 3.1. Unlabelled Fe(III) cytochrome *c* variant masses collected from MALDI-TOF mass spectrometry

Variant	Expected Average Mass (Da)	Expected Monoisotopic Mass (Da)	Obtained Monoisotopic Mass (Da)
WT*	12665.20	12655.29	12640.23
Asn62Cys	12654.23	12644.26	12647.57
Asn62Cys/Asp60Ala	12610.22	12600.27	12607.51
Asn62Cys/Trp59Tyr	12631.20	12621.24	12623.79
Asn62Cys/Trp59Phe	12615.20	12605.25	12609.31
Asn62Cys/Met64Leu	12636.20	12626.30	12640.23
Asn62Cys/Asp60Ala/Trp59Phe	12571.19	12561.26	12571.25

3.3.2. Optical spectroscopy

The heme content and extinction coefficient for the Asn62Cys, Asn62Cys/Asp60Ala, Asn62Cys/Trp59Tyr, Asn62Cys/Trp59Phe, Asn62Cys/Met64Leu, and Asn62Cys/Asp60Ala/Trp59Phe mutants were determined using the pyridine hemochromagen assay. The assay involves protein denaturation and replacement of the His18/Met80 axial ligands with pyridine (Figure B.16 and B.17). Despite different amino acid substitutions surrounding the heme moiety and the assay performed on intact covalently bound heme, it has been found that the surrounding protein environment has negligible effects on the absorption profile once the protein is denatured.[41] Spectra were collected at 2-minute intervals for 6 minutes following reduction with sodium dithionite to ensure complete reduction of Fe(III). No changes in the spectra were observed after 2 minutes.

None of the substitutions induce significant changes to the energy or the intensity of the electronic transitions of the proteins with respect to the WT* cyt *c* (Figure 3.4 and B.18). These include comparable absorption profiles for the Soret band ($S_0 \rightarrow S_2$ transition) ranging between 408 to 409 nm for Fe(III)-cyt *c* and 414 to 415 nm for Fe(II)-cyt *c*. The Fe(II)-cyt *c* Q-bands ($S_0 \rightarrow S_1$ transition) were also comparable to each other with wavelengths between 520 to 521 nm and 549 to 550 nm. The presence and similarity of the 695 nm sulfur to iron charge-transfer band for the mutants except for Asn62Cys/Trp59Tyr and Asn62Cys/Asp60Ala/Trp59Phe indicate that Met80 sulfur ligation to the iron is retained as it is for the WT* protein (Figure 3.5).

While the unstable Asn62Cys/Trp59Tyr variant did not display noticeable differences in the Soret and Q-bands, it did present a substantial red-shift to 704 nm for the charge-transfer brand. Any alterations to the charge-transfer band associated with Met80-iron ligation indicate changes in the integrity of the bond and subsequently the conformational state of the heme crevice.[88] With the addition of the Trp59Tyr mutation to Asn62Cys, a tryptophan that forms an H-bond with a heme propionate group was substituted with a tyrosine. Similar to tryptophan, the tyrosine can also H-bond to the propionate through the phenolic hydroxyl group. However, it likely caused a large enough disturbance at the heme prosthetic group that it inhibited the protein's ability to fold similarly to WT*. Complete absence of the charge-transfer band suggests loss of Met80 axial coordination which may be the case for the similarly unstable Asn62Cys/Asp60Ala/Trp59Phe triple mutant. It is unclear at this time what species may have replaced Met80 but in pH-induced studies of unfolding Met80 intact protein, a lysine from elsewhere has been found to coordinate from the heme coordination loop (residues 70−85) such as Lys73 and Lys79.[89,90] In urea-induced denaturation of Lys72Ala/Lys73Ala/Lys79Ala cyt *c*, His26 and His33 have instead been found replacing Met80 during the unfolding process.[91]

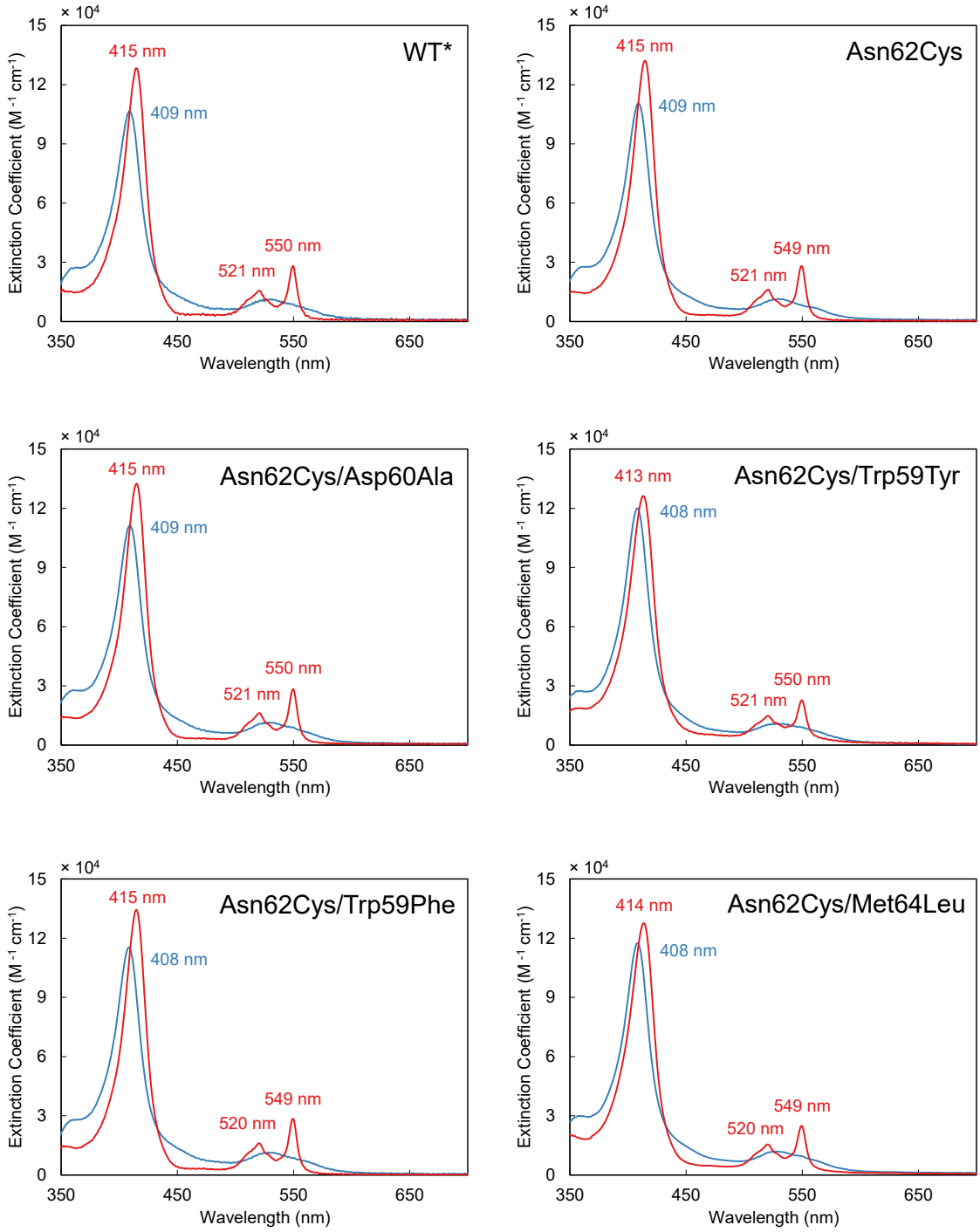

Figure 3.4. **Optical spectra of unmodified Fe(III) (blue trace) and Fe(II) (red trace) yeast iso-1 cytochrome *c* WT* and variants in 5 mM sodium phosphate at pH 7.0.**

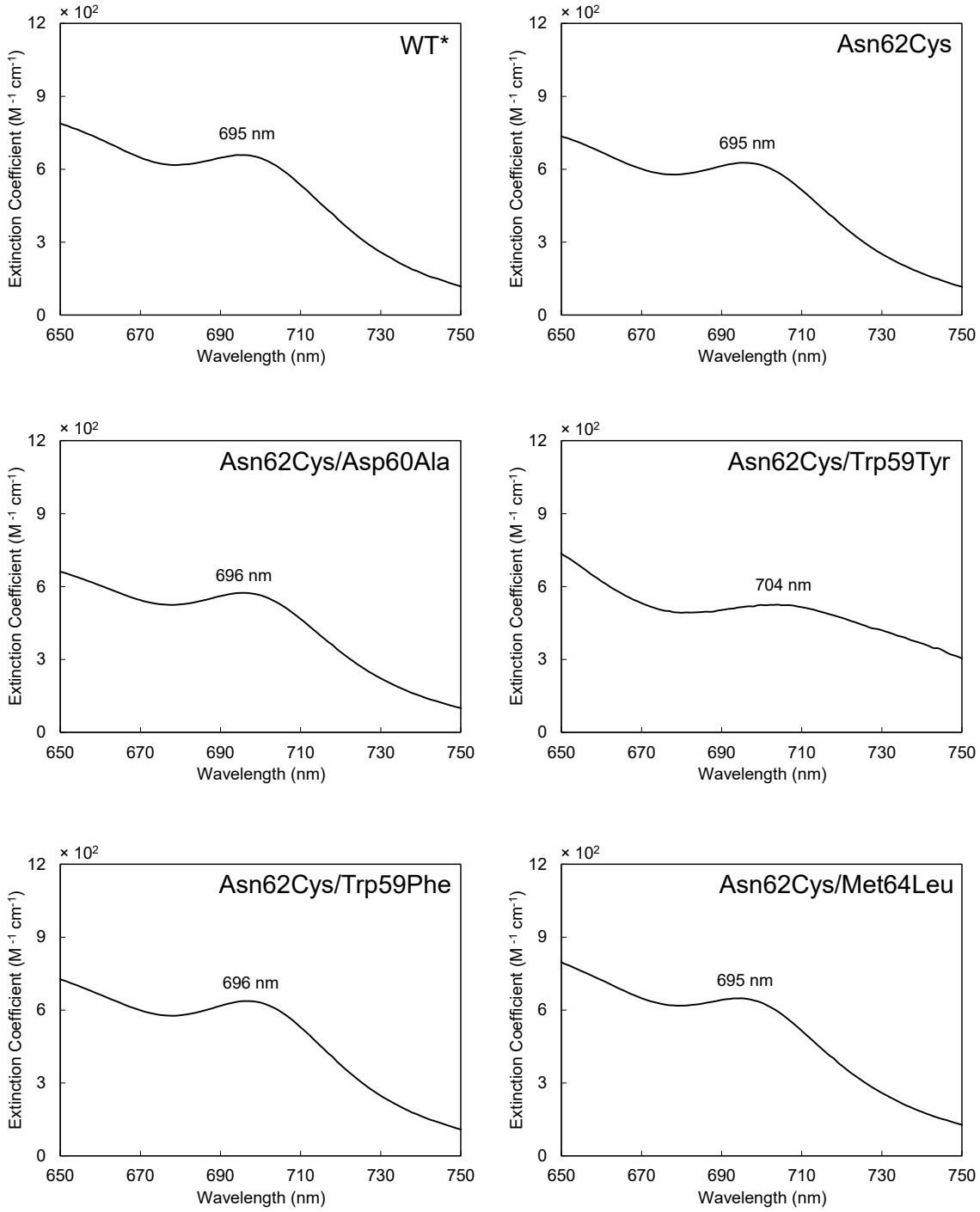

Figure 3.5. Optical spectra of the charge-transfer band from unmodified Fe(III) yeast iso-1 cytochrome *c* WT* and variants in 5 mM sodium phosphate at pH 7.0.

3.3.3. Circular dichroism spectroscopy

Far–UV circular dichroism spectra for unmodified Asn62Cys protein strongly resemble features reported in spectra for WT* in the literature for both energy and molar ellipticity (Figure 3.6).[92] The Asn62Cys, Asn62Cys/Asp60Ala and Asn62Cys/Trp59Phe mutants exhibit α-helical characteristic double minima at 220 nm (n → π* transition) and 208 nm (π → π* transition) for both Fe(III)-cyt *c* and Fe(II)-cyt *c.* A maximum was also observed at 194–195 nm (π → π* transition). The double minima for the Fe(III) form of Asn62Cys/Trp59Tyr while present, is distorted comparatively with a shift to 217 nm along with an increase in molar ellipticity and a reduction in molar ellipticity at 207 nm. Surprisingly, the Fe(II) form exhibited smaller shifts to 219 nm and 208 nm indicating the additional Trp59Tyr mutation affects the Fe(III) protein structure disproportionately. Further, there was a shift in the maximum to 192 nm and 193 nm for Fe(III) and Fe(II) respectively, accompanied by a large reduction in molar ellipticity. The result suggests that in line with UV–Vis spectrophotometric findings, there are minimal structural differences in both secondary and tertiary features upon insertion of the Asn62Cys mutation. Likewise, the Fe(III)-cyt *c* and Fe(II)-cyt *c* Asn62Cys/Asp60Ala and Asn62Cys/Trp59Phe spectra are also very similar indicating little perturbation upon removing H-bonding features in the pathway of interest. Unsurprisingly, given the red-shift in the charge-transfer band for the Asn62Cys/Trp59Tyr mutant, the Fe(III) and Fe(II) CD spectra were notably different from the others (Figure 3.5).

Estimates of discrepancies in secondary structure based on collected Fe(III) and Fe(II) CD spectra were examined with both CDNN and BeStSel tools. With CDNN, the secondary structures evaluated for Asn62Cys, Asn62Cys/Asp60Ala, and Asn62Cys/Trp59Phe were all closely aligned with each other based on predicted percentages (Table 3.2). Estimations did not vary much even between Fe(III) and Fe(II) forms. Analysis with BeStSel also produced similar results (Table 3.3). As the CD spectra produced two strong minima between 208–220 nm and a strong maximum at 194–195 nm, indicative of α-helical structure, the estimations of secondary structure unsurprisingly also suggested a predominance of α-helices. The Asn62Cys/Trp59Tyr variant had lower percentages of α-helical structure and greater parallel and anti-parallel structures owing to the differences in the CD spectra collected.

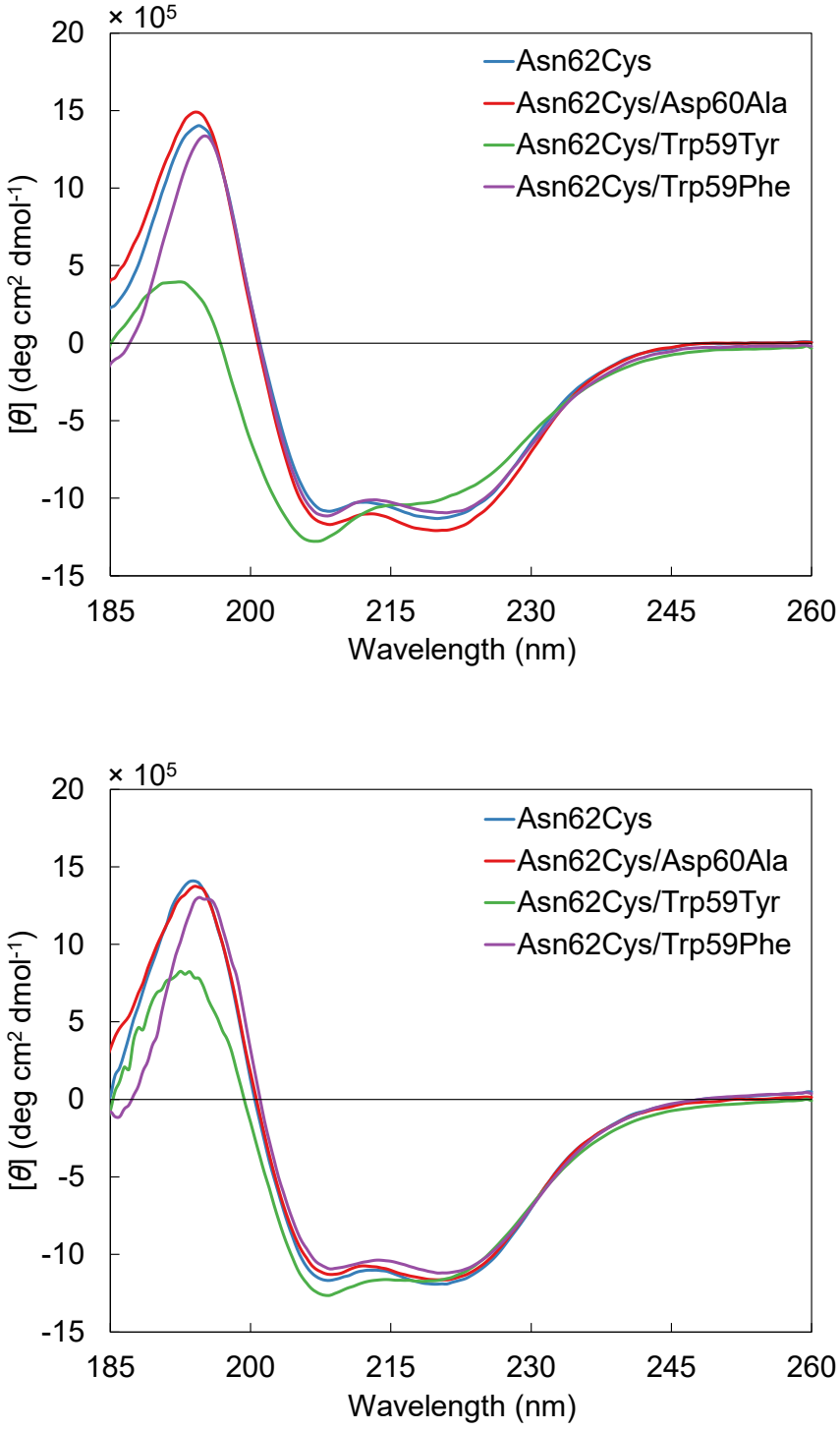

Figure 3.6. **Far–UV circular dichroism spectra of unmodified Fe(III) (top) and Fe(II) (bottom) yeast iso-1 cytochrome *c* variants in 5 mM sodium phosphate at pH 7.0.**

Table 3.2. Estimated percent secondary structure composition of Fe(III) and Fe(II)-cytochrome *c* analyzed with Circular Dichroism for Neural Networks[a]

	Structure	Asn62Cys	Asn62Cys/ Asp60Ala	Asn62Cys/ Trp59Tyr	Asn62Cys/ Trp59Phe
Fe(III)cyt *c*	Helix	29.7	31.3	25.2	28.9
	Antiparallel	12.9	11.4	25.3	14.3
	Parallel	9.1	8.6	9.2	9.2
	Beta-Turn	18.0	17.7	20.1	18.3
	Random Coil	32.8	31.1	29.6	32.8
	Total Sum	102.4	100.0	109.3	103.5
Fe(II)cyt *c*	Helix	30.4	30.4	28.0	28.8
	Antiparallel	12.6	12.4	17.4	14.2
	Parallel	8.8	8.8	8.9	9.3
	Beta-Turn	18.0	17.9	18.9	18.3
	Random Coil	31.3	31.7	30.5	33.2
	Total Sum	101.0	101.1	103.7	103.8

[a]Calculated using data from circular dichroism spectra between 185 to 260 nm in 5 mM sodium phosphate, pH 7.0.

Table 3.3. Estimated percent secondary structure composition of Fe(III) and Fe(II)-cytochrome *c* analyzed with Beta Structure Selection[a]

	Structure	Asn62Cys	Asn62Cys/ Asp60Ala	Asn62Cys/ Trp59Tyr	Asn62Cys/ Trp59Phe
Fe(III)cyt *c*	Helix	26.6	28.4	20.5	25.5
	Antiparallel	6.2	4.9	11.1	4.6
	Parallel	2.8	3.6	8.6	9.4
	Beta-Turn	15.4	15.7	15.3	14.4
	Others	49.0	47.4	44.5	46.1
	Total Sum	100.0	100.0	100.0	100.0
Fe(II)cyt *c*	Helix	26.8	26.1	20.4	23.3
	Antiparallel	2.9	2.8	8.7	4.2
	Parallel	4.1	4.2	10.5	10.5
	Beta-Turn	15.5	15.7	14.7	13.9
	Others	50.7	51.2	45.8	47.9
	Total Sum	100.0	100.0	100.1	99.8

[a]Calculated using data from circular dichroism spectra between 190 to 250 nm in 5 mM sodium phosphate, pH 7.0.

3.3.4. Electrochemistry

The redox properties of WT* and each cyt *c* variant were investigated using CV and DPV (Table 3.4). Cyt *c* was adsorbed on 4-mercaptopyridine self-assembled monolayers on the surface of a gold electrode. The pyridine nitrogen in 4-mercaptopyridine loosely interacts with cyt *c* through H-bond networks. Under the condition of 100 mM sodium phosphate at pH 7.0, CV and DPV reduction potentials for WT* were 0.289 V and 0.284 V, respectively. While it can be difficult to compare literature

values due to differing buffer compositions, the values are nearly identical within error to reported values of 0.286 V in 100 mM sodium phosphate buffer at pH 6.0 and 0.272 V in 100 mM sodium phosphate buffer at pH 7.4 collected by CV.[92] Measured WT* values were also similar to a reported WT value of 0.290 V.[89] In the absence of protein, no electrochemical response was observed.

Table 3.4. Reduction potentials[a] of cytochrome *c* variants from cyclic and differential pulse voltammetry

	E°' (V)[b]	E°' (V)[c]
WT*	0.289 ± 0.004	0.284 ± 0.006
Asn62Cys	0.289 ± 0.003	0.283 ± 0.002
Asn62Cys/Asp60Ala	0.286 ± 0.005	0.279 ± 0.006
Asn62Cys/Trp59Phe	0.276 ± 0.007	0.267 ± 0.007
Asn62Cys/Met64Leu	0.288 ± 0.003	0.281 ± 0.004

[a]Reduction potentials (vs. NHE) were recorded in 100 mM sodium phosphate at pH 7.0. [b]Reduction potentials obtained from cyclic voltammetry. [c]Reduction potentials obtained from differential pulse voltammetry.

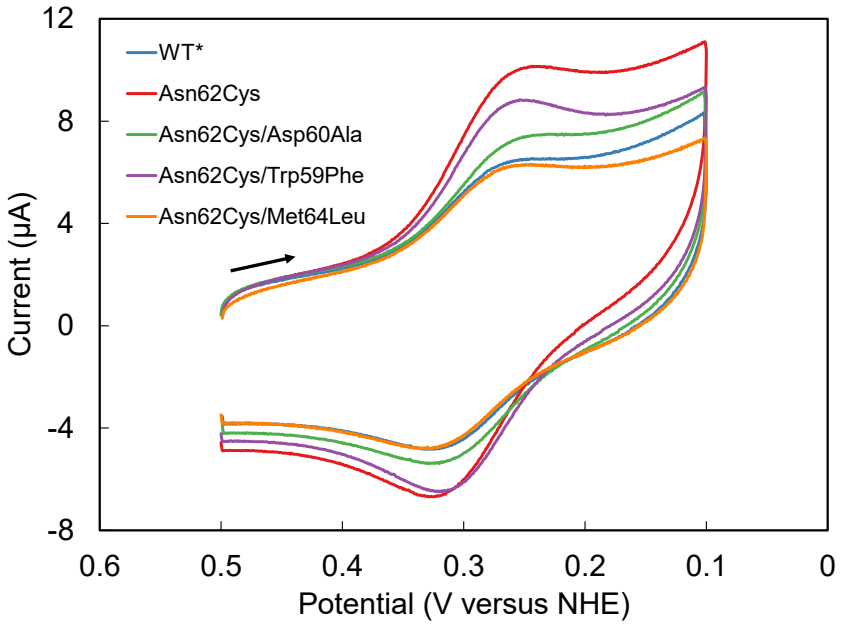

Figure 3.7. Cyclic voltammograms (CV) of 100-200 μM unmodified yeast iso-1 cytochrome *c* at the surface of a gold electrode coated with 4-mercaptopyridine. All CVs were recorded with a scan rate of 100 mV/s in 100 mM sodium phosphate at pH 7.0. The arrow shown indicates the scan direction.

All variants of interest have remarkably similar Fe^{III}/Fe^{II} reduction potentials from CV suggesting that the substitutions have little effect on altering the heme environment

(Figure 3.7). A decrease in reduction potential has been associated with an increase in solvent exposure of the heme for *c*-type cytochromes.[6,93–95] The standard redox potentials collected from CV compared to DPV were also very similar (Figure 3.8). While the variant Asn62Cys/Trp59Phe had a downward shift of 13 mV from CV and 17 mV from DPV relative to WT*, the difference is negligible and any changes in heme solvent exposure minimal. For reference, a reduction of 13 mV and 17 mV corresponds to an estimated 0.9% and 1.1% increase in solvent exposure, respectively.[93]

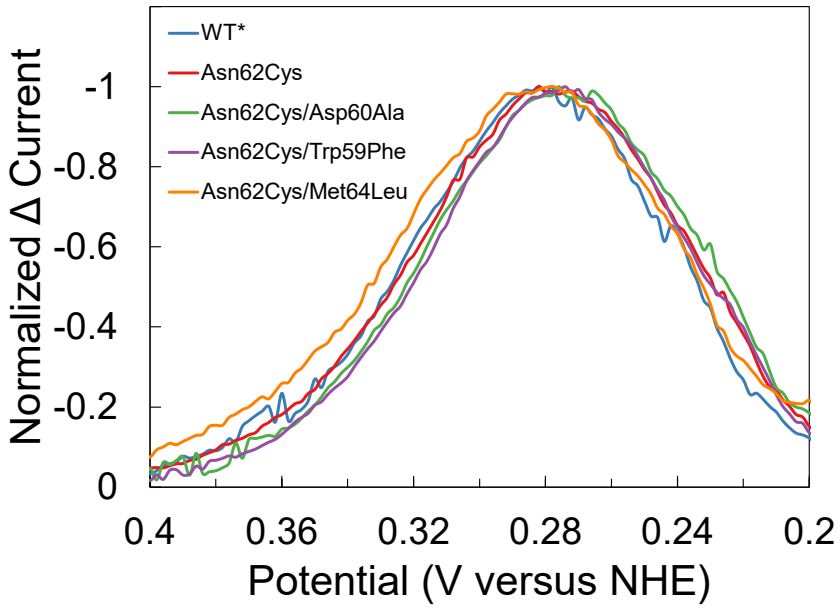

Figure 3.8. Normalized differential pulse voltammograms (DPV) of unmodified cyt *c* in 100 mM sodium phosphate at pH 7.0. DPV parameters: scan rate, 20 mV/s; pulse width, 100 ms; and amplitude, 25 mV.

Of note, no clear peaks were observed at positive reduction potentials for the Asn62Cys/Trp59Tyr and Asn62Cys/Asp60Ala/Trp59Phe mutants from CV and DPV experiments. In mutants with a dramatic change in the heme environment such as loss of axial heme iron Met80 coordination in the Met80Ala/Cys102Thr mutant, a decrease of nearly 500 mV has been observed relative to WT* ($E^{\circ\prime}$ = –0.194 V vs. NHE).[96] In this case, based on structural data, a cavity is created near the distal heme site with coordination of an OH^- ion and minimal perturbance of nearby residues.[97] In wild-type (WT) protein, urea denaturation studies showed that unfolding of the protein during which Met80 is replaced by His26 or His33 causes the reduction potential to decrease by nearly 500 mV as well

($E°'$ = –0.244 V vs. NHE).[91] Compounding evidence based on optical spectroscopy, circular dichroism spectroscopy, and electrochemistry suggests that both the Asn62Cys/Trp59Tyr and Asn62Cys/Asp60Ala/Trp59Phe mutants are unlikely to maintain the same fold as Asn62Cys, Asn62Cys/Asp60Ala, Asn62Cys/Trp59Phe, and Asn62Cys/Met64Leu. Further experiments may be performed to determine the presence of reduction peaks with negative potentials for these two mutants.

3.3.5. Ru(II) labelling

To investigate ET reactions in a driving force optimized ($-\Delta G° = \lambda$) regime, we created the yeast cyt *c* mutants to allow for labelling with a ruthenium tris(diimine) complex. In contrast, $Ru(bpy)_2(imidazole)_2$ used in the past occur at a lower driving force. Analogous to the Ru-His62 protein systems, the native Asn62 was converted to Cys using site-directed mutagenesis. The only other surface cysteine residue available in the WT protein was mutated from Cys102 to Ser in WT*, allowing for site-specific labelling at Cys62. Two other cysteine residues, Cys14 and Cys17 are covalently linked to the heme through thioether bonds.

The new Asn62Cys proteins were modified with two different Cys-reactive labels (see Experimental Section): $Ru(bpy)_2$(epoxy-phen) or $Ru(Me_2bpy)_2$(epoxy-phen). The resultant proteins were purified following a modified protocol for P450 BM3.[85] All mutants were bioconjugated at the Cys62 thiol side chain with either label through opening of the epoxy ring followed by β-hydroxy cysteinyl formation. Potassium carbonate was then used to allow for dehydration and aromatization of the label.

It is worth noting that, while the labels were prepared according to the literature, their ^{1}H NMR spectra were complex. The spectra are set out in Appendix B.23–B27. The Cys-reactive 5,6-epoxy-5,6-dihydro-[1,10]phenanthroline has two potential isomers when ligated to Ru and the Ru complex itself has two isomers (Δ and Λ). The former isomers are removed on aromatization of the phen ring on reaction with Cys, but the Δ and Λ isomers remain. In practice, these are never isolated for studies of this nature and the redox properties of the isomers are invariant.

Successful bioconjugation for Asn62Cys, Asn62Cys/Asp60Ala, Asn62Cys/Trp59Phe, and Asn62Cys/Met64Leu was seen with a change in colour of the

purified Fe(II)Ru-cyt *c* from pink to orange (Figure 3.9). Yields were in the range of 25 to 45% depending on the variant and label used. Additionally, MALDI-TOF mass spectrometry experiments demonstrated an appropriate mass shift in the m/z values of the different variants (Table 3.5 and Figure B.8 to B.15). The labelled proteins were characterized by UV–Vis. All variants had near-identical electronic transition energies and intensities as Asn62Cys (Figure B.31). Further, in comparison to unlabelled proteins, the optical spectra for the Soret and Q-bands were also near-identical indicating the modified proteins have maintained proper folding (Figure 3.10 and 3.11). The appearance of a shoulder was seen at approximately 460 nm for $Ru(bpy)_2(phen)$ and 470 nm for $Ru(Me_2bpy)_2(phen)$ labelled proteins corresponding to metal-to-ligand charge-transfer for Ru(II). The shoulder was expected for both labels due to absorption in the region with the free labels (Figure B.28 and B.30).

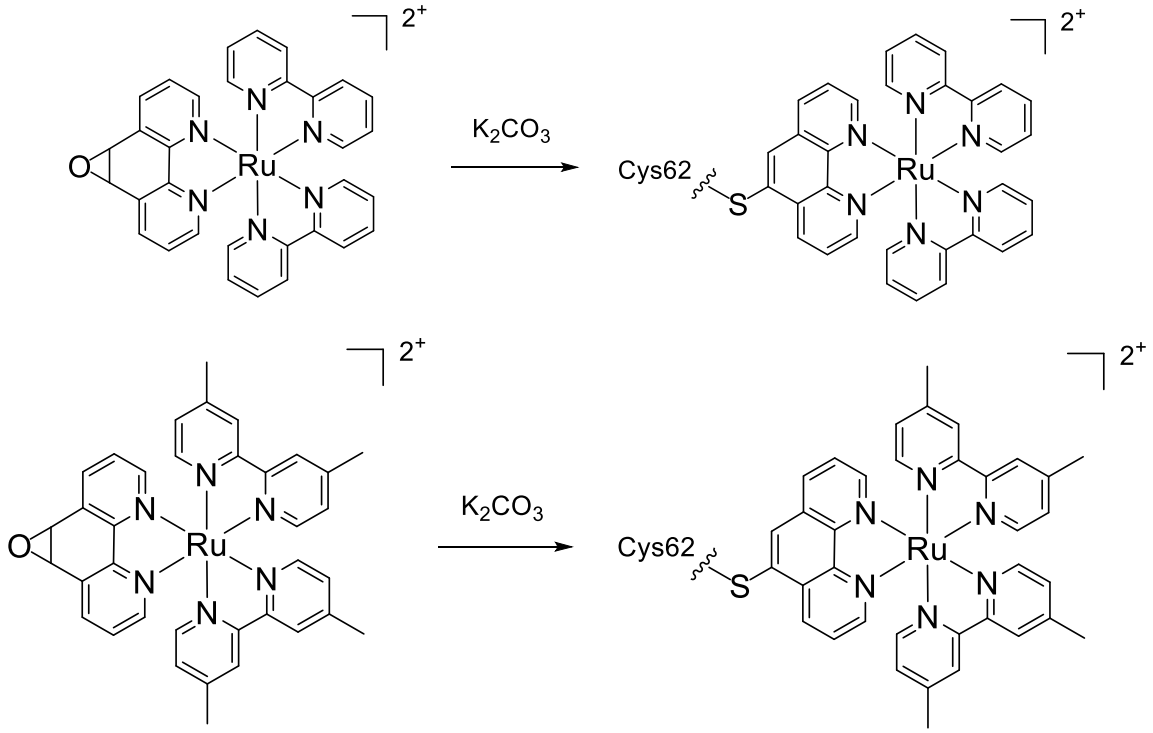

Figure 3.9. Bioconjugation of (2,2´-bipyridyl)$_2$(5-cysteinyl-1,10-phenanthroline)Ru(II) (top) and (4-4´-dimethyl-2,2´-bipyridyl)$_2$(5-cysteinyl-1,10-phenanthroline)Ru(II) (bottom) to yeast iso-1 cytochrome *c* Asn62Cys variants. The covalently bound sulfur shown is part of the Cys62 side-chain.

In the case of Fe(II)Ru-Asn62Cys/Trp59Tyr, conjugation of both Ru(II) labels appeared to be unsuccessful. For $Ru(bpy)_2(phen)$ labelled, there did not appear to be the

appearance of a shoulder at 460 nm as expected in the UV–Vis absorption spectrum (Figure B.32). Addition of sodium ascorbate was unable to reduce the heme to Fe(II) unlike other mutants as evident by the lack of a red-shift in the Soret and appearance of Q-bands at 521 and 550 nm. The Asn62Cys/Trp59Tyr mutant labelled with $Ru(Me_2bpy)_2(phen)$ appeared to show a marked increase in absorption at 470 nm indicative of conjugation (Figure B.33). Addition of sodium ascorbate was able to convert a small percentage of species from Fe(III) to Fe(II) as seen by the appearance of Q-bands at 521 and 549 nm but with lower than expected absorption intensities. The expected red-shift in the Soret band for both Ru(II) labelled Asn62Cys/Trp59Tyr mutants was also not seen. Expected masses as characterized by MALDI-TOF were also not readily apparent.

Table 3.5. Ru(II)-cytochrome *c* variant masses collected from MALDI-TOF mass spectrometry

Label	Variant	Expected Monoisotopic Mass (Da)	Obtained Monoisotopic Mass (Da)
$Ru(bpy)_2(phen)$	Asn62Cys	13147.30	13155.36
	Asn62Cys/Asp60Ala	13103.31	13115.92
	Asn62Cys/Trp59Phe	13108.29	13118.00
	Asn62Cys/Met64Leu	13129.34	13136.11
$Ru(Me_2bpy)_2(phen)$	Asn62Cys	13203.36	13218.60
	Asn62Cys/Asp60Ala	13159.37	13171.23
	Asn62Cys/Trp59Phe	13164.35	13175.28
	Asn62Cys/Met64Leu	13185.40	13209.57

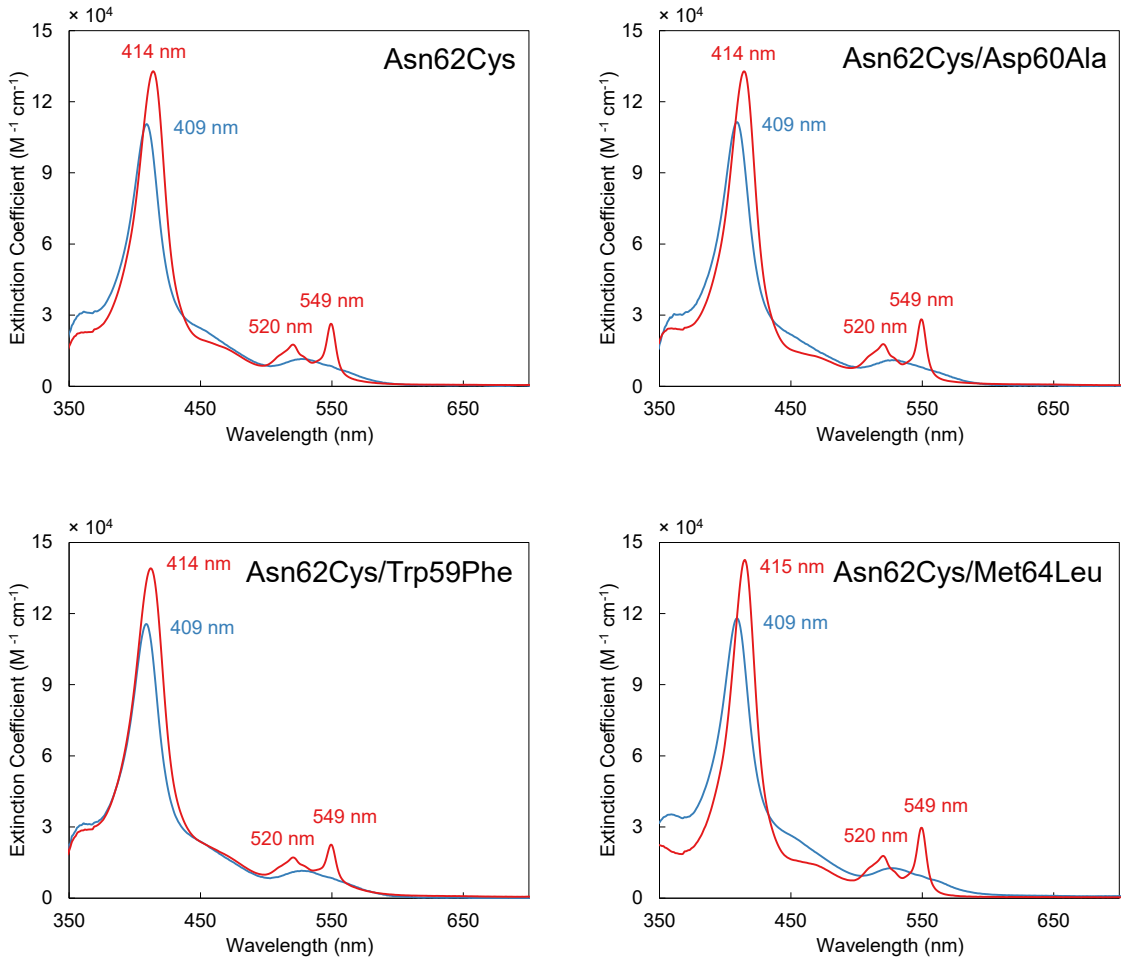

Figure 3.10. Optical spectra of (2,2´-bipyridyl)$_2$(5-cysteinyl-1,10-phenanthroline)Ru(II)-modified yeast iso-1 cytochrome *c* variants in the Fe(III) (blue trace) and Fe(II) (red trace) oxidation states. Spectra were recorded in 5 mM sodium phosphate at pH 7.0.

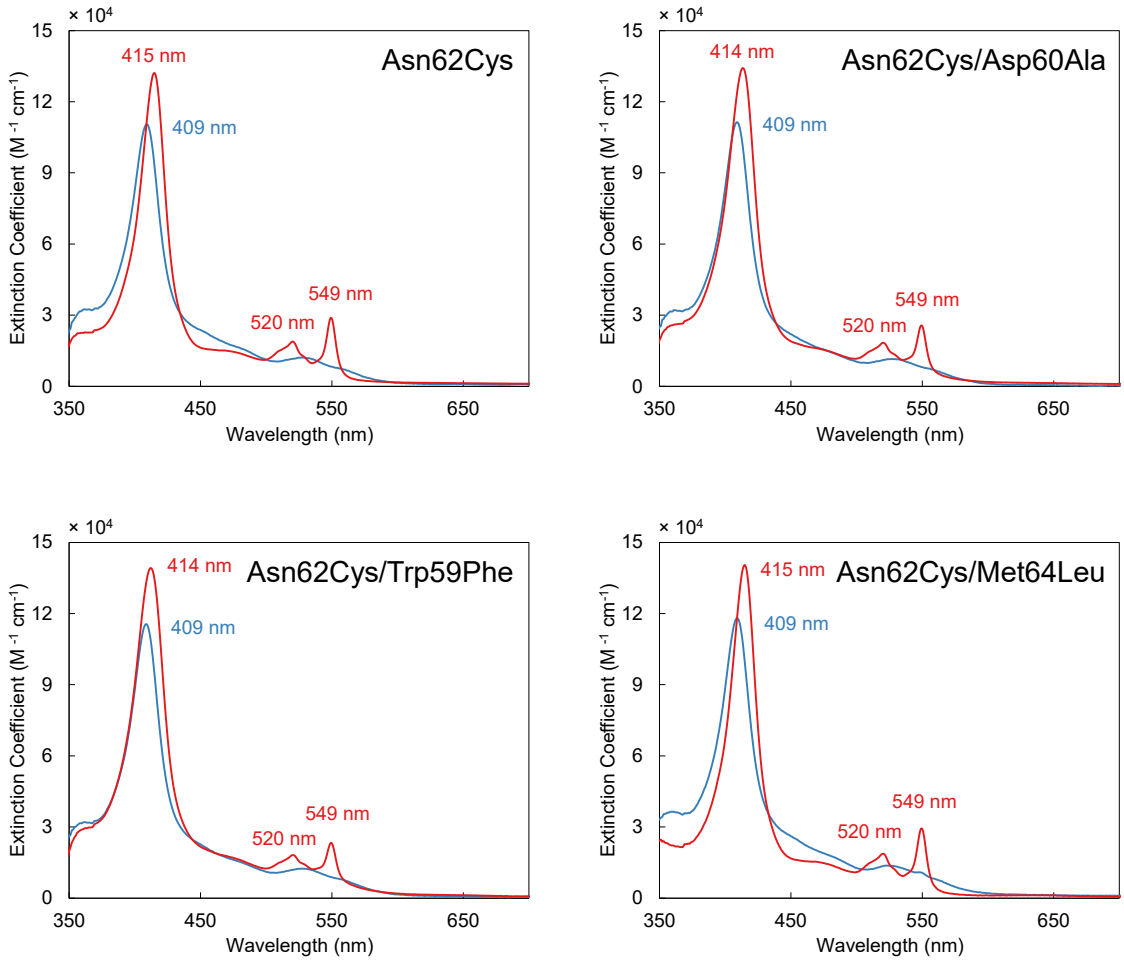

Figure 3.11. Optical spectra of (4-4´-dimethyl-2,2´-bipyridyl)$_2$(5-cysteinyl-1,10-phenanthroline)Ru(II)-modified yeast iso-1 cytochrome *c* variants in the Fe(III) (blue trace) and Fe(II) (red trace) oxidation states. Spectra were recorded in 5 mM sodium phosphate at pH 7.0.

3.3.6. ET kinetics

ET kinetics were explored in each of the Asn62Cys, Asn62Cys/Asp60Ala, Asn62Cys/Trp59Phe, and Asn62Cys/Met64Leu mutants using time-resolved laser spectroscopy. In all cases, a flash quench scheme (Figure 1.2) was used to generate protein-tethered Ru(III) oxidants. The quencher used was $[Ru(NH_3)_6]Cl_3$. The normalized kinetics traces for all of the mutants with the two different labels are shown in Figure 3.12 and the individual traces are shown in Appendix B.34 and B.35. The traces are single wavelength traces at 550 nm that follow the oxidation of Fe(II)-cyt *c* by the flash-quench generated Ru(III) oxidant. The data show that Asn62Cys, Asn62Cys/Asp60Ala, and Asn62Cys/Trp59Phe follow similar curves unlike that of Asn62Cys/Met64Leu for both

Ru(II) labels. A summary of the rate constants and ET driving forces are tabulated in Table 3.6.

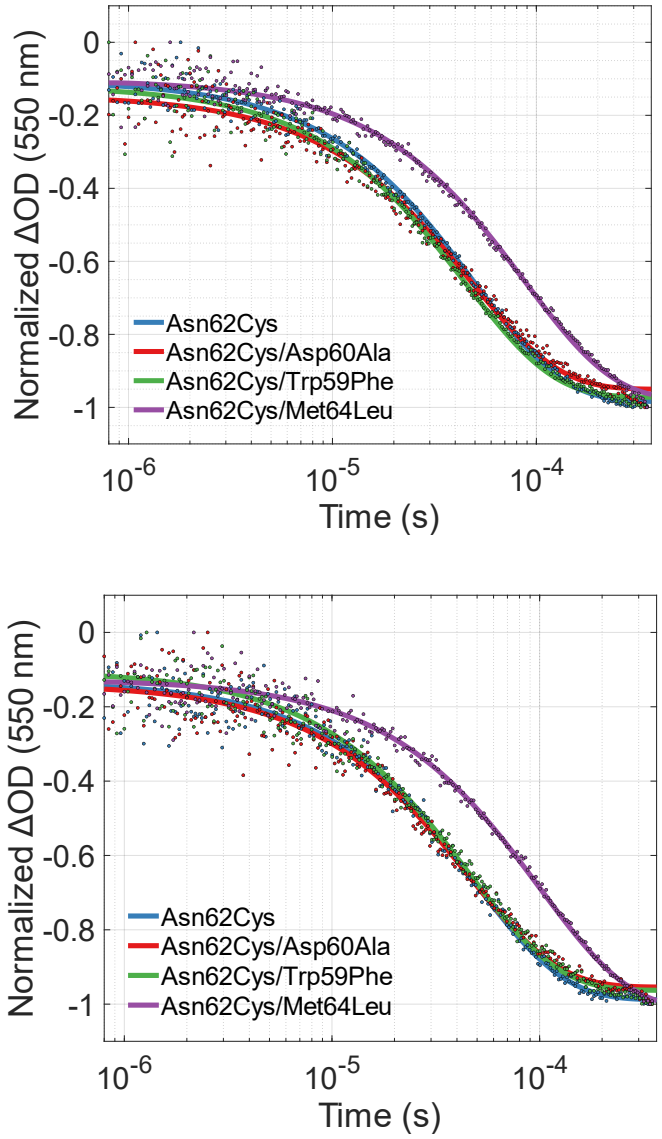

Figure 3.12. Normalized kinetic traces to values between 0 and –1 (dots) and fits (solid lines) for Ru(bpy)$_2$(phen) (top) and Ru(Me$_2$bpy)$_2$(phen) (bottom) labelled cytochrome *c* mutants.

Table 3.6. Thermodynamic and kinetic parameters of Ru(bpy)$_2$(phen) and Ru(Me$_2$bpy)$_2$(phen) labelled cytochrome *c* mutants

	$\Delta G°$ (bpy)	logk (bpy)	$\Delta G°$ (Me$_2$bpy)	logk (Me$_2$bpy)
Asn62Cys	–0.98	4.36±0.07	–0.85	4.29±0.03
Asn62Cys/Asp60Ala	–0.98	4.36±0.04	–0.85	4.32±0.04
Asn62Cys/Trp59Phe	–0.99	4.36±0.02	–0.86	4.35±0.02
Asn62Cys/Met64Leu	–0.98	4.13±0.06	–0.85	4.04±0.06

3.3.7. Analysis of electron transfer rate constants and pathways

The most striking result from the data shown in Table 3.6 is that elimination of either hydrogen bond involving Asp60 or Trp59 causes no change in the ET rate constant. We predicted that removing these interactions would slow heme to Ru(III) ET by decreasing H_{DA}.[1] This decrease could either result from the introduction of a through-space jump along the known position62-heme ET pathway or by forcing the pathway along a longer network of covalent bonds. However, the data indicate that this pathway is not operative and the relevant pathway involves ET along Asn63 and Met64. Mutation of Met64 to Leu causes a factor of 2 decrease in the ET rate constant. The pathway involves a series of covalent bonds followed by a through-space jump between Met64 and the heme edge.

The reactions investigated here occur at high driving forces. Based on the reorganization energy of cyt *c* (0.8 eV)[24,98] and that of $Ru(bpy)_3^{3+/2+}$ (1.3. eV),[12,99,100] we estimate the overall reorganization energy (λ) for ET from cyt *c*-Fe(II) to Ru(III) to be 1 eV using the additivity postulate (see Chapter 1). Work using photosensitizers based on $Ru(bpy)_2(imidazole)_2$ showed a λ value near 0.8 eV, while these using a Ru-label with a larger intrinsic λ showed a value of over 1.2 eV.

Using the above value for λ and the observed rate constants, we can estimate values for H_{DA} in WT* and Met64Leu cyt *c*. Taking the close contact value H_{AB}^0 = 186 cm^{-1}, our estimates for H_{DA} are 0.009 and 0.007 cm^{-1} for Ru-WT* and Ru-Met64Leu, respectively. The values were calculated using the rate data for the $Ru(bpy)_2(phen)$ label since it is close to being driving force optimized (i.e., $-\Delta G° = \lambda$). PyMOL-generated models (Figure 3.13) suggest that the Met64Leu mutation increases the through-space jump between residue 64 and the heme by 0.6 Å (i.e., 3.3 Å for Met64 and 3.9 Å for Leu64). At a fixed distance, which assumes that the mutation does not dramatically affect protein dynamics on the ET timescale, this change in H_{DA} corresponds to a 0.03 $Å^{-1}$ change in the distance decay constant β (see Chapter 1). Given the exponential distance dependence for ET reactions, these very small changes in through-space jump distances can affect ET

[1] For a more detailed explanation of H_{DA} and its importance, the interested reader should consult Chapter 1.

rates in a big way. In the current system, the distance changes result in a factor of 2 difference in ET rate constant.

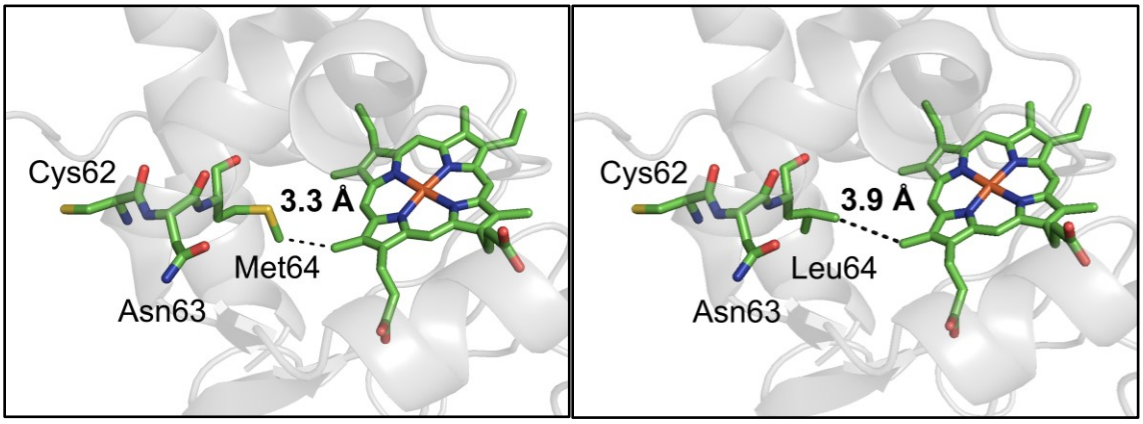

Figure 3.13. Comparison of the through-space jumps involved in ET along the position 62-63-64 pathway in cyt *c*. The Ru label is at position 62 in the Asn62Cys mutant. The dashed line and corresponding distance show the close contact distance between residue 64 and the heme edge. Hydrogens were not included in the distance calculations.

An important limitation of the above analysis based on X-ray structure distances is that only the locations of non-hydrogen atoms are known with any degree of certainty. It is possible to add hydrogens programmatically in PyMOL, but their locations are not optimized. Doing so, in this case, results in a larger change in the position 64 to heme through-space jump (1.0 Å, 1.8 Å for Met64 and 2.8 Å for Leu64). In addition, this purely structure-based analysis ignores the fundamental differences in Met and Leu. While both residues can be classified as “hydrophobic,” the polarizability of Met is much greater than that of Leu. There likely exists a dipolar interaction between the δ^- Met-sulfur and the δ^+ of the edge of the heme. Ultimately, a computational comparison of these pathways will yield greater insight into these electronic effects, as well as any changes to protein dynamics.

3.4. Conclusion

A series of Ru-modified cyt *c* variants have been produced and characterized. At the outset, the goal of this project was to elucidate the role of the two hydrogen bond-mediated ET steps in a long-standing ET pathway in cyt *c*. The pathway had been proposed to occur along a peptide section from position 62 to Trp59. However, removal of either of the hydrogen bonds (i.e., in the Asp60Ala or Trp59Phe mutants) induced no

change in the observed rate of ET from Fe(II)-heme to a flash-quench-generated Ru(II) oxidant. A mutation to an alternative pathway that was previously discounted, that is the Met64Leu mutation, slowed the rate of ET by a factor of two. The donor-acceptor distance in the WT* and Met64Leu proteins are expected to be the same, so the observed change in ET rate is due to changes in the donor-acceptor electronic coupling.

This study revisited an established ET system based on cyt *c* and showed that one of the proposed pathways is probably not operative, at least in the Ru-Cys62 driving force-optimized model investigated here. This study also provides a systematic model to understand the quantitative effects on ET rate constant (k_{ET}) from increasing the distance of a through-space jump. We also suspect that the differences in the physical properties (e.g., polarizability) of Met and Leu may play roles in electronic coupling in this system. A computational analysis of the ET pathway is underway at this time in collaboration with Prof. David Beratan (Duke University).

Chapter 4.

Exploring a tyrosine microenvironment in *Pseudomonas aeruginosa* azurin using fluorinated tyrosines

4.1. Introduction

Elucidating the properties of a single amino acid in a protein is a great challenge. In some proteins, single amino acids can play special roles, in particular at and around enzyme active sites. Examples that have received special attention include, Tyr161 in photosystem II, Trp59 in cytochrome *c* peroxidase, and Tyr122 in *E. coli* ribonucleotide reductase.[101] In all of the above examples, the amino acid is redox-active, cycling between its closed-shell configuration and the corresponding 1-electron oxidized radical. Open- and closed-shells are defined by a valence shell that is either not fully filled with electrons or fully filled, respectively. This mode of reactivity of amino acid side chains, reminiscent of the redox cycling in a transition metal, is crucial for life and has generated a body of research congruent with this importance. While a great deal of work emerged in the mid-1900s, new roles and thinking about amino acid radicals continues to emerge.[102,103] The goal of the work in this Chapter is to produce robust protein systems where the physical properties for protein-embedded tyrosine can be elucidated.

The use of unnatural amino acids has substantially aided researchers' ability to investigate unique properties of proteins. This includes a wide range of uses, from probing features of enzyme active sites[104] to generating modified proteins *in vivo* to investigating protein regulation and dysregulation.[105] One exceptional example of how unnatural amino acids can be used to probe enzymatic mechanisms is Stubbe's incorporation of nitro-, amino,- and fluorotyrosine amino acids into ribonucleotide reductase.[106–109] In short, this 10-year series of studies revealed unprecedented details about the kinetics and thermodynamics of electron transport in ribonucleotide reductase. Part of the success of this study was the detailed investigation of the physical properties of the site-selectively incorporated tyrosine residues. These are landmark studies but are specific to the unique tyrosine sites in ribonucleotide reductase. Given the widespread importance of tyrosine, it

is desirable to investigate a simple protein system where properties of unnatural tyrosine residues could be probed.

4.1.1. Project outline

In order to develop a model where the properties of open- and closed-shell Tyr can be investigated, a stable protein scaffold is needed. As shown in Chapter 2, selecting the right protein system is sometimes not straightforward. For the work described in this Chapter, the well-characterized, blue copper protein azurin from *P. aeruginosa* was chosen as the model system. Azurin is a small blue copper protein that is localized in the periplasmic space. It participates in bacterial denitrification by facilitating single-electron transfer reactions between Cu(I) and Cu(II).[11] Taking advantage of this, the copper ion is useful as either a donor or acceptor in ET studies. A mutant azurin with Tyr at position 48 (i.e., Trp48Tyr) and where all other Tyr has been changed to Phe (i.e., Tyr72Phe, Tyr107Phe) is known (Figure 4.1). Using the amber stop codon technology described above, a series of artificial azurins were created where Tyr48 is replaced with different fluorotyrosine residues.

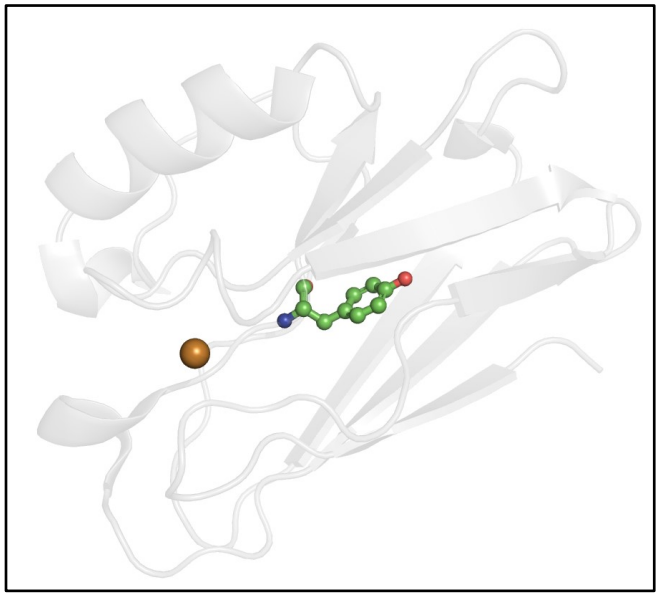

Figure 4.1. Image of Tyr48 azurin (PDB ID 3U25) showing the position of Tyr48 buried in the core of azurin. For reference, the Cu ion is shown as a copper-coloured sphere.

The electron paramagnetic resonance (EPR) spectroscopy of the Tyr48 radical has been investigated.[110] The properties are unique when compared to other tyrosine

radicals, which can be attributed to the unique hydrophobic site of position 48 in azurin.[111] Related studies on the Trp48 radical, further support that the core of azurin has distinct properties that can be probed spectroscopically.[112,113] In particular, magnetic resonance is useful in assessing the hydrogen bonding properties of the radical sites.[113] Raman and fluorescence measurements also inform on the nature of the Trp48 environment.[114] There are fewer nuclear magnetic resonance studies that target these sites specifically, though there are NMR studies of azurin that are available.[115] In sum, position 48 in azurin is an excellent site for probing the properties of embedded amino acids and their radicals. The incorporation of F_n-Tyr described in this Chapter is a step toward having a single platform with which to understand the physical properties of those residues in real protein environments.

4.2. Experimental

4.2.1. Materials

All reagents used were purchased from Sigma-Aldrich and used without purification unless otherwise noted. Miller LB broth, Terrific broth (TB), and L-arabinose were purchased from BioShop. 2-fluorophenol, 2,3-difluorophenol, 2,6-difluorophenol, 2,3,6-trifluorophenol, and 2,3,5,6-tetrafluorophenol were purchased from Tokyo Chemical Industry. Water used was from a Barnstead EASYpure system (18 MΩ cm^{-1}).

4.2.2. Site-directed mutagenesis

P. aeruginosa azurin mutant was prepared from a modified wild-type azurin gene (*azu*) with all Trp and Tyr amino acids mutated to Phe which is designated as all-Phe (Trp48Phe/Tyr72Phe/Tyr108Phe). The gene cloned in pET3a (Novagen) was then mutated to include an amber stop codon, Trp48TAG and a change from the terminal TAG stop codon to a TAA stop codon. The mutations were introduced by site-directed mutagenesis with the Q5 High-Fidelity PCR Kit (New England Biolabs). See Appendix C for the forward and reverse primers used (Integrated DNA Technologies). PCR cleanup was performed using the Qiagen QIAquick PCR Purification Kit and parent DNA digested with DpnI restriction enzyme (Thermo Scientific FastDigest). PCR reaction mixtures were transformed into 5-alpha chemically competent *E. coli* cells (New England Biolabs) and selection performed on ampicillin-supplemented LB agar incubated at 37°C, 16 hours.

Plasmid DNA from single colonies grown in liquid LB media was purified using the Qiagen QIAprep Spin Miniprep Kit. Sequences were verified using the Eurofins Genomics SimpleSeq Sanger sequencing service.

4.2.3. Synthesis of fluorotyrosines

E. coli strain SVS 370 containing pTZTPL plasmid was provided as a gift from JoAnne Stubbe from Massachusetts Institute of Technology. Expression of TPL for F_n-Tyr synthesis was based on literature-reported methods.[69,71,72] SVS 370 *E. coli* transformed with pTZTPL encoding *tpl* H343A was grown on LB agar supplemented with ampicillin. A single colony was grown in 30 mL LB with 100 µg/mL ampicillin (37°C, 180 rpm, 16 hours). From the starter culture, 16 mL was used to inoculate 8 L of broth containing 1% (w/v) casein enzymic hydrolysate, 0.5% (w/v) yeast extract, 0.5% (w/v) sodium chloride, and 100 µg/mL ampicillin. The broth was incubated (37°C, 150 rpm, 20 hours) and centrifuged (2000 *g*, 10 min, 4°C). The pellet was resuspended in 115 mL of 0.1 M potassium phosphate buffer (pH 7) containing 1 mM EDTA, 0.1 mM pyridoxal phosphate, and 5 mM β-mercaptoethanol. The cells were lysed by sonication for 3 minutes on ice (Branson Digital Sonifier 250 Cell Disruptor) and clarified lysate collected by centrifugation (25,000 *g*, 30 min, 4°C).

Synthesis of F_n-Tyr (n = 1–4) including 3-F-Tyr, 2,3-F_2-Tyr, 3,5-F_2-Tyr, 2,3,5-F_3-Tyr, and 2,3,5,6-F_4-Tyr were based on literature reported methods.[54,70] For the synthesis of all fluorotyrosines, 10 mM of the corresponding fluorophenol was added to 2 L of 30 mM ammonium acetate, 60 mM sodium pyruvate, and 5 mM β-mercaptoethanol adjusted to pH 8 with ammonium hydroxide. To each solution with the exception of 2,3,5,6-tetrafluorotyrosine, 40 µM pyridoxal phosphate and approximately 60 U of TPL were added where one unit is defined as 1 µmol of product per minute. The solution was stirred in the dark at 22°C for 3-4 days. For 2,3,5,6-F_4-Tyr, 40 µM pyridoxal phosphate and approximately 600 U of TPL were added. The reaction was continued for 3-4 weeks in the dark at 22°C with an additional 40 U of TPL and 1 mM of 2,3,5,6-tetrafluorophenol added each week. To purify all fluorotyrosines, HCl was added to all solutions to pH 2.7 to precipitate TPL. The precipitate was removed by filtering through a Celite pad. Unreacted fluorophenol was removed by liquid-liquid extraction using 500 mL ethyl acetate. The aqueous layer was loaded on a Dowex 50W-X8 hydrogen form cation exchange column (20-50 mesh) equilibrated with water. The column was washed with 8 column volumes of

water and eluted with 10% (v/v) ammonium hydroxide. Fractions containing α-amino acids as determined by a positive ninhydrin test were combined and solvent removed *in vacuo*. The F_n-Tyr analogues were characterized using ^{1}H and ^{19}F NMR recorded with a Bruker Ultrashield Plus 500 MHz (see Chapter 2).

4.2.4. Protein expression and purification

The pEVOL-*F_nYRS-E3* plasmid was provided as a gift from JoAnne Stubbe from Massachusetts Institute of Technology.[53] Protein expression optimizations included different concentrations of F_n-Tyr, the absence and presence of IPTG for induction, and post-induction incubation temperature. The expression levels of whole cell lysate were then analyzed using SDS-PAGE and expression levels determined with densitometry in ImageJ.[74]

Mutant *azu* Trp48TAG/Tyr72Phe/Tyr108Phe with TAA terminal stop codon and pEVOL-*F_nYRS-E3* were sequentially transformed into chemically competent BL21(DE3) *E. coli* cells (New England Biolabs) and selected for on ampicillin and chloramphenicol-supplemented LB agar (37°C, 16 hours). A single colony was inoculated into a starter culture of 25 mL LB supplemented with 100 µg/mL ampicillin and 25 µg/mL chloramphenicol then incubated (37°C, 180 rpm, 16 hours). From the starter culture, 3 mL was used to inoculate 1 L LB supplemented with 0.4% (v/v) glycerol, 100 µg/mL ampicillin, 25 µg/mL chloramphenicol, and 1 mM of the appropriate F_n-Tyr solubilized with ammonium hydroxide. The large culture was incubated (37°C, 180 rpm) and induced at an OD_{600} of 0.65 where 1 mM IPTG and 0.02% L-arabinose were added. The culture was incubated further (30°C, 180 rpm, 17.5 hours) and the pellet collected by centrifugation (4500*g*, 15 min, 4°C).

Azurin all-Phe (Trp48Phe/Tyr72Phe/Tyr108Phe) as a control was expressed similarly with transformation into chemically competent BL21(DE3) *E. coli* cells and selected for with ampicillin-supplemented LB agar (37°C, 16 hours). A single colony was inoculated into a 35 mL starter culture of LB supplemented with 100 µg/mL ampicillin and incubated (37°C, 180 rpm, 16 hours). From the starter culture, 3 mL was used to inoculate 1 L LB supplemented with 0.4% (v/v) glycerol and 100 µg/mL ampicillin. After incubation (37°C, 180 rpm) to an OD_{600} of 0.65, 1 mM IPTG was added. The culture was then

incubated at reduced temperature (30°C, 180 rpm, 17.5 hours) and the pellet collected by centrifugation (4500*g*, 15 min, 4°C).

An osmotic shock was performed where the pellet was resuspended in 10 mL of 50 mM Tris (pH 8.1), 1 mM EDTA, and 20% sucrose and incubated at 4°C for 20 minutes. The resuspension was centrifuged (6000 *g*, 20 min, 4°C) and the pellet resuspended in 20 mL of 500 µM $MgCl_2$. The resuspension was incubated at 4°C (20 min) and centrifuged (17,500 *g*, 20 min, 4°C). The supernatant was collected and the azurin metallated with 1.25 mL of 100 mM $CuSO_4$ and 750 µL of 500 mM sodium acetate (pH 4.5) added dropwise while stirring. The light blue solution was incubated (37°C, 180 rpm, 21.5 hours) and centrifuged (17,500 *g*, 20 min, 4°C) to remove the precipitate. The solution was purified with a CM Sepharose cation exchange column (Cytiva) equilibrated with 30 mM sodium acetate (pH 4). The column was washed with 3 column volumes of 30 mM sodium acetate (pH 4) and azurin eluted with 100 mM sodium acetate (pH 4.5). Fractions containing azurin were combined, concentrated by ultrafiltration (Amicon, 10 kDa), and exchanged into 30 mM sodium acetate buffer (pH 4) by gel filtration with a PD-10 column (Cytiva). UV–Vis spectra were collected of azurin in 30 mM sodium acetate (pH 4) with a Cary 100 Bio UV–Visible spectrophotometer.

4.2.5. Mass spectrometry

MALDI-TOF was used to verify the identities of mutant F_n-Tyr-azurin. Data collection was performed with a Bruker microFLEX MALDI-TOF instrument. Azurin mutants were prepared for MS analysis by exchanging them into water. Sinapinic acid was used as the MALDI matrix where the azurin was mixed 1:1 (v/v) with a solution containing 30:70 (v/v) acetonitrile : 0.1% TFA in water saturated with sinapinic acid. The mixture was then deposited onto a Bruker MALDI Biotarget 48 target plate over a dried drop of saturated sinapinic acid in ethanol. Theoretical monoisotopic masses of the protein were calculated based on the DNA sequence using the ExPASy Compute pI/Mw tool.[75–77]

4.3. Results and discussion

The azurin mutation of interest, namely Trp48TAG was produced using site-directed mutagenesis and verified with sequencing. Initial expression tests of azurin F_n-

Tyr48 containing the additional substitutions Tyr72Phe and Tyr108Phe did not appear to produce any desired protein following osmotic shock and the purification procedure. In contrast, expression and isolation of the control azurin all-Phe mutant (Trp48Phe/Tyr72Phe/Tyr108Phe) was typical. Given that expression required not only the plasmid carrying the azurin mutant gene but pEVOL-*F_nYRS-E3* which encodes for the tRNA and aaRS involved in F_n-Tyr insertion, the results were not all that surprising. Small-scale expression tests were carried out to optimize the production of azurin and visualized on an SDS-PAGE gel (Figure 4.2). Two different temperatures at 30 and 37°C were examined with the lack or presence of IPTG at 0.5 and 1 mM. While there did not appear to be significant overexpression of the protein, there were measurable differences in the intensity of the bands. Conditions of 30°C and addition of 1 mM IPTG provided the most intense band.

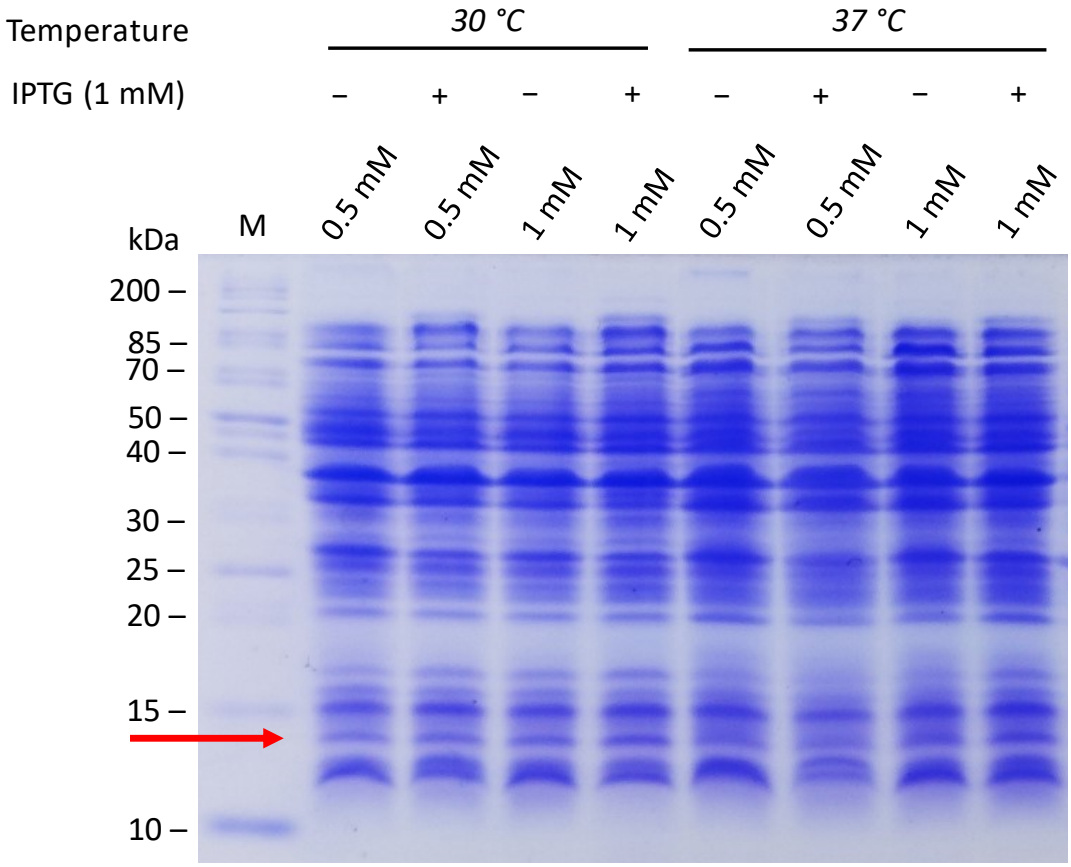

Figure 4.2. Whole-cell lysate SDS-PAGE gel of test expressions for 3-F-Tyr TAG48 incorporated azurin. The effect of IPTG concentration for induction of pET3a plasmid containing *azu* was examined along with incubation temperature post-induction. The red arrow indicates the band representing azurin (~13.9 kDa).

With the optimized parameters, 1 L preparative scale expressions of azurin were performed. Following osmotic shock, the periplasmic proteins were collected and presence of full-length azurin was assessed on an SDS-PAGE gel (Figure 4.3). Of the five F_n-Tyr examined, all of them had a band present with a mass of approximately 13.9 kDa, in line with the expected mass of the different variants and similar to the Trp48Phe/Tyr72Phe/Tyr108Phe control (Table 4.1). Further, the intensity of background proteins was also lower comparatively. Of these, 3-F-Tyr and 3,5-F_2-Tyr variants were purified and a light blue solution was obtained for each suggesting the existence of copper-metallated azurin. SDS-PAGE reconfirmed the presence of a band at 13.9 kDa of higher intensity (Figure 4.4). MALDI-TOF further verified that the two 3-F-Tyr and 3,5-F_2-Tyr variants had masses of 13900 and 13914 Da respectively, which were close to the expected monoisotopic masses (Figure C.1 and C.2).

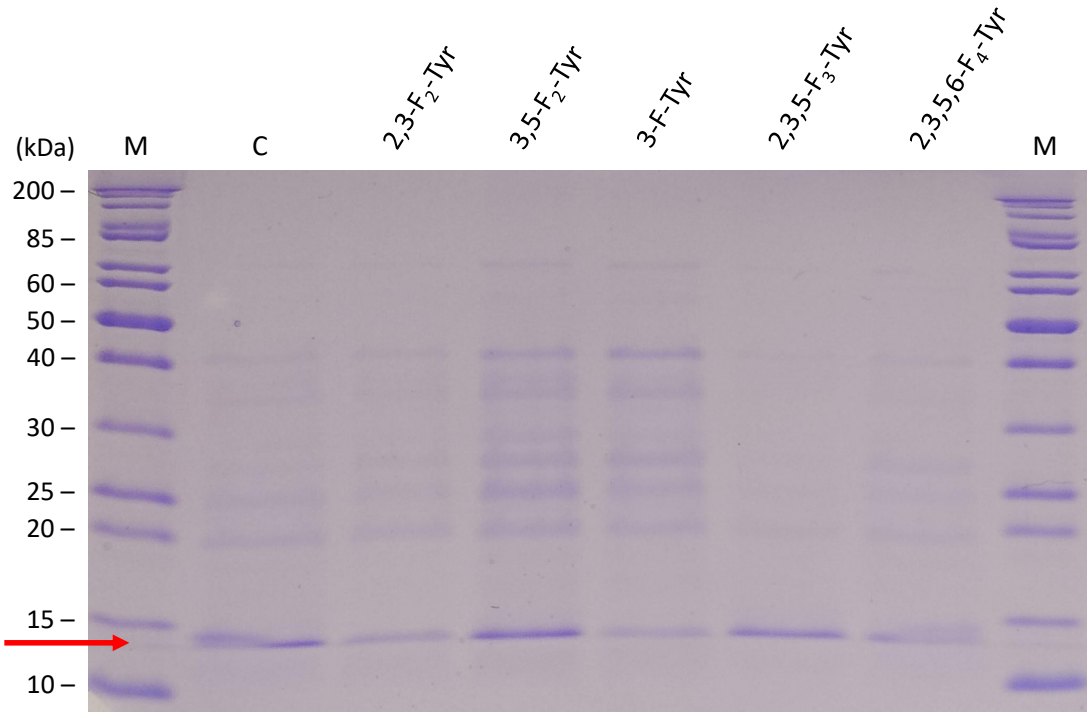

Figure 4.3. SDS-PAGE gel of azurin Trp48-F_n-Tyr/Tyr72Phe/Tyr108Phe expressions incorporated with F_n-Tyr following osmotic shock. The control (C) represents concurrent expression of known azurin all-Phe (Trp48Phe/Tyr72Phe/Tyr108Phe) following osmotic shock. The red arrow indicates the band representing azurin (~13.9 kDa).

Table 4.1. Calculated and MALDI-TOF collected masses of azurin variants

Variant	Expected Average Mass (Da)	Expected Monoisotopic Mass (Da)	Obtained Monoisotopic Mass (Da)
Trp48TAG Truncated[a]	5128.72	5125.39	—
Trp48-(3-F-Tyr)	13908.76	13899.75	13899.64
Trp48-(2,3-F_2-Tyr)	13926.75	13917.75	—
Trp48-(3,5-F_2-Tyr)	13926.75	13917.75	13914.39
Trp48-(2,3,5-F_3-Tyr)	13944.74	13935.74	—
Trp48-(2,3,5,6-F_4-Tyr)	13962.73	13953.73	—

[a]Truncated protein masses calculated based on the azurin Trp48TAG/Tyr72Phe/Tyr108Phe sequence up to and including Asn47.

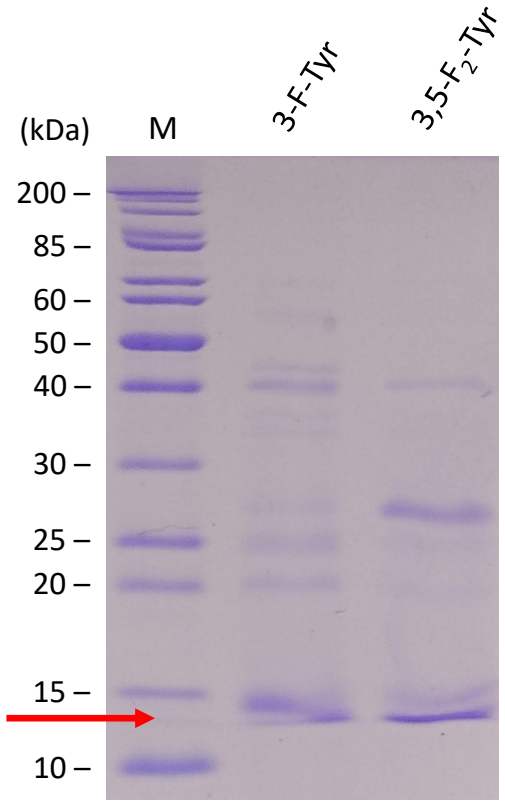

Figure 4.4. SDS-PAGE gel of purified azurin Trp48TAG/Tyr72Phe/Tyr108Phe incorporated with F_n-Tyr. The red arrow indicates the band representing azurin (~13.9 kDa).

Optical spectra were collected and yields were determined to be 0.2 mg/L and 6.1 mg/L for 3-F-Tyr and 3,5-F_2-Tyr respectively, where L is the volume of expression media (Figure 4.5). Both spectra show the presence of a band at 417 nm which is likely attributed to the coelution of cytochrome *c* during purification as expressed by the *E. coli* itself (see Chapter 3). Even low concentrations of cyt *c* contamination may be seen due to its relatively large Soret band's extinction coefficient. Further optimizing the expression of

azurin to increase the ratio of recombinant to basally expressed protein may help to decrease the relative amount of cyt *c* present during the purification process. Further, both spectra had similar energies and intensities of the ligand-to-metal charge transfer transition at 625 and 627 nm for both variants.[116] WT azurin also has a reported absorption maximum at 625 nm suggesting the copper environment is preserved for 3-F-Tyr and 3,5-F_2-Tyr.[117] Given the proximity of the Trp48 amino acid in WT to the copper, it can be conceived that distortions to the surrounding protein will cause large changes in the absorption maximum.

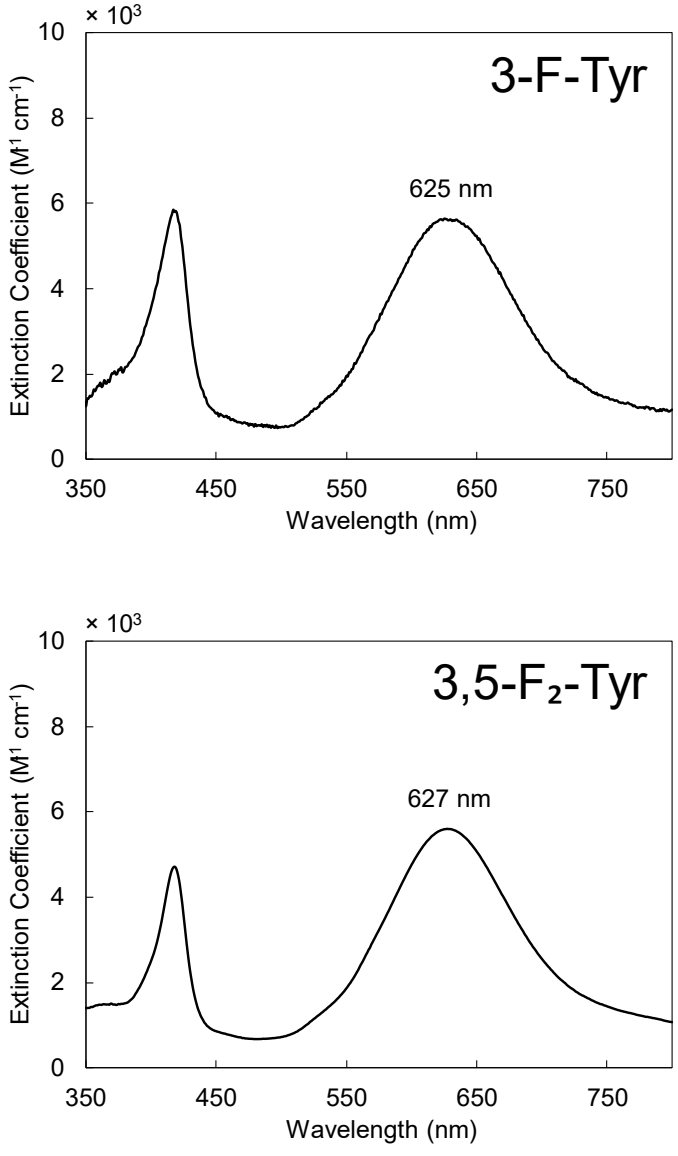

Figure 4.5. Optical spectra of 3-F-Tyr48 and 3,5-F_2-Tyr48 azurin variants in 60 mM sodium acetate at pH 4.0.

4.4. Conclusion

Based on our preliminary experimentation as a proof of concept, we have successfully expressed azurin with Trp48-(3-F-Tyr) and Trp48-(3,5-F_2-Tyr) incorporated as observed with SDS-PAGE and MALDI-TOF experiments. Optical spectroscopy was also used as a starting point to determine any structural differences at the copper site due to F_n-Tyr substitution. With the promising results of the initial characterization studies, future experiments will include further structural characterization based on electrochemistry and circular dichroism spectroscopy to determine the effect insertion of fluorotyrosines has on the overall structure. The other fluorotyrosines including 2,3-F_2-Tyr, 2,3,5-F_3-Tyr, and 2,3,5,6-F_4-Tyr will also be expressed and explored in more detail prior to electron paramagnetic resonance studies.

Chapter 5.

Closing remarks and future directions

Intraprotein electron transfer is essential for enabling the shuttling of electrons in biological systems and thus has attracted a large body of research from scientists. We further build on this foundation of research with the work reported in this thesis with an emphasis on modifying interactions in ET pathways. We first describe a method for incorporating fluorotyrosine unnatural amino acids into cytochrome *c* in order to modify an ET pathway by small increments (Chapter 2). Next, a series of substitutions were made to cyt *c*, namely Asp60Ala, Trp59Phe, and Met64Leu to modify hydrogen bonding in a second pathway (Chapter 3). Finally, we conducted preliminary experiments to illustrate proof of concept for introducing fluorotyrosines into azurin at position 48 in order to develop a system for understanding the properties of open- and closed-shell Tyr unnatural amino acids in a protein system (Chapter 4).

Chapter 2 described the process for substituting Tyr67 with different fluorotyrosines to examine an ET pathway beginning at Cys66. Through various optimization schemes, expression yields appeared to have increased noticeably based on SDS-PAGE results. However, while it appeared as though full-length cyt *c* with various fluorotyrosines were incorporated with no truncated protein detected, the expression levels were too poor to allow for downstream characterization experiments. In the process, a new plasmid was created combining both the cyt *c* gene and *ccmABCDEFGH* allowing for simpler expression protocols in the future and increased plasmid compatibilities. Given the structural importance of Tyr67 in maintaining the hydrogen bond network, it may be useful to target tyrosine residues that do not play significant roles in structure and function in the future. We are actively exploring the usage of the amber suppression system to incorporate fluorotyrosines in other protein models including azurin as discussed in Chapter 4.

Chapter 3 evaluated the significance of the cyt *c* hydrogen bond network in the context of ET. The Cys62 pathway was selected due to the presence of two hydrogen bonds. Separate substitutions were made to remove the hydrogen bonds separately with Asp60Ala and Trp59Phe which were expected to slow ET. Surprisingly, upon designing

the Ru-modified variants of these proteins, flash-quench experiments demonstrated that removal of these interactions did not change ET rates. I proceeded to generate a third mutation set with Met64Leu to examine an alternative ET pathway. The mutation increases the through-space jump between amino acid 64 and the heme. Flash-quench experiments showed that the rate of ET decreased by a factor of 2 indicating a preference for this pathway over the previously described one. Computational studies are currently being performed to study the electronic effects of these mutants. Given that the effect of hydrogen bonds was not able to be studied for ET, future work can explore hydrogen bond networks in other protein pathways. Further, it may be of interest to explore the Trp59Tyr mutant for any potential peroxidase activity given the likelihood of weakened or lost Met80-iron ligation.

Chapter 4 revisited the incorporation of fluorotyrosines in a different protein model, azurin. The fluorotyrosines were incorporated at position 48 to create mutants that are closely related to each other to study open- and closed-shell Tyr48. I have expressed 3-F-Tyr and 3,5-F_2-Tyr variants of azurin thus far and am in the process of performing preliminary characterization for 2,3,5-F_3-Tyr as well. With the azurin, I intend to further characterize the protein to understand the redox properties of the Tyr48 in comparison with F_n-Tyr48. I aim to use techniques including spectroscopy, electrochemistry, and magnetic resonance studies to examine this.

Over the course of examining the incorporation of fluorotyrosines in proteins, it appears as though the simpler the protein is to express, the better the outcome will be. For cyt *c*, a host of cytochrome *c* maturation proteins are required (*ccmABCDEFGH*) for expression which can pose a large burden on the *E. coli* on top of the need to produce machinery to incorporate the fluorotyrosines themselves. Expression levels of cyt *c, to begin with,* were already low in contrast to azurin. Further, a downside with azurin is that the protein is secreted to the periplasmic space requiring an osmotic shock to be performed for isolation. Thus, a fine balance is required between extracting as much protein from this space as possible without rupturing the cells themselves and releasing difficult to separate cytoplasmic proteins. It would seem that protein models of interest should feature already high expression levels for WT and simple expression and purification systems to encourage the best outcomes.

References

(1) Nelson, N.; Ben-Shem, A. The Complex Architecture of Oxygenic Photosynthesis. *Nat. Rev. Mol. Cell Biol.* **2004**, *5*, 971–982. https://doi.org/10.1038/nrm1525.

(2) Rutherford, A. W.; Faller, P. Photosystem II: Evolutionary Perspectives. *Philos. Trans. R. Soc. Lond., B, Biol. Sci.* **2003**, *358* (1429), 245–253. https://doi.org/10.1098/rstb.2002.1186.

(3) Sazanov, L. A. A Giant Molecular Proton Pump: Structure and Mechanism of Respiratory Complex I. *Nat. Rev. Mol. Cell Biol.* **2015**, *16*, 375–388. https://doi.org/10.1038/nrm3997.

(4) Yoshikawa, S.; Shimada, A. Reaction Mechanism of Cytochrome *c* Oxidase. *Chem. Rev.* **2015**, *115* (4), 1936–1989. https://doi.org/10.1021/cr500266a.

(5) Liguori, I.; Russo, G.; Curcio, F.; Bulli, G.; Aran, L.; Della-Morte, D.; Gargiulo, G.; Testa, G.; Cacciatore, F.; Bonaduce, D.; Abete, P. Oxidative Stress, Aging, and Diseases. *Clin. Interv. Aging* **2018**, *13*, 757–772. https://doi.org/10.2147/CIA.S158513.

(6) Liu, J.; Chakraborty, S.; Hosseinzadeh, P.; Yu, Y.; Tian, S.; Petrik, I.; Bhagi, A.; Lu, Y. Metalloproteins Containing Cytochrome, Iron–Sulfur, or Copper Redox Centers. *Chem. Rev.* **2014**, *114* (8), 4366–4469. https://doi.org/10.1021/cr400479b.

(7) Scott, R. A.; Mauk, A. G. *Cytochrome C: A Multidisciplinary Approach*; University Science Books, 1996.

(8) Dawson, J. W.; Gray, H. B.; Holwerda, R. A.; Westhead, E. W. Kinetics of the Reduction of Metalloproteins by Chromous Ion. *Proc. Natl. Acad. Sci. USA* **1972**, *69* (1), 30–33. https://doi.org/10.1073/pnas.69.1.30.

(9) McArdle, J. V.; Gray, H. B.; Creutz, C.; Sutin, N. Kinetic Studies of the Oxidation of Ferrocytochrome *c* from Horse Heart and *Candida Krusei* by Tris(1,10-Phenanthroline)Cobalt(III). *J. Am. Chem. Soc.* **1974**, *96* (18), 5737–5741. https://doi.org/10.1021/ja00825a009.

(10) Wherland, S.; Pecht, I. Protein-Protein Electron Transfer. A Marcus Theory Analysis of Reactions between *c* Type Cytochromes and Blue Copper Proteins. *Biochemistry* **1978**, *17* (13), 2585–2591. https://doi.org/10.1021/bi00606a020.

(11) Parr, S. R.; Barber, D.; Greenwood, C. A Purification Procedure for the Soluble Cytochrome Oxidase and Some Other Respiratory Proteins from *Pseudomonas Aeruginosa*. *Biochem. J.* **1976**, *157* (2), 423–430. https://doi.org/10.1042/bj1570423.

(12) Marcus, R. A.; Sutin, N. Electron Transfers in Chemistry and Biology. *Biochim. Biophys. Acta Bioenerg.* **1985**, *811* (3), 265–322. https://doi.org/10.1016/0304-4173(85)90014-X.

(13) Barbara, P. F.; Meyer, T. J.; Ratner, M. A. Contemporary Issues in Electron Transfer Research. *J. Phys. Chem.* **1996**, *100* (31), 13148–13168. https://doi.org/10.1021/jp9605663.

(14) Hopfield, J. J. Electron Transfer Between Biological Molecules by Thermally Activated Tunneling. *Proc. Natl. Acad. Sci. U.S.A.* **1974**, *71* (9), 3640–3644. https://doi.org/10.1073/pnas.71.9.3640.

(15) Marcus, R. A. On the Theory of Electron-Transfer Reactions. VI. Unified Treatment for Homogeneous and Electrode Reactions. *J. Chem. Phys.* **1965**, *43* (2), 679–701. https://doi.org/10.1063/1.1696792.

(16) Gray, H. B.; Winkler, J. R. Long-Range Electron Transfer. *Proc. Natl. Acad. Sci. USA* **2005**, *102* (10), 3534–3539. https://doi.org/10.1073/pnas.0408029102.

(17) Mauk, A. G.; Scott, R. A.; Gray, H. B. Distances of Electron Transfer to and from Metalloprotein Redox Sites in Reactions with Inorganic Complexes. *J. Am. Chem. Soc.* **1980**, *102* (13), 4360–4363. https://doi.org/10.1021/ja00533a012.

(18) Yocom, K. M.; Shelton, J. B.; Shelton, J. R.; Schroeder, W. A.; Worosila, G.; Isied, S. S.; Bordignon, E.; Gray, H. B. Preparation and Characterization of a Pentaammineruthenium(III) Derivative of Horse Heart Ferricytochrome *c*. *Proc. Natl. Acad. Sci. U. S. A.* **1982**, *79* (22), 7052–7055. https://doi.org/10.1073/pnas.79.22.7052.

(19) Winkler, J. R.; Nocera, D. G.; Yocom, K. M.; Bordignon, E.; Gray, H. B. Electron-Transfer Kinetics of Pentaammineruthenium(III)(Histidine-33)-Ferricytochrome *c*. Measurement of the Rate of Intramolecular Electron Transfer between Redox Centers Separated by 15 Å in a Protein. *J. Am. Chem. Soc.* **1982**, *104* (21), 5798–5800. https://doi.org/10.1021/ja00385a047.

(20) Elias, Horst.; Chou, M. H.; Winkler, J. R. Electron-Transfer Kinetics of Zinc-Substituted Cytochrome *c* and Its Ru(NH3)5(Histidine-33) Derivative. *J. Am. Chem. Soc.* **1988**, *110* (2), 429–434. https://doi.org/10.1021/ja00210a019.

(21) Meade, T. J.; Gray, H. B.; Winkler, J. R. Driving-Force Effects on the Rate of Long-Range Electron Transfer in Ruthenium-Modified Cytochrome *c*. *J. Am. Chem. Soc.* **1989**, *111* (12), 4353–4356. https://doi.org/10.1021/ja00194a030.

(22) Chang, I. J.; Gray, H. B.; Winkler, J. R. High-Driving-Force Electron Transfer in Metalloproteins: Intramolecular Oxidation of Ferrocytochrome c by Ru(2,2'-Bpy)$_2$(Im)(His-33)$^{3+}$. *J. Am. Chem. Soc.* **1991**, *113* (18), 7056–7057. https://doi.org/10.1021/ja00018a064.

(23) Winkler, J. R.; Di Bilio, A. J.; Farrow, N. A.; Richards, J. H.; Gray, H. B. Electron Tunneling in Biological Molecules. *Pure Appl. Chem.* **1999**, *71* (9), 1753–1764. https://doi.org/10.1351/pac199971091753.

(24) Gray, H. B.; Winkler, J. R. Electron Tunneling through Proteins. *Quart. Rev. Biophys.* **2003**, *36* (3), 341–372. https://doi.org/10.1017/S0033583503003913.

(25) Wuttke, D. S.; Bjerrum, M. J.; Chang, I.-J.; Winkler, J. R.; Gray, H. B. Electron Tunneling in Ruthenium-Modified Cytochrome *c*. *Biochim. Biophys. Acta Bioenerg.* **1992**, *1101* (2), 168–170. https://doi.org/10.1016/0005-2728(92)90204-F.

(26) Gray, H. B.; Winkler, J. R. Electron Flow through Proteins. *Chem. Phys. Lett.* **2009**, *483* (1–3), 1–9. https://doi.org/10.1016/j.cplett.2009.10.051.

(27) Halpern, J.; Orgel, L. E. The Theory of Electron Transfer between Metal Ions in Bridged Systems. *Discuss. Faraday Soc.* **1960**, *29*, 32–41. https://doi.org/10.1039/df9602900032.

(28) McConnell, H. M. Intramolecular Charge Transfer in Aromatic Free Radicals. *J. Chem. Phys.* **1961**, *35* (2), 508–515. https://doi.org/10.1063/1.1731961.

(29) Beratan, D. N.; Onuchic, J. N.; Hopfield, J. J. Electron Tunneling through Covalent and Noncovalent Pathways in Proteins. *J. Chem. Phys.* **1987**, *86* (8), 4488–4498. https://doi.org/10.1063/1.452723.

(30) Onuchic, J. N.; Beratan, D. N. A Predictive Theoretical Model for Electron Tunneling Pathways in Proteins. *J. Chem. Phys.* **1990**, *92* (1), 722–733. https://doi.org/10.1063/1.458426.

(31) Onuchic, J. N.; Beratan, D. N.; Winkler, J. R.; Gray, H. B. Pathway Analysis of Protein Electron-Transfer Reactions. *Annu. Rev. Biophys. Biomol. Struct.* **1992**, *21*, 349–377.

(32) Beratan, D. N.; Onuchic, J. N.; Winkler, J. R.; Gray, H. B. Electron-Tunneling Pathways in Proteins. *Science* **1992**, *258* (5089), 1740–1741. https://doi.org/10.1126/science.1334572.

(33) Prytkova, T. R.; Kurnikov, I. V.; Beratan, D. N. Coupling Coherence Distinguishes Structure Sensitivity in Protein Electron Transfer. *Science* **2007**, *315* (5812), 622–625. https://doi.org/10.1126/science.1134862.

(34) Stokes, G. G. On the Reduction and Oxidation of the Colouring Matter of the Blood. *Proc. R. Soc. Lond.* **1864**, *13*, 355–364. https://doi.org/10.1098/rspl.1863.0080.

(35) Hill, R. The Chemical Nature of Hæmochromogen and Its Carbon Monoxide Compound. *Proc. R. Soc. Lond. B.* **1926**, *100* (705), 419–430. https://doi.org/10.1098/rspb.1926.0064.

(36) Hill, R. Reduced Hæmatin and Hæmochromogen. *Proc. R. Soc. Lond. B.* **1929**, *105* (735), 112–130. https://doi.org/10.1098/rspb.1929.0032.

(37) Schejter, A.; Aviram, I. The Reaction of Cytochrome *c* with Imidazole. *Biochemistry* **1969**, *8* (1), 149–153. https://doi.org/10.1021/bi00829a021.

(38) George, P.; Schejter, A. The Reactivity of Ferrocytochrome *c* with Iron-Binding Ligands. *J. Biol. Chem.* **1964**, *239* (5), 1504–1508. https://doi.org/10.1016/S0021-9258(18)91343-8.

(39) George, P.; Glauser, S. C.; Schejter, A. The Reactivity of Ferricytochrome *c* with Ionic Ligands. *J. Biol. Chem.* **1967**, *242* (8), 1690–1695. https://doi.org/10.1016/S0021-9258(18)96056-4.

(40) Schejter, A.; Plotkin, B.; Vig, I. The Reactivity of Cytochrome *c* with Soft Ligands. *FEBS Letters* **1991**, *280* (2), 199–201. https://doi.org/10.1016/0014-5793(91)80292-B.

(41) Berry, E. A.; Trumpower, B. L. Simultaneous Determination of Hemes *a*, *b*, and *c* from Pyridine Hemochrome Spectra. *Anal. Biochem.* **1987**, *161* (1), 1–15. https://doi.org/10.1016/0003-2697(87)90643-9.

(42) Holzwarth, G.; Doty, P. The Ultraviolet Circular Dichroism of Polypeptides. *J. Am. Chem. Soc.* **1965**, *87* (2), 218–228. https://doi.org/10.1021/ja01080a015.

(43) Greenfield, N. J.; Fasman, G. D. Computed Circular Dichroism Spectra for the Evaluation of Protein Conformation. *Biochemistry* **1969**, *8* (10), 4108–4116. https://doi.org/10.1021/bi00838a031.

(44) Venyaminov, S. Y.; Baikalov, I. A.; Shen, Z. M.; Wu, C. S. C.; Yang, J. T. Circular Dichroic Analysis of Denatured Proteins: Inclusion of Denatured Proteins in the Reference Set. *Anal. Biochem.* **1993**, *214* (1), 17–24. https://doi.org/10.1006/abio.1993.1450.

(45) Greenfield, N. J. Using Circular Dichroism Spectra to Estimate Protein Secondary Structure. *Nat. Protoc.* **2006**, *1* (6), 2876–2890. https://doi.org/10.1038/nprot.2006.202.

(46) Kelly, S. M.; Jess, T. J.; Price, N. C. How to Study Proteins by Circular Dichroism. *Biochim. Biophys. Acta Proteins Proteom.* **2005**, *1751* (2), 119–139. https://doi.org/10.1016/j.bbapap.2005.06.005.

(47) Böhm, G.; Muhr, R.; Jaenicke, R. Quantitative Analysis of Protein Far UV Circular Dichroism Spectra by Neural Networks. *Protein Eng. Des. Sel.* **1992**, *5* (3), 191–195. https://doi.org/10.1093/protein/5.3.191.

(48) Micsonai, A.; Wien, F.; Kernya, L.; Lee, Y.-H.; Goto, Y.; Réfrégiers, M.; Kardos, J. Accurate Secondary Structure Prediction and Fold Recognition for Circular Dichroism Spectroscopy. *Proc. Natl. Acad. Sci. U. S. A.* **2015**, *112* (24), E3095–E3103. https://doi.org/10.1073/pnas.1500851112.

(49) Micsonai, A.; Wien, F.; Bulyáki, É.; Kun, J.; Moussong, É.; Lee, Y.-H.; Goto, Y.; Réfrégiers, M.; Kardos, J. BeStSel: A Web Server for Accurate Protein Secondary Structure Prediction and Fold Recognition from the Circular Dichroism Spectra. *Nucleic Acids Res.* **2018**, *46* (W1), W315–W322. https://doi.org/10.1093/nar/gky497.

(50) Winter, G.; Fersht, A. R.; Wilkinson, A. J.; Zoller, M.; Smith, M. Redesigning Enzyme Structure by Site-Directed Mutagenesis: Tyrosyl TRNA Synthetase and ATP Binding. *Nature* **1982**, *299* (5885), 756–758. https://doi.org/10.1038/299756a0.

(51) Zheng, L.; Baumann, U.; Reymond, J.-L. An Efficient One-Step Site-Directed and Site-Saturation Mutagenesis Protocol. *Nucleic Acids Res.* **2004**, *32* (14), e115. https://doi.org/10.1093/nar/gnh110.

(52) Xie, J.; Schultz, P. G. An Expanding Genetic Code. *Methods* **2005**, *36* (3), 227–238. https://doi.org/10.1016/j.ymeth.2005.04.010.

(53) Minnihan, E. C.; Young, D. D.; Schultz, P. G.; Stubbe, J. Incorporation of Fluorotyrosines into Ribonucleotide Reductase Using an Evolved, Polyspecific Aminoacyl-TRNA Synthetase. *J. Am. Chem. Soc.* **2011**, *133* (40), 15942–15945. https://doi.org/10.1021/ja207719f.

(54) Seyedsayamdost, M. R.; Reece, S. Y.; Nocera, D. G.; Stubbe, J. Mono-, Di-, Tri-, and Tetra-Substituted Fluorotyrosines: New Probes for Enzymes That Use Tyrosyl Radicals in Catalysis. *J. Am. Chem. Soc.* **2006**, *128* (5), 1569–1579. https://doi.org/10.1021/ja055926r.

(55) Ravichandran, K. R.; Zong, A. B.; Taguchi, A. T.; Nocera, D. G.; Stubbe, J.; Tommos, C. Formal Reduction Potentials of Difluorotyrosine and Trifluorotyrosine Protein Residues: Defining the Thermodynamics of Multistep Radical Transfer. *J. Am. Chem. Soc.* **2017**, *139* (8), 2994–3004. https://doi.org/10.1021/jacs.6b11011.

(56) Loscha, K. V.; Herlt, A. J.; Qi, R.; Huber, T.; Ozawa, K.; Otting, G. Multiple-Site Labeling of Proteins with Unnatural Amino Acids. *Angew. Chem. Int. Ed.* **2012**, *51* (9), 2243–2246. https://doi.org/10.1002/anie.201108275.

(57) Nienberg, C.; Retterath, A.; Becher, K.-S.; Saenger, T.; Mootz, H.; Jose, J. Site-Specific Labeling of Protein Kinase CK2: Combining Surface Display and Click Chemistry for Drug Discovery Applications. *Pharmaceuticals* **2016**, *9* (3), 36. https://doi.org/10.3390/ph9030036.

(58) Heil, C. S.; Rittner, A.; Goebel, B.; Beyer, D.; Grininger, M. Site-Specific Labelling of Multidomain Proteins by Amber Codon Suppression. *Sci. Rep.* **2018**, *8* (1), 14864. https://doi.org/10.1038/s41598-018-33115-5.

(59) Lange, C.; Hunte, C. Crystal Structure of the Yeast Cytochrome Bc1 Complex with Its Bound Substrate Cytochrome c. *Proc. Natl. Acad. Sci. USA* **2002**, *99* (5), 2800–2805. https://doi.org/10.1073/pnas.052704699.

(60) Wenger, O. S. How Donor−Bridge−Acceptor Energetics Influence Electron Tunneling Dynamics and Their Distance Dependences. *Acc. Chem. Res.* **2011**, *44* (1), 25–35. https://doi.org/10.1021/ar100092v.

(61) Warren, J. J.; Ener, M. E.; Vlček, A.; Winkler, J. R.; Gray, H. B. Electron Hopping through Proteins. *Coord. Chem. Rev.* **2012**, *256* (21–22), 2478–2487. https://doi.org/10.1016/j.ccr.2012.03.032.

(62) Gu, J.; Yang, S.; Rajic, A. J.; Kurnikov, I. V.; Prytkova, T. R.; Pletneva, E. V. Control of Cytochrome *c* Redox Reactivity through Off-Pathway Modifications in the Protein Hydrogen-Bonding Network. *Chem. Commun.* **2014**, *50* (40), 5355–5357. https://doi.org/10.1039/c3cc47943a.

(63) Ying, T.; Wang, Z.-H.; Lin, Y.-W.; Xie, J.; Tan, X.; Huang, Z.-X. Tyrosine-67 in Cytochrome *c* Is a Possible Apoptotic Trigger Controlled by Hydrogen Bonds via a Conformational Transition. *Chem. Commun.* **2009**, No. 30, 4512. https://doi.org/10.1039/b904347k.

(64) Ow, Y.-L. P.; Green, D. R.; Hao, Z.; Mak, T. W. Cytochrome c: Functions beyond Respiration. *Nat. Rev. Mol. Cell Biol.* **2008**, *9* (7), 532–542. https://doi.org/10.1038/nrm2434.

(65) Belikova, N. A.; Vladimirov, Y. A.; Osipov, A. N.; Kapralov, A. A.; Tyurin, V. A.; Potapovich, M. V.; Basova, L. V.; Peterson, J.; Kurnikov, I. V.; Kagan, V. E. Peroxidase Activity and Structural Transitions of Cytochrome *c* Bound to Cardiolipin-Containing Membranes. *Biochemistry* **2006**, *45* (15), 4998–5009. https://doi.org/10.1021/bi0525573.

(66) Weber, D. S.; Warren, J. J. A Survey of Methionine-Aromatic Interaction Geometries in the Oxidoreductase Class of Enzymes: What Could Met-Aromatic Interactions Be Doing near Metal Sites? *J. Inorg. Biochem.* **2018**, *186*, 34–41. https://doi.org/10.1016/j.jinorgbio.2018.05.008.

(67) Weber, D. S.; Warren, J. J. The Interaction between Methionine and Two Aromatic Amino Acids Is an Abundant and Multifunctional Motif in Proteins. *Arch. Biochem. Biophys.* **2019**, *672*, 108053. https://doi.org/10.1016/j.abb.2019.07.018.

(68) Gómez-Tamayo, J. C.; Cordomí, A.; Olivella, M.; Mayol, E.; Fourmy, D.; Pardo, L. Analysis of the Interactions of Sulfur-Containing Amino Acids in Membrane Proteins: Interactions Involving Met and Cys in Membrane Proteins. *Protein Sci.* **2016**, *25* (8), 1517–1524. https://doi.org/10.1002/pro.2955.

(69) Chen, H.; Gollnick, P.; Phillips, R. S. Site-Directed Mutagenesis of His343-->Ala in *Citrobacter Freundii* Tyrosine Phenol-Lyase. Effects on the Kinetic Mechanism and Rate-Determining Step. *Eur. J. Biochem.* **1995**, *229* (2), 540–549. https://doi.org/10.1111/j.1432-1033.1995.0540k.x.

(70) Seyedsayamdost, M. R.; Yee, C. S.; Stubbe, J. Site-Specific Incorporation of Fluorotyrosines into the R2 Subunit of *E. Coli* Ribonucleotide Reductase by Expressed Protein Ligation. *Nat. Protoc.* **2007**, *2* (5), 1225–1235. https://doi.org/10.1038/nprot.2007.159.

(71) Phillips, R. S.; Ravichandran, K.; Tersch, R. L. V. Synthesis of L-Tyrosine from Phenol and S-(o-Nitrophenyl)-L-Cysteine Catalysed by Tyrosine Phenol-Lyase. *Enzyme Microb. Technol.* **1989**, *11* (2), 80–83. https://doi.org/10.1016/0141-0229(89)90064-1.

(72) Kim, K.; Cole, P. A. Kinetic Analysis of a Protein Tyrosine Kinase Reaction Transition State in the Forward and Reverse Directions. *J. Am. Chem. Soc.* **1998**, *120* (28), 6851–6858. https://doi.org/10.1021/ja9808393.

(73) Arslan, E.; Schulz, H.; Zufferey, R.; Künzler, P.; Thöny-Meyer, L. Overproduction of the *Bradyrhizobium Japonicum c*-Type Cytochrome Subunits of the Cbb3 Oxidase

in *Escherichia Coli*. *Biochem. Biophys. Res. Commun.* **1998**, *251* (3), 744–747. https://doi.org/10.1006/bbrc.1998.9549.

(74) Schneider, C. A.; Rasband, W. S.; Eliceiri, K. W. NIH Image to ImageJ: 25 Years of Image Analysis. *Nat. Methods* **2012**, *9* (7), 671–675. https://doi.org/10.1038/nmeth.2089.

(75) Bjellqvist, B.; Hughes, G. J.; Pasquali, C.; Paquet, N.; Ravier, F.; Sanchez, J.-C.; Frutiger, S.; Hochstrasser, D. The Focusing Positions of Polypeptides in Immobilized PH Gradients Can Be Predicted from Their Amino Acid Sequences. *Electrophoresis* **1993**, *14* (1), 1023–1031. https://doi.org/10.1002/elps.11501401163.

(76) Bjellqvist, B.; Basse, B.; Olsen, E.; Celis, J. E. Reference Points for Comparisons of Two-Dimensional Maps of Proteins from Different Human Cell Types Defined in a pH Scale Where Isoelectric Points Correlate with Polypeptide Compositions. *Electrophoresis* **1994**, *15* (1), 529–539. https://doi.org/10.1002/elps.1150150171.

(77) Gasteiger, E.; Hoogland, C.; Gattiker, A.; Duvaud, S.; Wilkins, M. R.; Appel, R. D.; Bairoch, A. Protein Identification and Analysis Tools on the ExPASy Server. In *The Proteomics Protocols Handbook*; Walker, J. M., Ed.; Humana Press: Totowa, NJ, 2005; pp 571–607. https://doi.org/10.1385/1-59259-890-0:571.

(78) Studier, F. W.; Moffatt, B. A. Use of Bacteriophage T7 RNA Polymerase to Direct Selective High-Level Expression of Cloned Genes. *J. Mol. Biol.* **1986**, *189* (1), 113–130. https://doi.org/10.1016/0022-2836(86)90385-2.

(79) Dubendorff, J. W.; Studier, F. W. Controlling Basal Expression in an Inducible T7 Expression System by Blocking the Target T7 Promoter with Lac Repressor. *J. Mol. Biol. 219* (1), 45–59. https://doi.org/10.1016/0022-2836(91)90856-2.

(80) Studier, F. W.; Rosenberg, A. H.; Dunn, J. J.; Dubendorff, J. W. Use of T7 RNA Polymerase to Direct Expression of Cloned Genes. In *Methods in Enzymology*; Elsevier, 1990; Vol. 185, pp 60–89. https://doi.org/10.1016/0076-6879(90)85008-C.

(81) Young, T. S.; Ahmad, I.; Yin, J. A.; Schultz, P. G. An Enhanced System for Unnatural Amino Acid Mutagenesis in *E. Coli*. *J. Mol. Biol.* **2010**, *395* (2), 361–374. https://doi.org/10.1016/j.jmb.2009.10.030.

(82) Baneyx, F.; Mujacic, M. Recombinant Protein Folding and Misfolding in *Escherichia Coli*. *Nat. Biotechnol.* **2004**, *22* (11), 1399–1408. https://doi.org/10.1038/nbt1029.

(83) Bowler, B. E.; Meade, T. J.; Mayo, S. L.; Richards, J. H.; Gray, H. B. Long-Range Electron Transfer in Structurally Engineered Pentaammineruthenium (Histidine-62)Cytochrome *c*. *J. Am. Chem. Soc.* **1989**, *111* (23), 8757–8759. https://doi.org/10.1021/ja00205a049.

(84) Beratan, D. N.; Onuchic, J. N.; Betts, J. N.; Bowler, B. E.; Gray, H. B. Electron Tunneling Pathways in Ruthenated Proteins. *J. Am. Chem. Soc.* **1990**, *112* (22), 7915–7921. https://doi.org/10.1021/ja00178a011.

(85) Dwaraknath, S.; Tran, N.-H.; Dao, T.; Colbert, A.; Mullen, S.; Nguyen, A.; Cortez, A.; Cheruzel, L. A Facile and Versatile Methodology for Cysteine Specific Labeling of Proteins with Octahedral Polypyridyl d^6 Metal Complexes. *J. Inorg. Biochem.* **2014**, *136*, 154–160. https://doi.org/10.1016/j.jinorgbio.2013.12.013.

(86) Wei, H.; Yin, J.; Wang, E. Bis(2,2′-Bipyridine)(5,6-Epoxy-5,6-Dihydro-[1,10] Phenanthroline)Ruthenium: Synthesis and Electrochemical and Electrochemiluminescence Characterization. *Anal. Chem.* **2008**, *80* (14), 5635–5639. https://doi.org/10.1021/ac8001462.

(87) Battistuzzi, G.; Borsari, M.; Cowan, J. A.; Ranieri, A.; Sola, M. Control of Cytochrome *c* Redox Potential: Axial Ligation and Protein Environment Effects. *J. Am. Chem. Soc.* **2002**, *124* (19), 5315–5324. https://doi.org/10.1021/ja017479v.

(88) Kaminsky, L. S.; Miller, V. J.; Davison, A. J. Thermodynamic Studies of the Opening of the Heme Crevice of Ferricytochrome *c*. *Biochemistry* **1973**, *12* (12), 2215–2221. https://doi.org/10.1021/bi00736a006.

(89) Rosell, F. I.; Ferrer, J. C.; Mauk, A. G. Proton-Linked Protein Conformational Switching: Definition of the Alkaline Conformational Transition of Yeast Iso-1-Ferricytochrome *c*. *J. Am. Chem. Soc.* **1998**, *120* (44), 11234–11245. https://doi.org/10.1021/ja971756+.

(90) Döpner, S.; Hildebrandt, P.; Rosell, F. I.; Mauk, A. G. Alkaline Conformational Transitions of Ferricytochrome *c* Studied by Resonance Raman Spectroscopy. *J. Am. Chem. Soc.* **1998**, *120* (44), 11246–11255. https://doi.org/10.1021/ja9717572.

(91) Monari, S.; Millo, D.; Ranieri, A.; Di Rocco, G.; van der Zwan, G.; Gooijer, C.; Peressini, S.; Tavagnacco, C.; Hildebrandt, P.; Borsari, M. The Impact of Urea-Induced Unfolding on the Redox Process of Immobilised Cytochrome *c*. *J. Biol. Inorg. Chem.* **2010**, *15* (8), 1233–1242. https://doi.org/10.1007/s00775-010-0681-7.

(92) Deng, Y.; Zhong, F.; Alden, S. L.; Hoke, K. R.; Pletneva, E. V. The K79G Mutation Reshapes the Heme Crevice and Alters Redox Properties of Cytochrome *c*. *Biochemistry* **2018**, *57* (40), 5827–5840. https://doi.org/10.1021/acs.biochem.8b00650.

(93) Stellwagen, E. Haem Exposure as the Determinate of Oxidation–Reduction Potential of Haem Proteins. *Nature* **1978**, *275* (5675), 73–74. https://doi.org/10.1038/275073a0.

(94) Tezcan, F. A.; Winkler, J. R.; Gray, H. B. Effects of Ligation and Folding on Reduction Potentials of Heme Proteins. *J. Am. Chem. Soc.* **1998**, *120* (51), 13383–13388. https://doi.org/10.1021/ja982536e.

(95) Mao, J.; Hauser, K.; Gunner, M. R. How Cytochromes with Different Folds Control Heme Redox Potentials. *Biochemistry* **2003**, *42* (33), 9829–9840. https://doi.org/10.1021/bi027288k.

(96) Casalini, S.; Battistuzzi, G.; Borsari, M.; Bortolotti, C. A.; Ranieri, A.; Sola, M. Electron Transfer and Electrocatalytic Properties of the Immobilized Methionine80Alanine Cytochrome *c* Variant. *J. Phys. Chem. B* **2008**, *112* (5), 1555–1563. https://doi.org/10.1021/jp0765953.

(97) Banci, L.; Bertini, I.; Bren, K. L.; Gray, H. B.; Sompornpisut, P.; Turano, P. Three-Dimensional Solution Structure of the Cyanide Adduct of a Variant of Saccharomyces Cerevisiae Iso-1-Cytochrome *c* Containing the Met80Ala Mutation. Identification of Ligand-Residue Interactions in the Distal Heme Cavity. *Biochemistry* **1995**, *34* (36), 11385–11398. https://doi.org/10.1021/bi00036a011.

(98) Mines, G. A.; Bjerrum, M. J.; Hill, M. G.; Casimiro, D. R.; Chang, I.-J.; Winkler, J. R.; Gray, H. B. Rates of Heme Oxidation and Reduction in Ru(His33)Cytochrome *c* at Very High Driving Forces. *J. Am. Chem. Soc.* **1996**, *118* (8), 1961–1965. https://doi.org/10.1021/ja9519243.

(99) Brunschwig, B. S.; Creutz, C.; Macartney, D. H.; Sham, T.-K.; Sutin, N. The Role of Inner-Sphere Configuration Changes in Electron-Exchange Reactions of Metal Complexes. *Faraday Discuss. Chem. Soc.* **1982**, *74*, 113–127. https://doi.org/10.1039/dc9827400113.

(100) Young, R. C.; Keene, F. R.; Meyer, T. J. Measurement of Rates of Electron Transfer between Tris(2,2'-Bipyridine)Ruthenium(3+) and Tris(1,10-Phenanthroline)Iron(2+) Ions and between Tris(1,10-Phenanthroline)Ruthenium(3+) and Tris(2,2'-Bipyridine)Ruthenium(2+) Ions by Differential Excitation Flash Photolysis. *J. Am. Chem. Soc.* **1977**, *99* (8), 2468–2473. https://doi.org/10.1021/ja00450a011.

(101) Stubbe, J.; van der Donk, W. A. Protein Radicals in Enzyme Catalysis. *Chem. Rev.* **1998**, *98* (2), 705–762. https://doi.org/10.1021/cr9400875.

(102) Teo, R. D.; Wang, R.; Smithwick, E. R.; Migliore, A.; Therien, M. J.; Beratan, D. N. Mapping Hole Hopping Escape Routes in Proteins. *Proc. Natl. Acad. Sci. U.S.A* **2019**, *116* (32), 15811–15816. https://doi.org/10.1073/pnas.1906394116.

(103) Gray, H. B.; Winkler, J. R. Living with Oxygen. *Acc. Chem. Res.* **2018**, *51* (8), 1850–1857. https://doi.org/10.1021/acs.accounts.8b00245.

(104) Garner, D. K.; Vaughan, M. D.; Hwang, H. J.; Savelieff, M. G.; Berry, S. M.; Honek, J. F.; Lu, Y. Reduction Potential Tuning of the Blue Copper Center in *Pseudomonas Aeruginosa* Azurin by the Axial Methionine as Probed by Unnatural Amino Acids. *J. Am. Chem. Soc.* **2006**, *128* (49), 15608–15617. https://doi.org/10.1021/ja062732i.

(105) Nödling, A. R.; Spear, L. A.; Williams, T. L.; Luk, L. Y. P.; Tsai, Y.-H. Using Genetically Incorporated Unnatural Amino Acids to Control Protein Functions in Mammalian Cells. *Essays Biochem.* **2019**, *63* (2), 237–266. https://doi.org/10.1042/EBC20180042.

(106) Minnihan, E. C.; Nocera, D. G.; Stubbe, J. Reversible, Long-Range Radical Transfer in *E. Coli* Class Ia Ribonucleotide Reductase. *Acc. Chem. Res.* **2013**, *46* (11), 2524–2535. https://doi.org/10.1021/ar4000407.

(107) Minnihan, E. C.; Seyedsayamdost, M. R.; Uhlin, U.; Stubbe, J. Kinetics of Radical Intermediate Formation and Deoxynucleotide Production in 3-Aminotyrosine-Substituted *Escherichia Coli* Ribonucleotide Reductases. *J. Am. Chem. Soc.* **2011**, *133* (24), 9430–9440. https://doi.org/10.1021/ja201640n.

(108) Ravichandran, K. R.; Minnihan, E. C.; Wei, Y.; Nocera, D. G.; Stubbe, J. Reverse Electron Transfer Completes the Catalytic Cycle in a 2,3,5-Trifluorotyrosine-Substituted Ribonucleotide Reductase. *J. Am. Chem. Soc.* **2015**, *137* (45), 14387–14395. https://doi.org/10.1021/jacs.5b09189.

(109) Ravichandran, K. R.; Taguchi, A. T.; Wei, Y.; Tommos, C.; Nocera, D. G.; Stubbe, J. A >200 MeV Uphill Thermodynamic Landscape for Radical Transport in *Escherichia Coli* Ribonucleotide Reductase Determined Using Fluorotyrosine-Substituted Enzymes. *J. Am. Chem. Soc.* **2016**, *138* (41), 13706–13716. https://doi.org/10.1021/jacs.6b08200.

(110) Wehbi, W. A. Amino Acid Radicals in Rhenium-Modified Copper Proteins. Dissertation (Ph.D.), California Institute of Technology, Pasadena CA, 2003.

(111) Gilardi, G.; Mei, G.; Rosato, N.; Canters, G. W.; Finazzi-Agro, A. Unique Environment of Trp48 in *Pseudomonas Aeruginosa* Azurin as Probed by Site-Directed Mutagenesis and Dynamic Fluorescence Spectroscopy. *Biochemistry* **1994**, *33* (6), 1425–1432. https://doi.org/10.1021/bi00172a020.

(112) Shafaat, H. S.; Leigh, B. S.; Tauber, M. J.; Kim, J. E. Spectroscopic Comparison of Photogenerated Tryptophan Radicals in Azurin: Effects of Local Environment and Structure. *J. Am. Chem. Soc.* **2010**, *132* (26), 9030–9039. https://doi.org/10.1021/ja101322g.

(113) Stoll, S.; Shafaat, H. S.; Krzystek, J.; Ozarowski, A.; Tauber, M. J.; Kim, J. E.; Britt, R. D. Hydrogen Bonding of Tryptophan Radicals Revealed by EPR at 700 GHz. *J. Am. Chem. Soc.* **2011**, *133* (45), 18098–18101. https://doi.org/10.1021/ja208462t.

(114) Rivera, J. J.; Liang, J. H.; Shimamura, G. R.; Shafaat, H. S.; Kim, J. E. Raman and Quantum Yield Studies of Trp48-d_5 in Azurin: Closed-Shell and Neutral Radical Species. *J. Phys. Chem. B* **2019**, *123* (30), 6430–6443. https://doi.org/10.1021/acs.jpcb.9b04655.

(115) Canters, G. W.; Hill, H. A. O.; Kitchen, N. A.; Adman, E. T. The Assignment of the ^{1}H Nuclear Magnetic Resonance Spectrum of Azurin. *Eur. J. Biochem.* **1984**, *138* (1), 141–152. https://doi.org/10.1111/j.1432-1033.1984.tb07893.x.

(116) Solomon, E. I.; Baldwin, M. J.; Lowery, M. D. Electronic Structures of Active Sites in Copper Proteins: Contributions to Reactivity. *Chem. Rev.* **1992**, *92* (4), 521–542. https://doi.org/10.1021/cr00012a003.

(117) Guzzi, R.; Sportelli, L.; Rosa, C. L.; Milardi, D.; Grasso, D.; Verbeet, M. P.; Canters, G. W. A Spectroscopic and Calorimetric Investigation on the Thermal Stability of the Cys3Ala/Cys26Ala Azurin Mutant. *Biophys. J.* **1999**, *77* (2), 1052–1063. https://doi.org/10.1016/S0006-3495(99)76955-9.

Appendix A.

Supporting information for Chapter 2

Table A.1 Primers for Glu66Cys series of *CYC1* mutants and *ccmABCDEFGH*.

Mutation		Sequence (5' → 3')
Glu66Cys	Forward	GTCATGCTACTTGACTAACCCAGCG
	Reverse	GTCAAGTAGCATGACATGTTATTTTCGTCCC
Glu66Cys/Tyr67TAG	Forward	GTCATGCTAGTTGACTAACCCAGCG
	Reverse	GTCAACTAGCATGACATGTTATTTTCGTCCC
Cytc_NdeI	Forward	ATTCTACATATGAAATACCTGCTGCCGACCGC
Cytc_XhoI	Reverse	TTGGAACTCGAGTTACTCAGAGGCTTTTTTCAAG
Ccm_NcoI	Forward	TAATGTCCATGGATGGGTATGCTTGAAGCCAGAG
Ccm_HindIII	Reverse	AATGTCAAGCTTTTATTTACTCTCCTGCGGCGAC

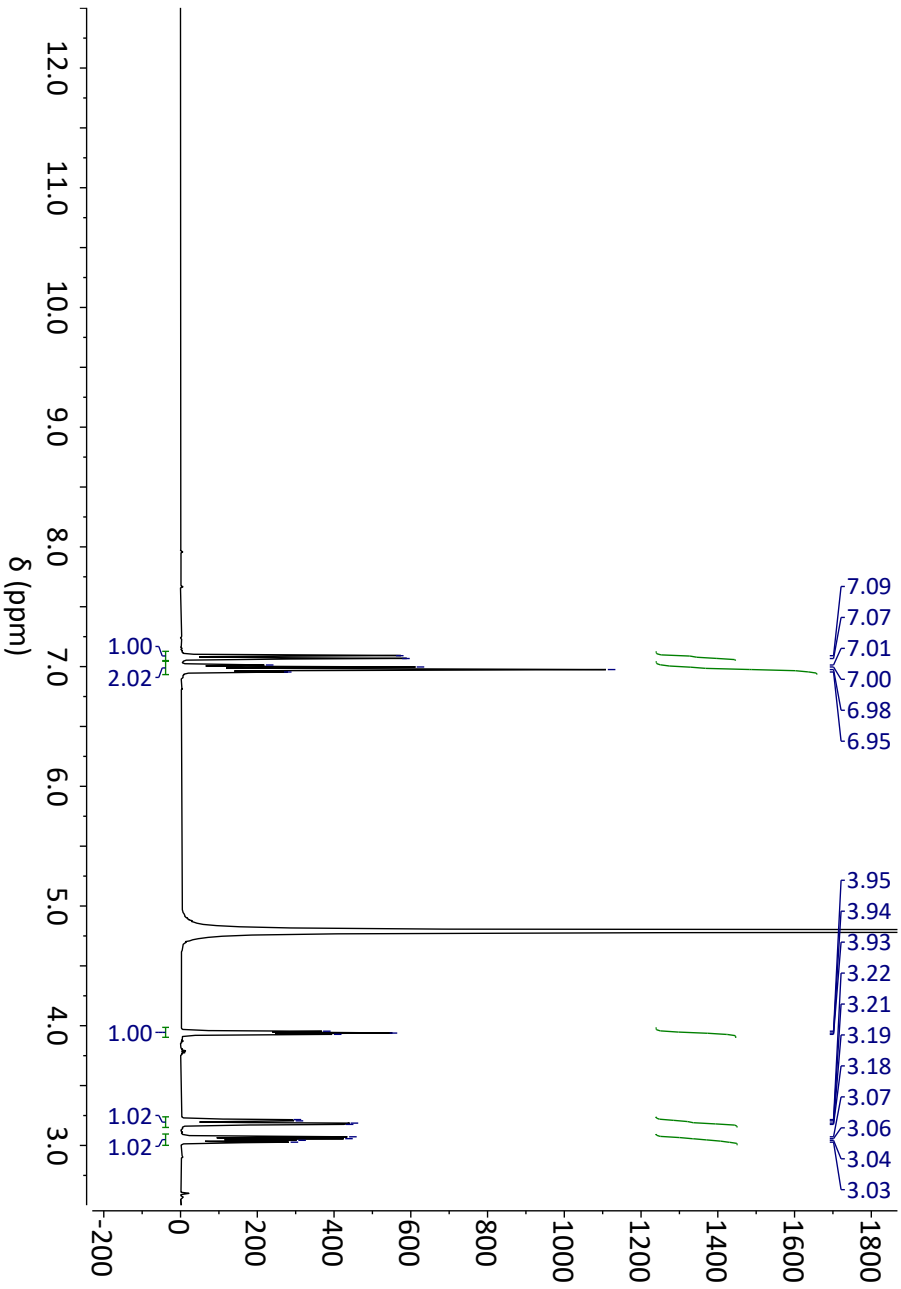

Figure A.1. ^{1}H NMR spectrum (500 MHz) for 3-fluorotyrosine in D_2O.

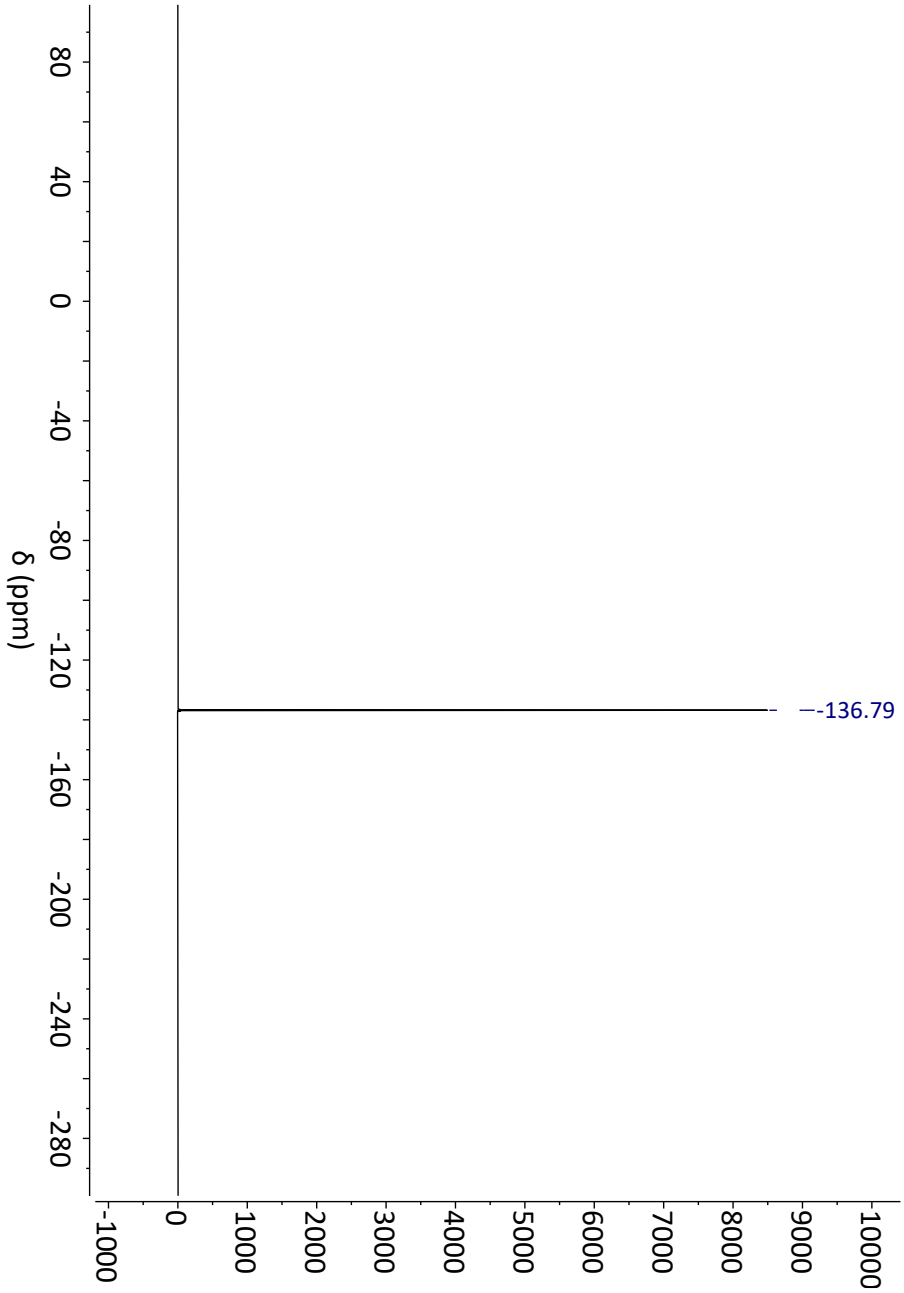

Figure A.2. **^{19}F NMR spectrum (500 MHz) for 3-fluorotyrosine in D_2O.**

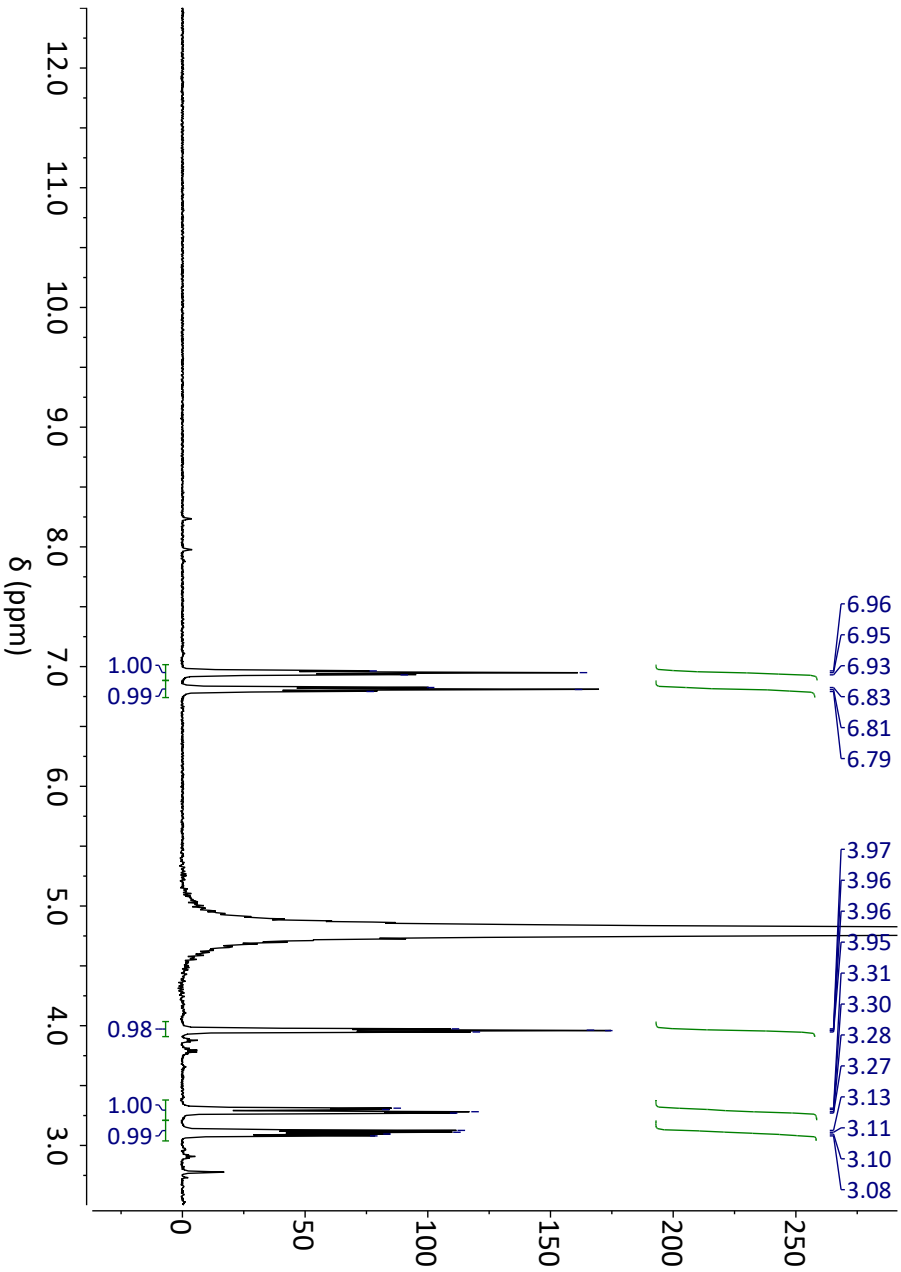

Figure A.3. ^{1}H NMR spectrum (500 MHz) for 2,3-difluorotyrosine in D_2O.

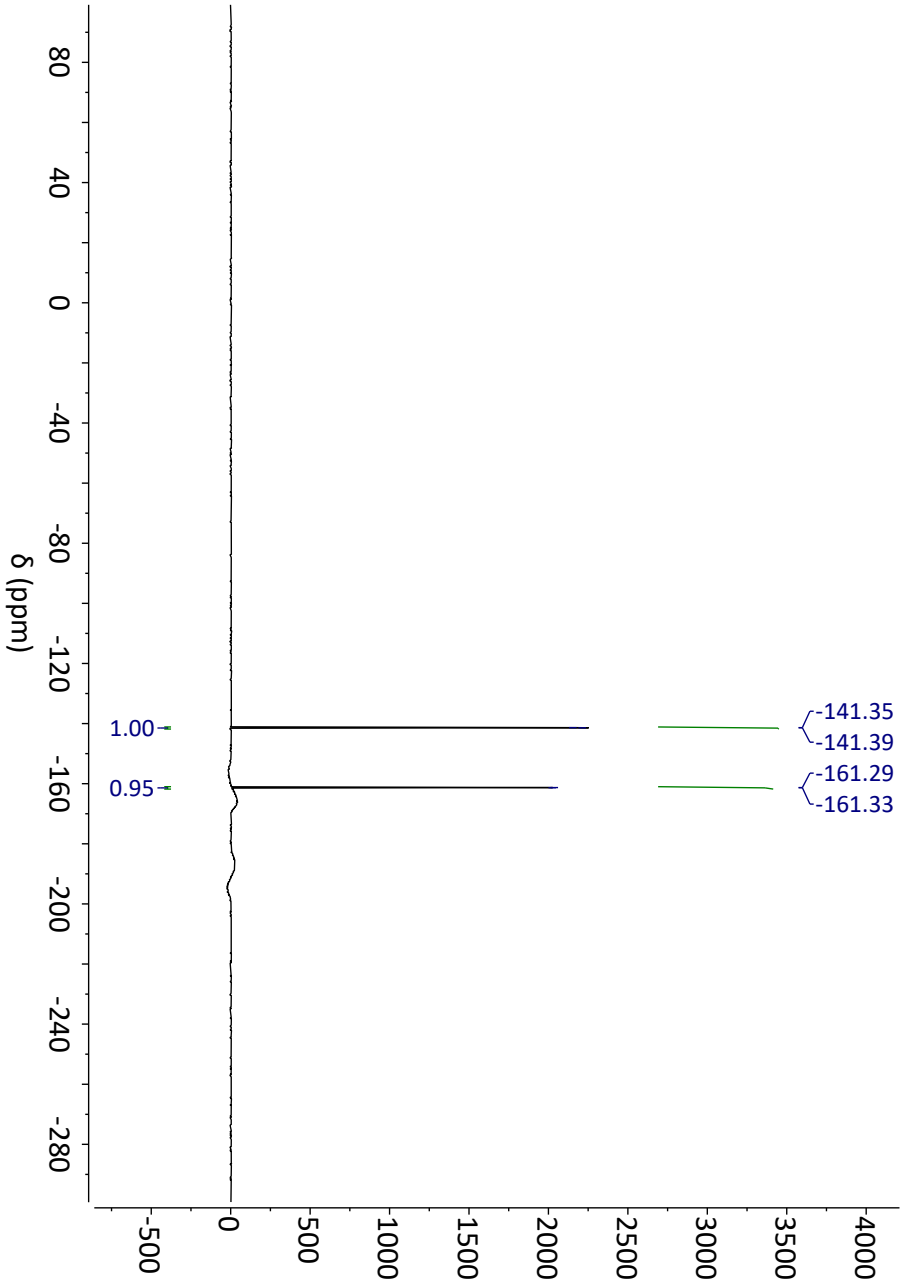

Figure A.4. **^{19}F NMR spectrum (500 MHz) for 2,3-difluorotyrosine in D_2O.**

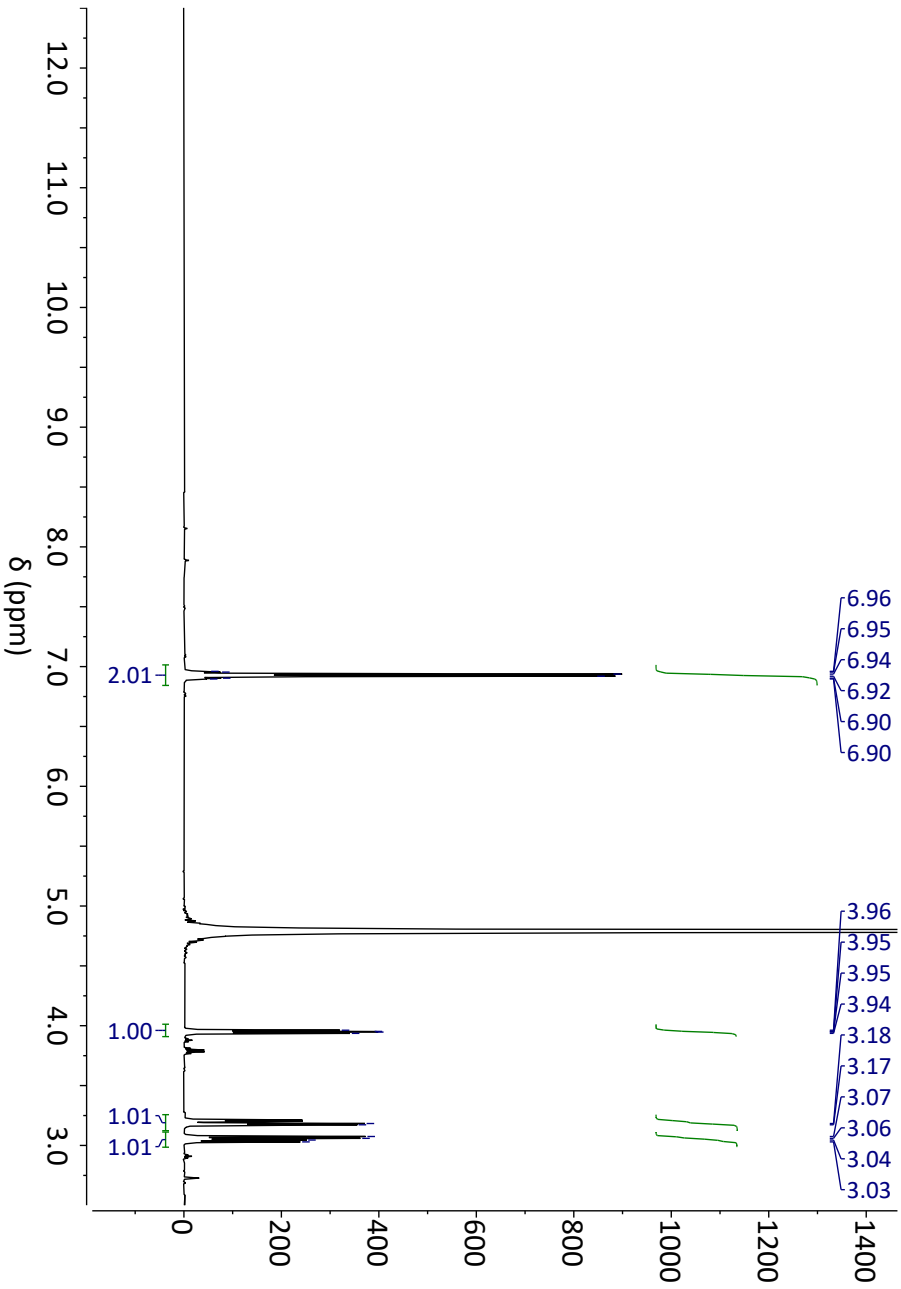

Figure A.5. **^{1}H NMR spectrum (500 MHz) for 3,5-difluorotyrosine in D_2O.**

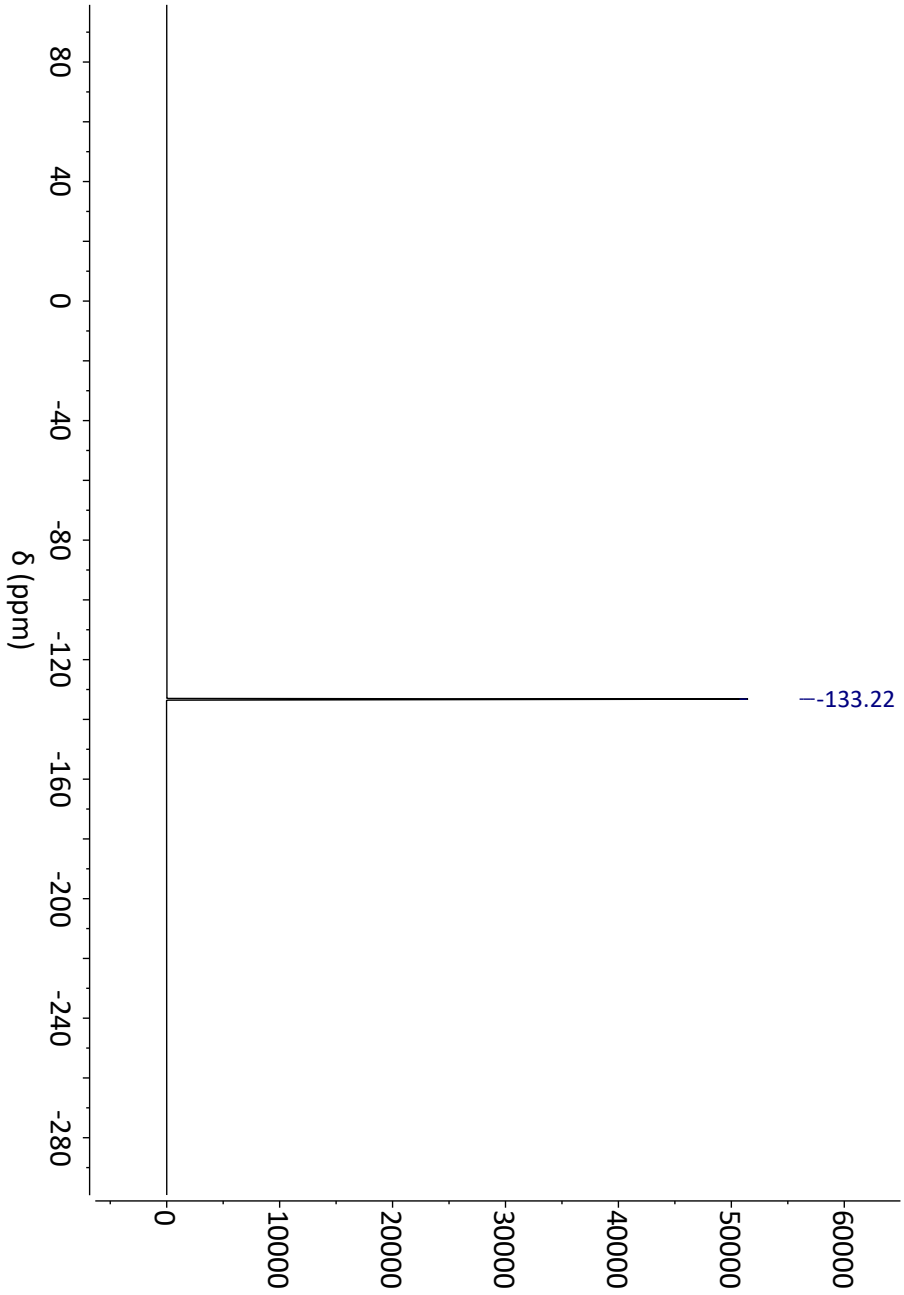

Figure A.6. **^{19}F NMR spectrum (500 MHz) for 3,5-difluorotyrosine in D_2O.**

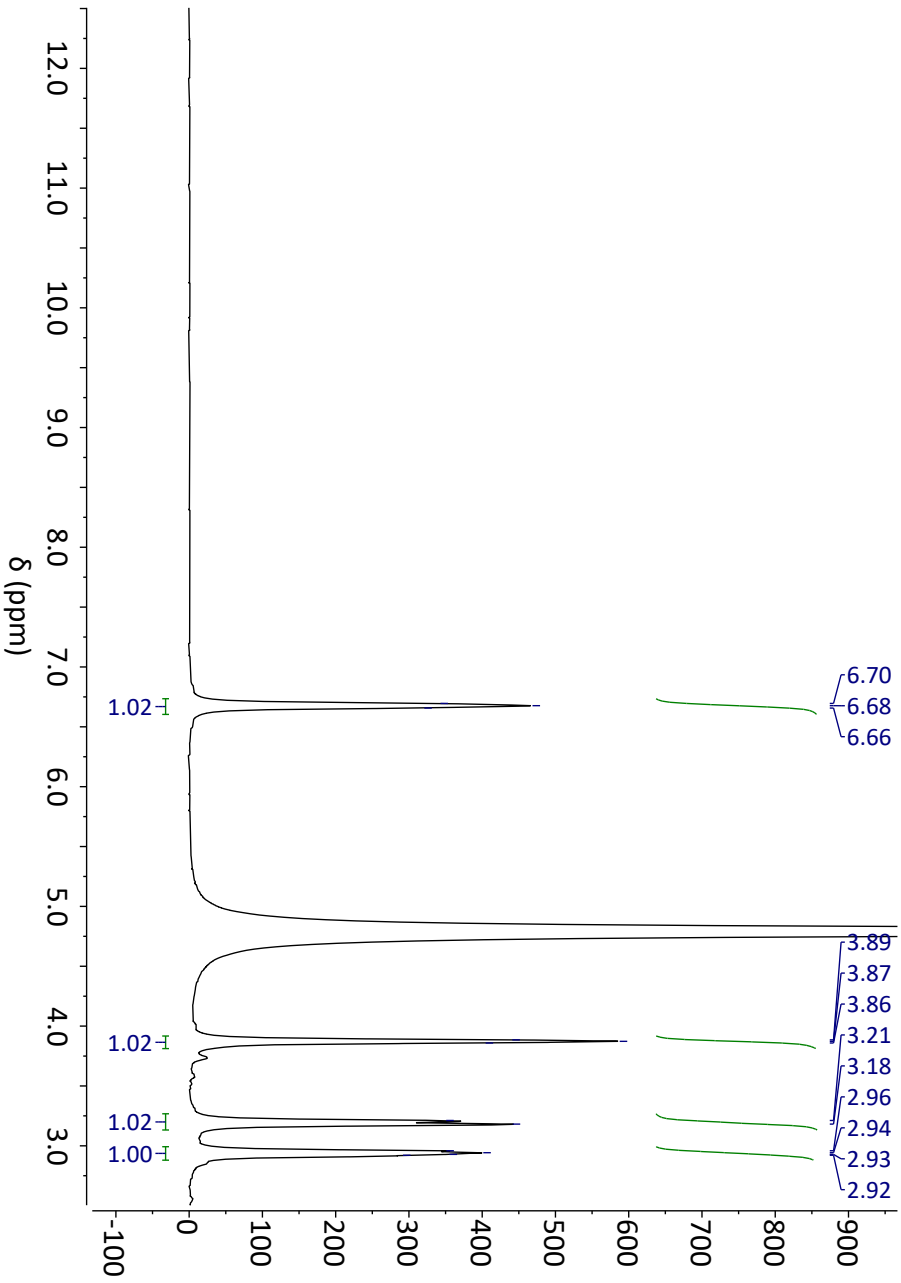

Figure A.7. ^{1}**H NMR spectrum (500 MHz) for 2,3,5-trifluorotyrosine in** D_2O**.**

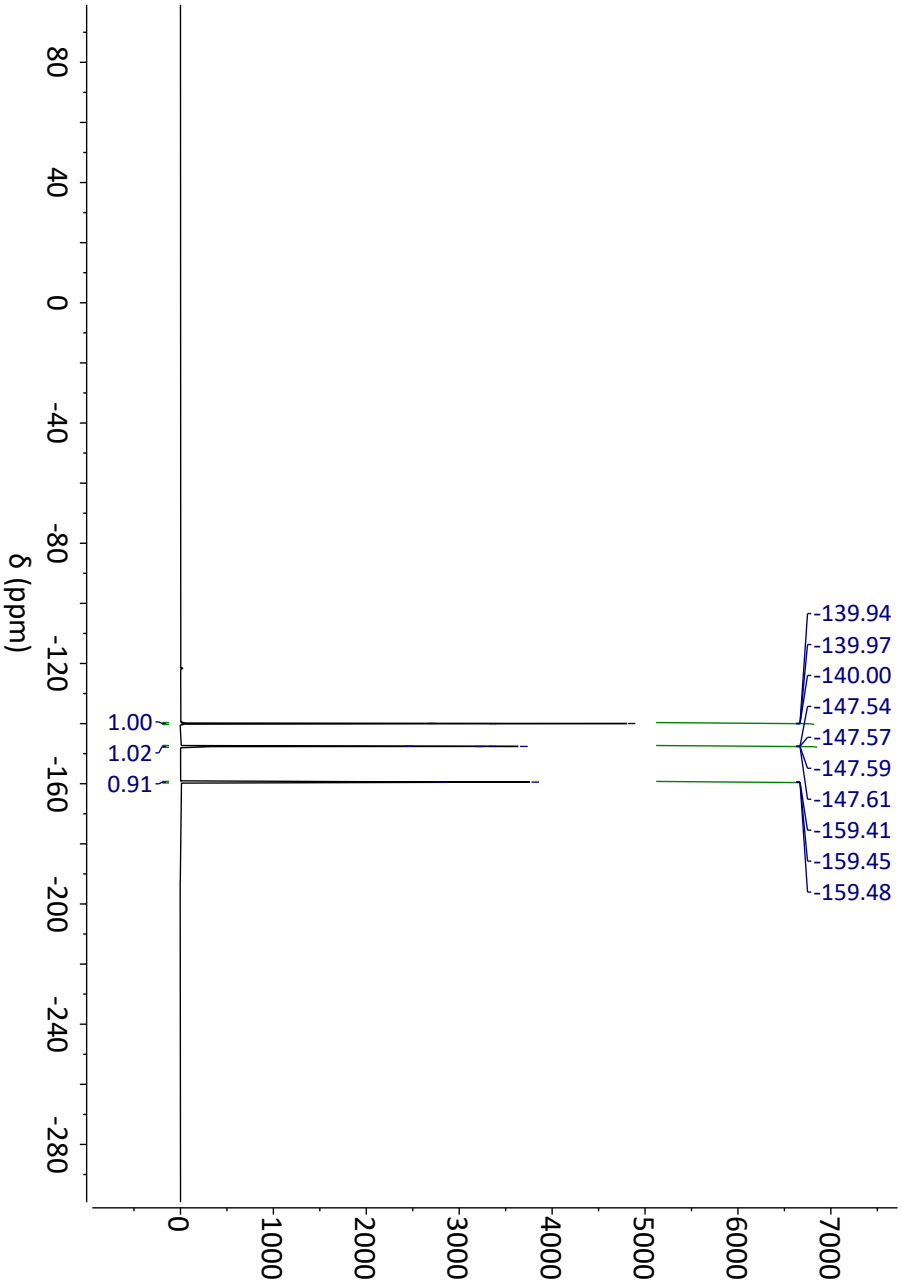

Figure A.8. **^{19}F NMR spectrum (500 MHz) for 2,3,5-trifluorotyrosine in D_2O.**

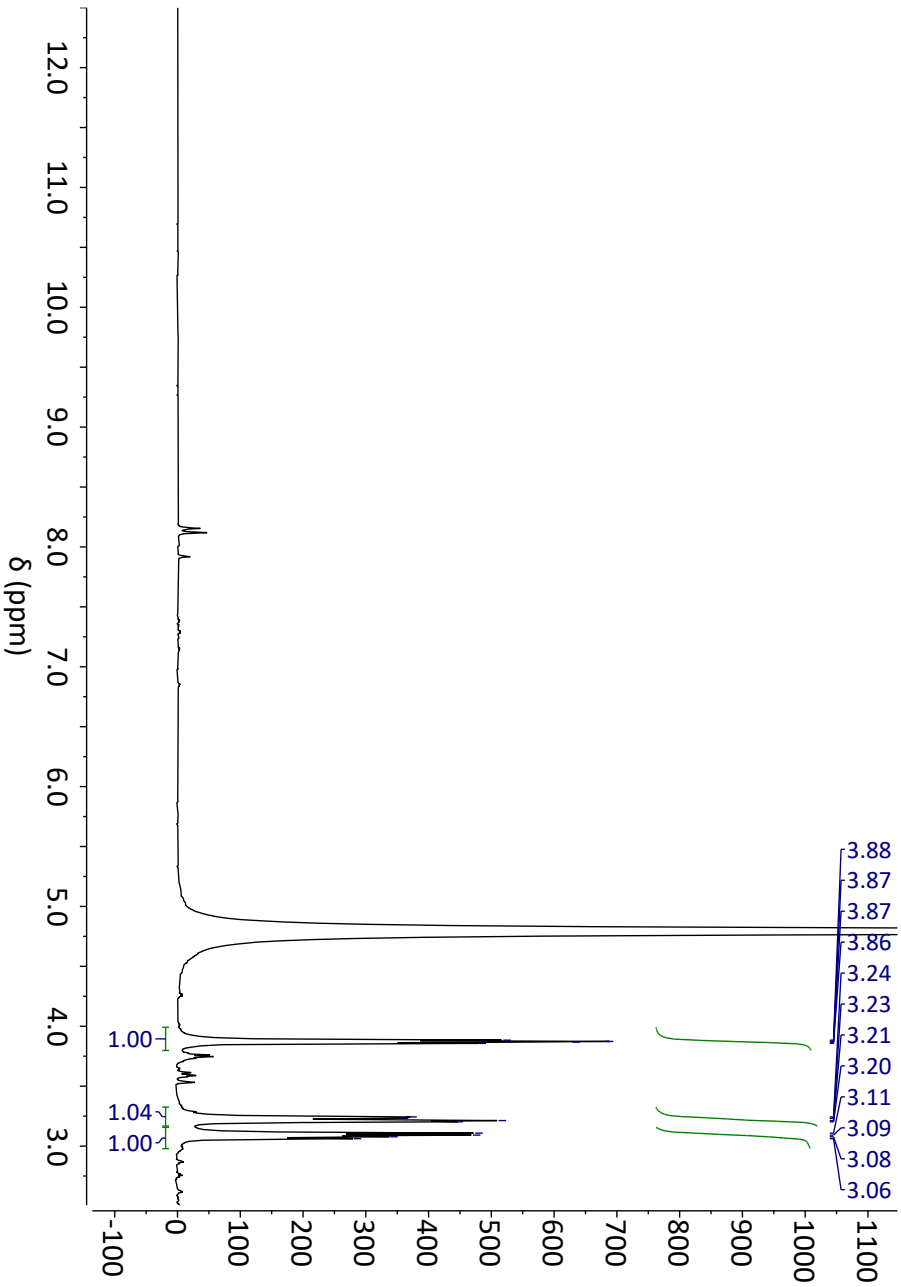

Figure A.9. ^{1}H NMR spectrum (500 MHz) for 2,3,5,6-tetrafluorotyrosine in D_2O.

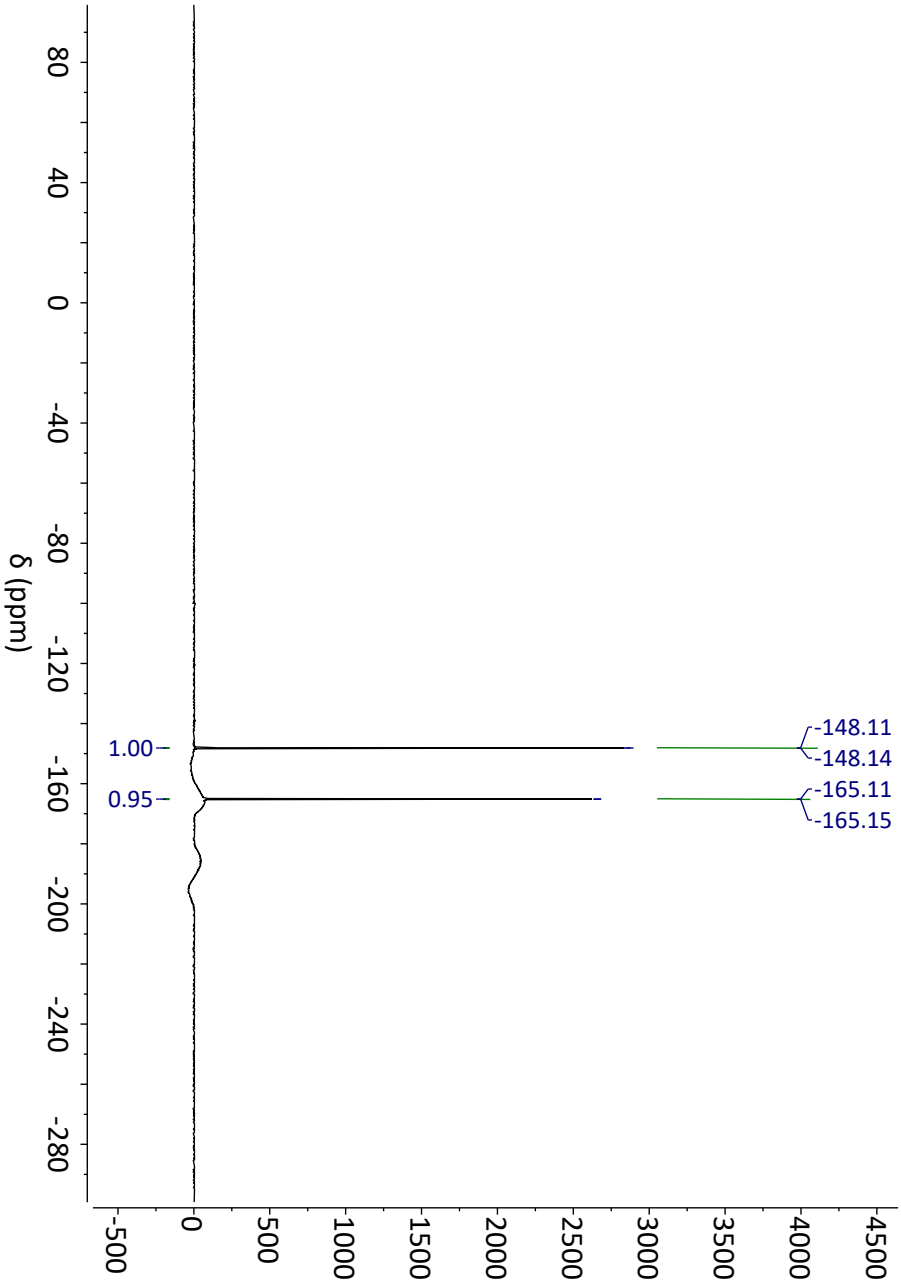

Figure A.10. ^{19}F NMR spectrum (500 MHz) for 2,3,5,6-tetrafluorotyrosine in D_2O.

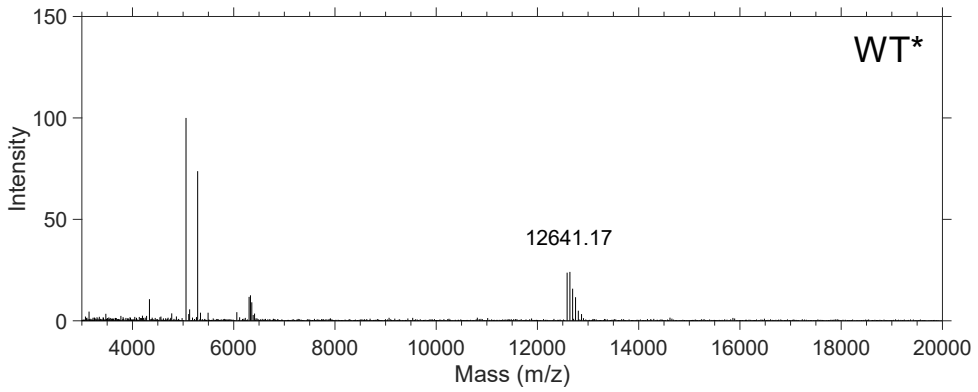

Figure A.11. MALDI-TOF mass spectrometry of Fe(III) yeast iso-1 cytochrome *c* WT* expressed from the combined pETDuet-1-*ccmABCDEFGH/CYC1*$_{\text{Glu66Cys/Tyr67TAG}}$ plasmid. Expected mass: 12655 Da; observed mass: 12641 Da.

Appendix B.

Supporting information for Chapter 3

Table B.1 Primers for Asn62Cys series of *CYC1* mutants.

Mutation		Sequence (5' → 3')
Asn62Cys	Forward	GGACGAATGTAACATGTCAGAGTACTTGACTAAC
	Reverse	CATGTTACATTCGTCCCACAACACGTTTTTCTTG
Asp60Ala	Forward	GTTGTGGGCCGAATGTAACATGTCAGAGTACTTGACTAAC
	Reverse	CATTCGGCCCACAACACGTTTTTCTTGATATTGGC
Asn62Cys/Trp59Tyr	Forward	GTGTTGTATGACGAATGTAACATGTCAGAGTACTTG
	Reverse	CATTCGTCATACAACACGTTTTTCTTGATATTGGC
Asn62Cys/Trp59Phe	Forward	CGTGTTGTTTGACGAATGTAACATGTCAGAGTACTTG
	Reverse	CATTCGTCAAACAACACGTTTTTCTTGATATTGGC
Asn62Cys/Met64Leu	Forward	AAACGTGTTGTGGGACGAATGTAACCTGTCAGA
	Reverse	GCTGGGTTAGTCAAGTACTCTGACAGGTTACAT
Asn62Cys/Asp60Ala/ Trp59Tyr	Forward	GTGTTGTATGCCGAATGTAACATGTCAGAGTACTTG
	Reverse	CATTCGGCATACAACACGTTTTTCTTGATATTGGC
Asn62Cys/Asp60Ala/ Trp59phe	Forward	GTGTTGTTTGCCGAATGTAACATGTCAGAGTACTTG
	Reverse	CATTCGGCAAACAACACGTTTTTCTTGATATTGGC

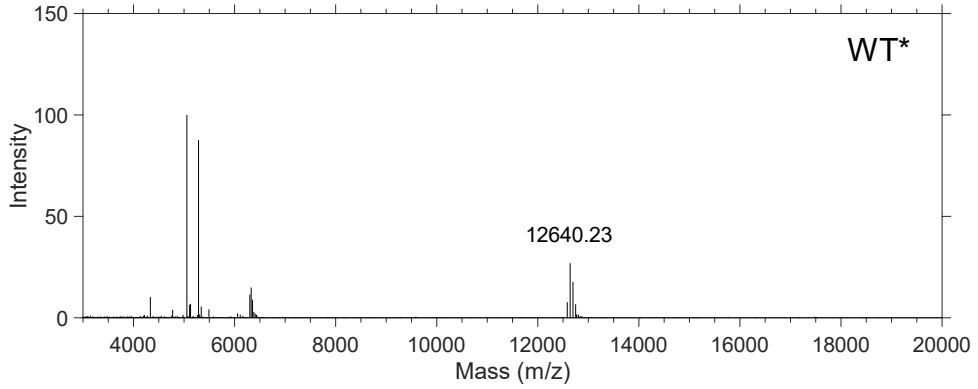

Figure B.1. MALDI-TOF mass spectrometry of Fe(III) yeast iso-1 cytochrome *c* WT*. Expected mass: 12655 Da; observed mass: 12640 Da.

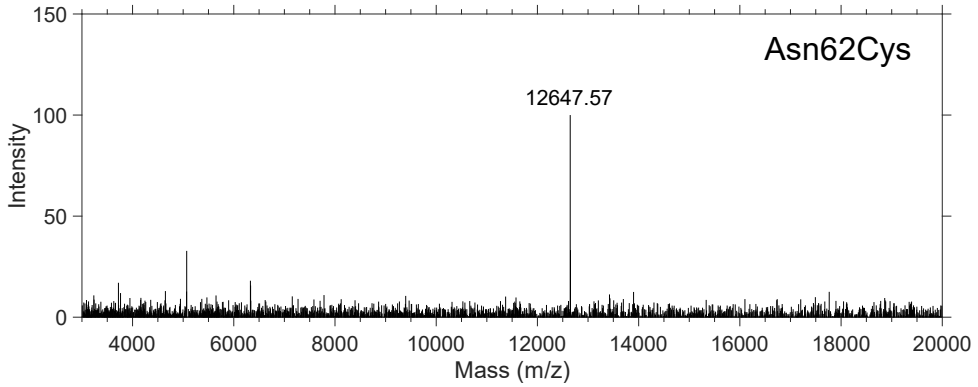

Figure B.2. MALDI-TOF mass spectrometry of unlabelled Fe(III) yeast iso-1 cytochrome *c* Asn62Cys. Expected mass: 12644 Da; observed mass: 12648 Da.

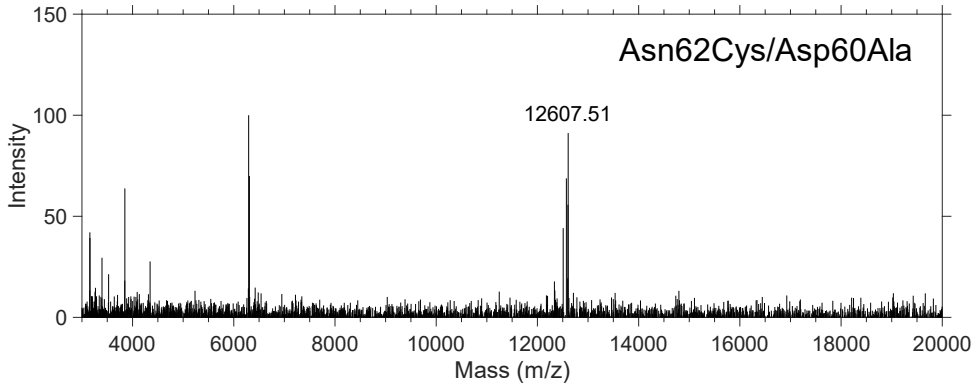

Figure B.3. MALDI-TOF mass spectrometry of unlabelled Fe(III) yeast iso-1 cytochrome *c* Asn62Cys/Asp60Ala. Expected mass: 12600 Da; observed mass: 12608 Da.

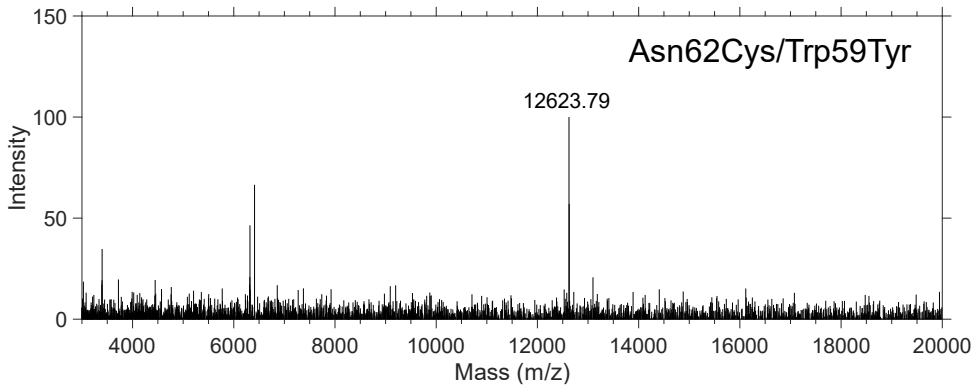

Figure B.4. MALDI-TOF mass spectrometry of unlabelled Fe(III) yeast iso-1 cytochrome *c* Asn62Cys/Trp59Tyr. Expected mass: 12621 Da; observed mass: 12624 Da.

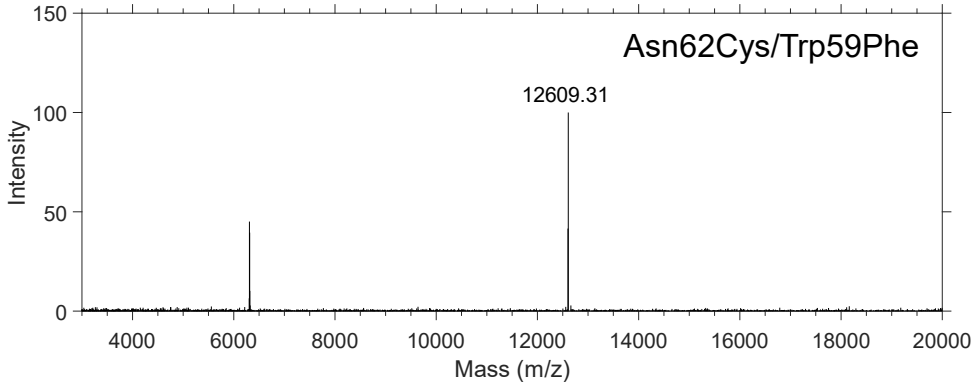

Figure B.5. MALDI-TOF mass spectrometry of unlabelled Fe(III) yeast iso-1 cytochrome *c* Asn62Cys/Trp59Phe. Expected mass: 12605 Da; observed mass: 12609 Da.

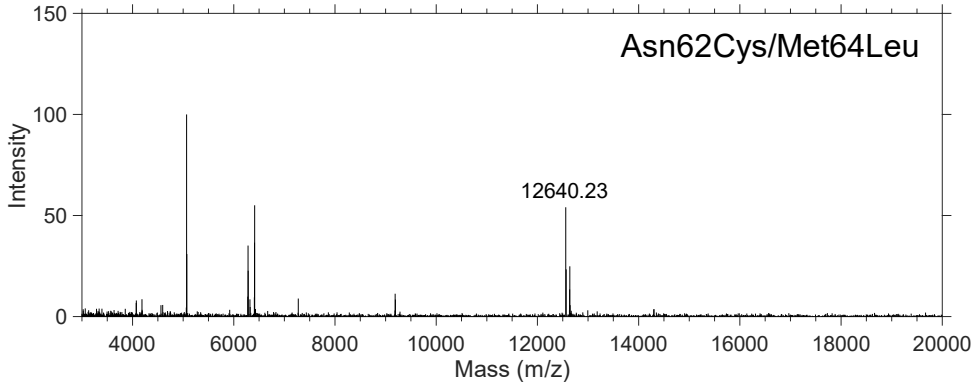

Figure B.6. MALDI-TOF mass spectrometry of unlabelled Fe(III) yeast iso-1 cytochrome *c* Asn62Cys/Met64Leu. Expected mass: 12626 Da; observed mass: 12640 Da.

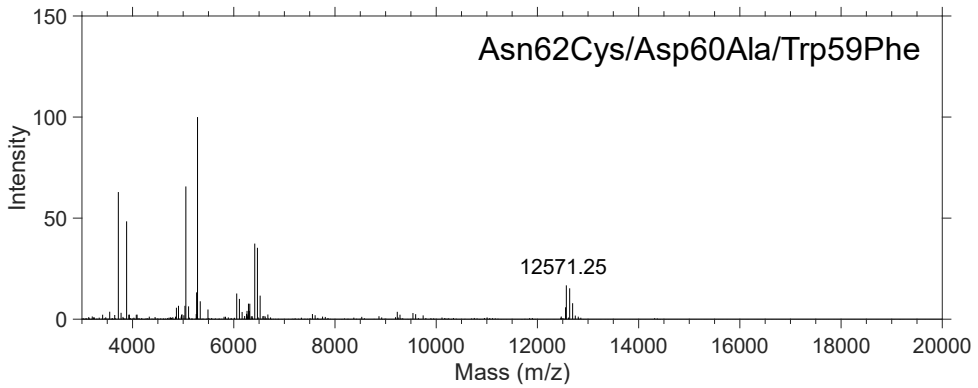

Figure B.7. MALDI-TOF mass spectrometry of unlabelled Fe(III) yeast iso-1 cytochrome *c* Asn62Cys/Asp60Ala/Trp59Phe. Expected mass: 12561 Da; observed mass: 12571 Da.

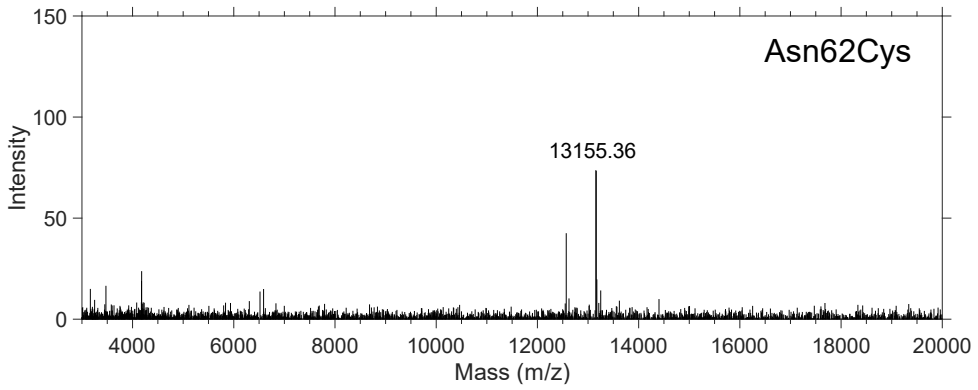

Figure B.8. MALDI-TOF mass spectrometry of (2,2´-bipyridyl)$_2$(5-cysteinyl-1,10-phenanthroline)Ru(II)-modified yeast iso-1 cytochrome *c* Asn62Cys. Expected mass: 13147 Da; observed mass: 13155 Da.

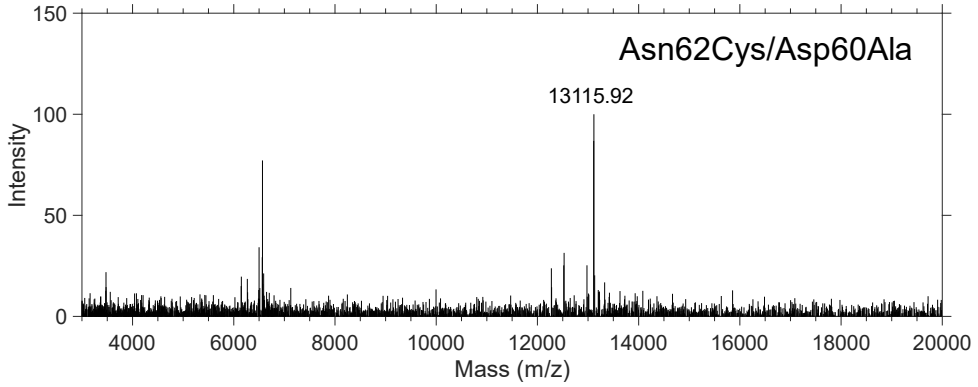

Figure B.9. MALDI-TOF mass spectrometry of (2,2´-bipyridyl)$_2$(5-cysteinyl-1,10-phenanthroline)Ru(II)-modified yeast iso-1 cytochrome *c* Asn62Cys/Asp60Ala. Expected mass: 13103 Da; observed mass: 13116 Da.

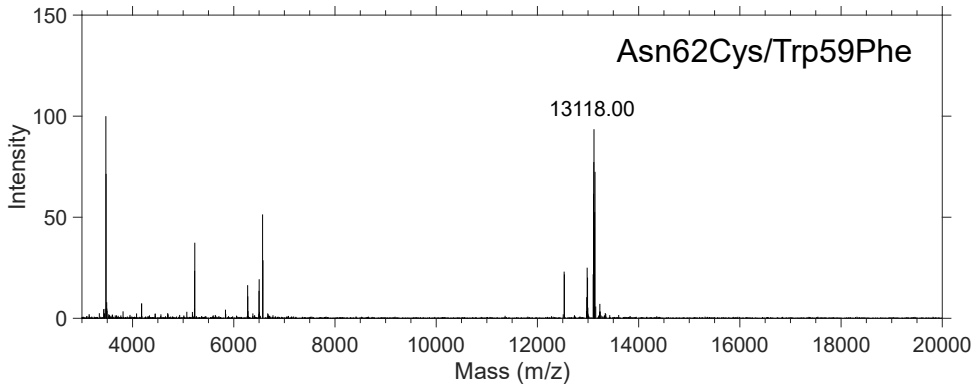

Figure B.10. MALDI-TOF mass spectrometry of (2,2´-bipyridyl)$_2$(5-cysteinyl-1,10-phenanthroline)Ru(II)-modified yeast iso-1 cytochrome *c* Asn62Cys/Trp59Phe. Expected mass: 13108 Da; observed mass: 13118 Da.

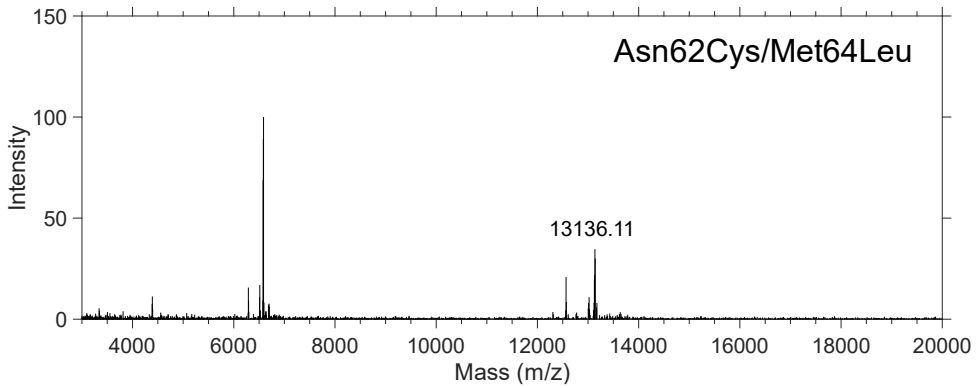

Figure B.11. MALDI-TOF mass spectrometry of (2,2´-bipyridyl)$_2$(5-cysteinyl-1,10-phenanthroline)Ru(II)-modified yeast iso-1 cytochrome *c* Asn62Cys/Met64Leu. Expected mass: 13129 Da; observed mass: 13136 Da.

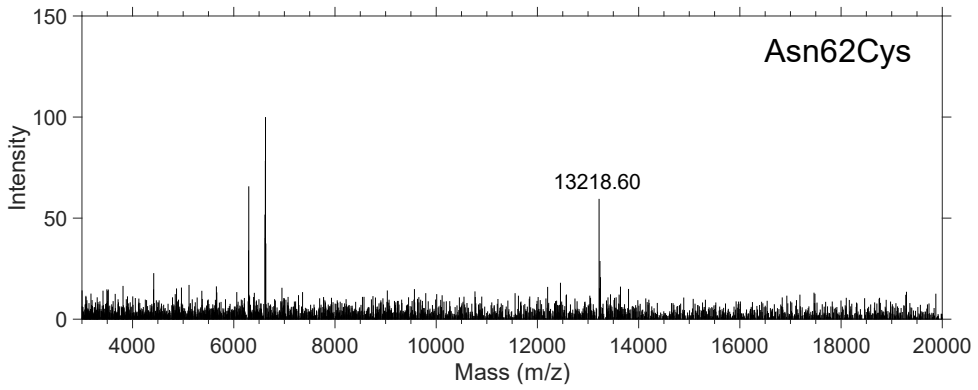

Figure B.12. MALDI-TOF mass spectrometry of (4-4´-dimethyl-2,2´-bipyridyl)$_2$(5-cysteinyl-1,10-phenanthroline)Ru(II)-modified yeast iso-1 cytochrome *c* Asn62Cys. Expected mass: 13203 Da; observed mass: 13219 Da.

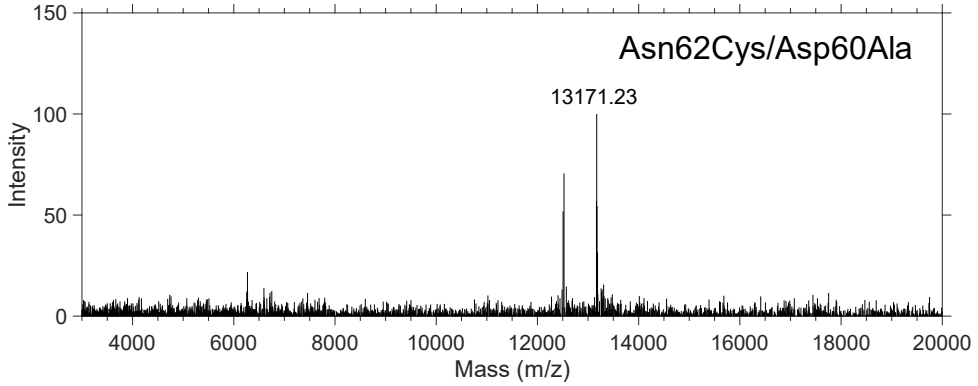

Figure B.13. MALDI-TOF mass spectrometry of (4-4´-dimethyl-2,2´-bipyridyl)$_2$(5-cysteinyl-1,10-phenanthroline)Ru(II)-modified yeast iso-1 cytochrome *c* Asn62Cys/Asp60Ala. Expected mass: 13159 Da; observed mass: 13171 Da.

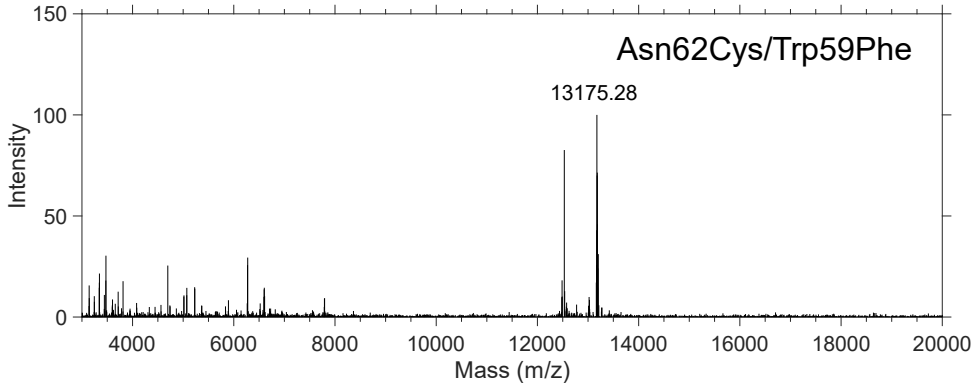

Figure B.14. MALDI-TOF mass spectrometry of (4-4´-dimethyl-2,2´-bipyridyl)$_2$(5-cysteinyl-1,10-phenanthroline)Ru(II)-modified yeast iso-1 cytochrome *c* Asn62Cys/Trp59Phe. Expected mass: 13164 Da; observed mass: 13175 Da.

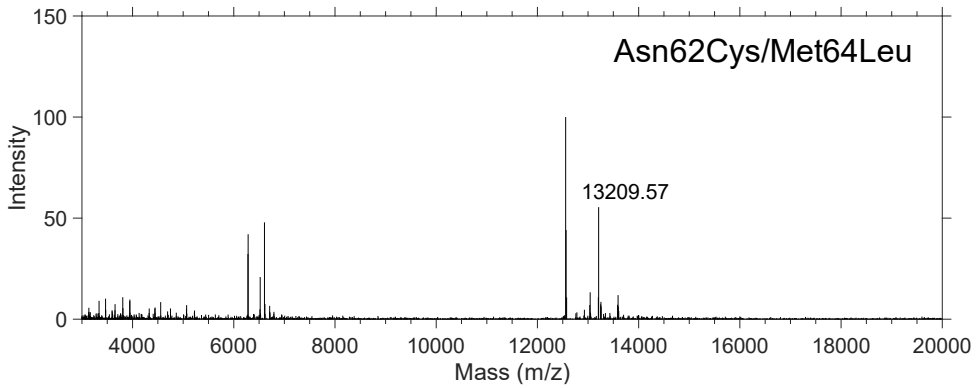

Figure B.15. MALDI-TOF mass spectrometry of (4-4´-dimethyl-2,2´-bipyridyl)$_2$(5-cysteinyl-1,10-phenanthroline)Ru(II)-modified yeast iso-1 cytochrome *c* Asn62Cys/Met64Leu. Expected mass: 13185 Da; observed mass: 13210 Da.

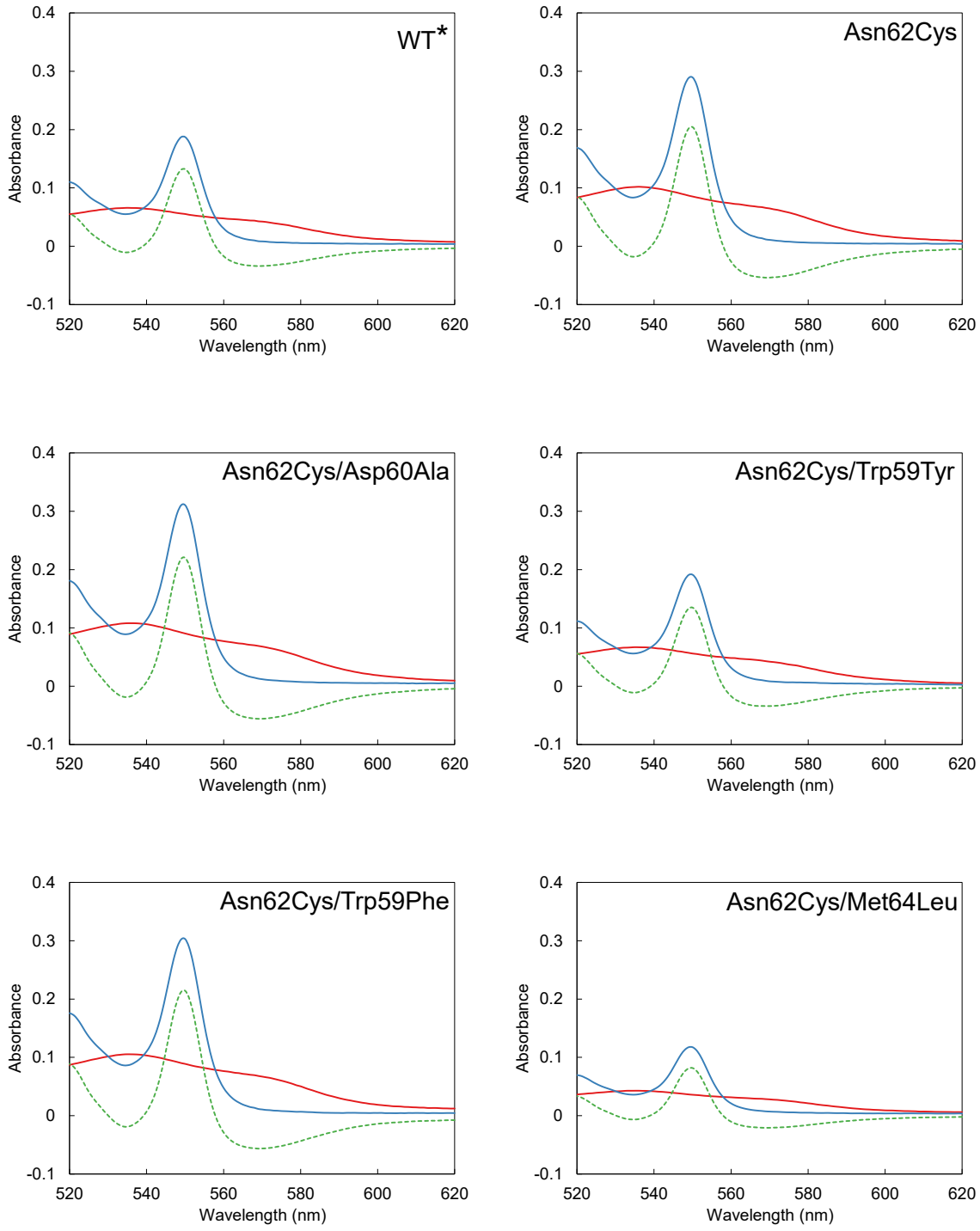

Figure B.16. UV–Vis spectra of the pyridine hemochrome assay for Fe(III) (red line), Fe(II) (blue line), and Fe(III)-Fe(II) difference (green line) for cytochrome *c* WT* and variants. Absorbance values were compared with published extinction coefficients for *c*-type cytochromes to determine the concentration of the original protein.[41]

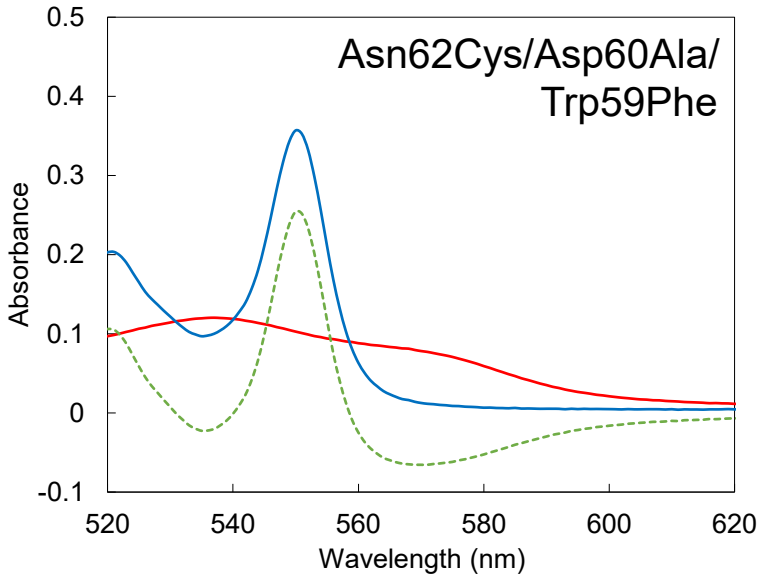

Figure B.17. UV–Vis spectra of the pyridine hemochrome assay for Fe(III) (red line), Fe(II) (blue line), and Fe(III)-Fe(II) difference (green line) for yeast iso-1 cytochrome *c* Asn62Cys/Asp60Ala/Trp59Phe. Absorbance values were compared with published extinction coefficients for *c*-type cytochromes to determine the concentration of the original protein.[41]

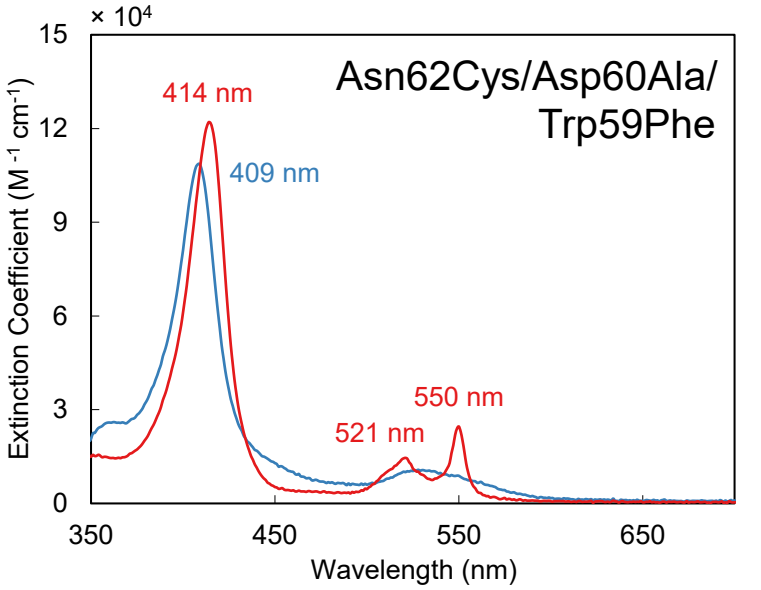

Figure B.18. Optical spectra of unmodified Fe(III) (blue trace) and Fe(II) (red trace) yeast iso-1 cytochrome *c* Asn62Cys/Asp60Ala/Trp59Phe in 5 mM sodium phosphate at pH 7.0.

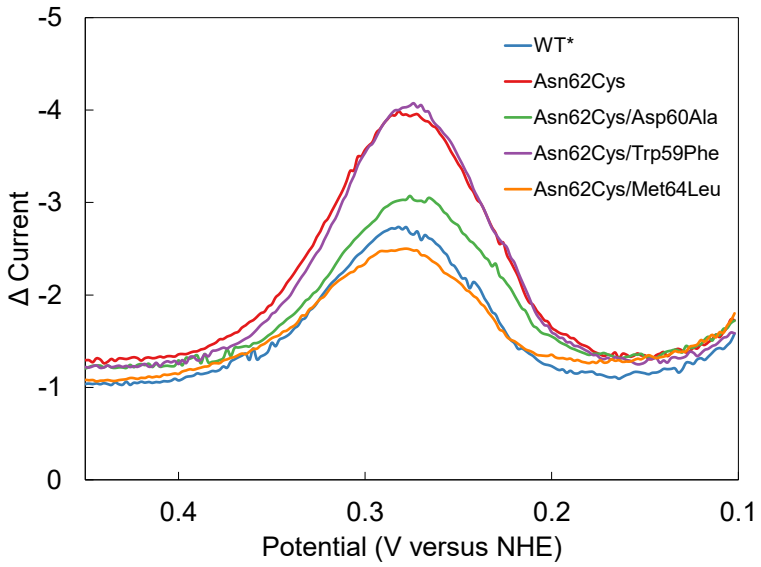

Figure B.19. Differential pulse voltammograms (DPV) of 100-200 μM unmodified yeast iso-1 cytochrome *c* at the surface of a gold electrode coated with 4-mercaptopyridine. All DPVs were recorded in 100 mM sodium phosphate at pH 7.0. DPV parameters: scan rate, 20 mV/s; pulse width, 100 ms; and amplitude, 25 mV.

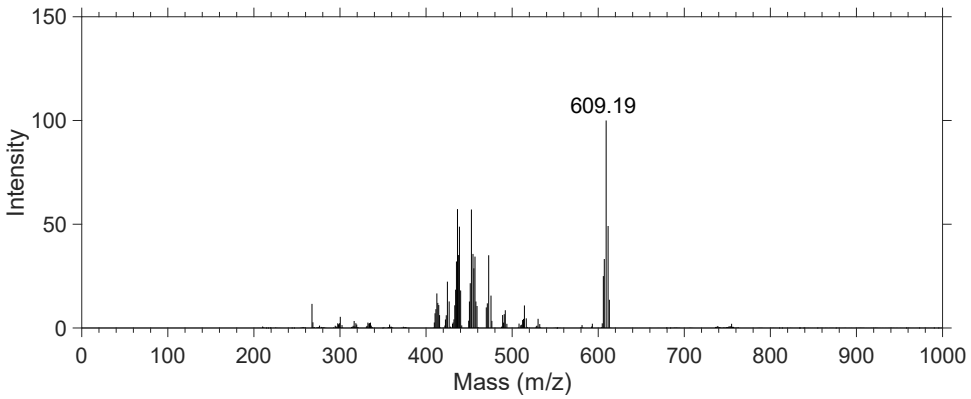

Figure B.20. MALDI-TOF mass spectrometry of [Ru(2,2´-bipyridyl)$_2$(5,6-epoxy-5,6-dihydro-1,10-phenanthroline)](PF$_6$)$_2$. Expected mass: 609.11 Da; observed mass: 609.19 Da.

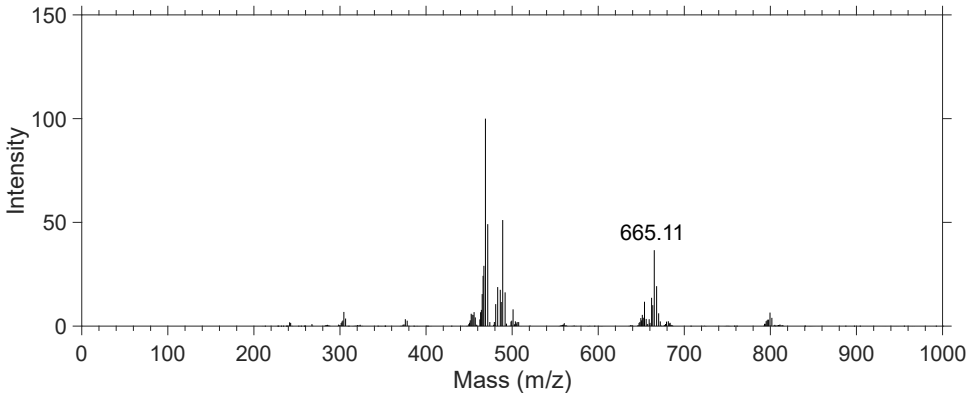

Figure B.21. MALDI-TOF mass spectrometry of [Ru(4-4´-dimethyl-2,2´-bipyridyl)$_2$(5,6-epoxy-5,6-dihydro-1,10-phenanthroline)](PF$_6$)$_2$. Expected mass: 665.17 Da; observed mass: 665.11 Da.

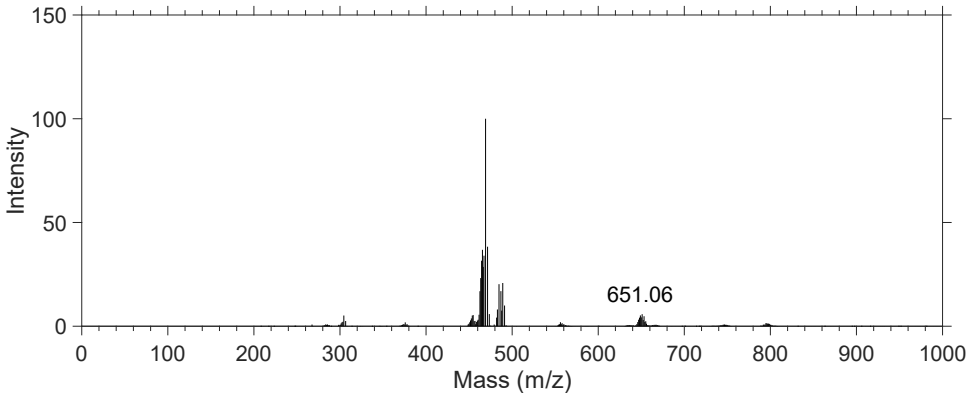

Figure B.22. MALDI-TOF mass spectrometry of [Ru(4-4´-dimethyl-2,2´-bipyridyl)$_2$(1,10-phenanthroline)](PF$_6$)$_2$. Expected mass: 651.18 Da; observed mass: 651.06 Da.

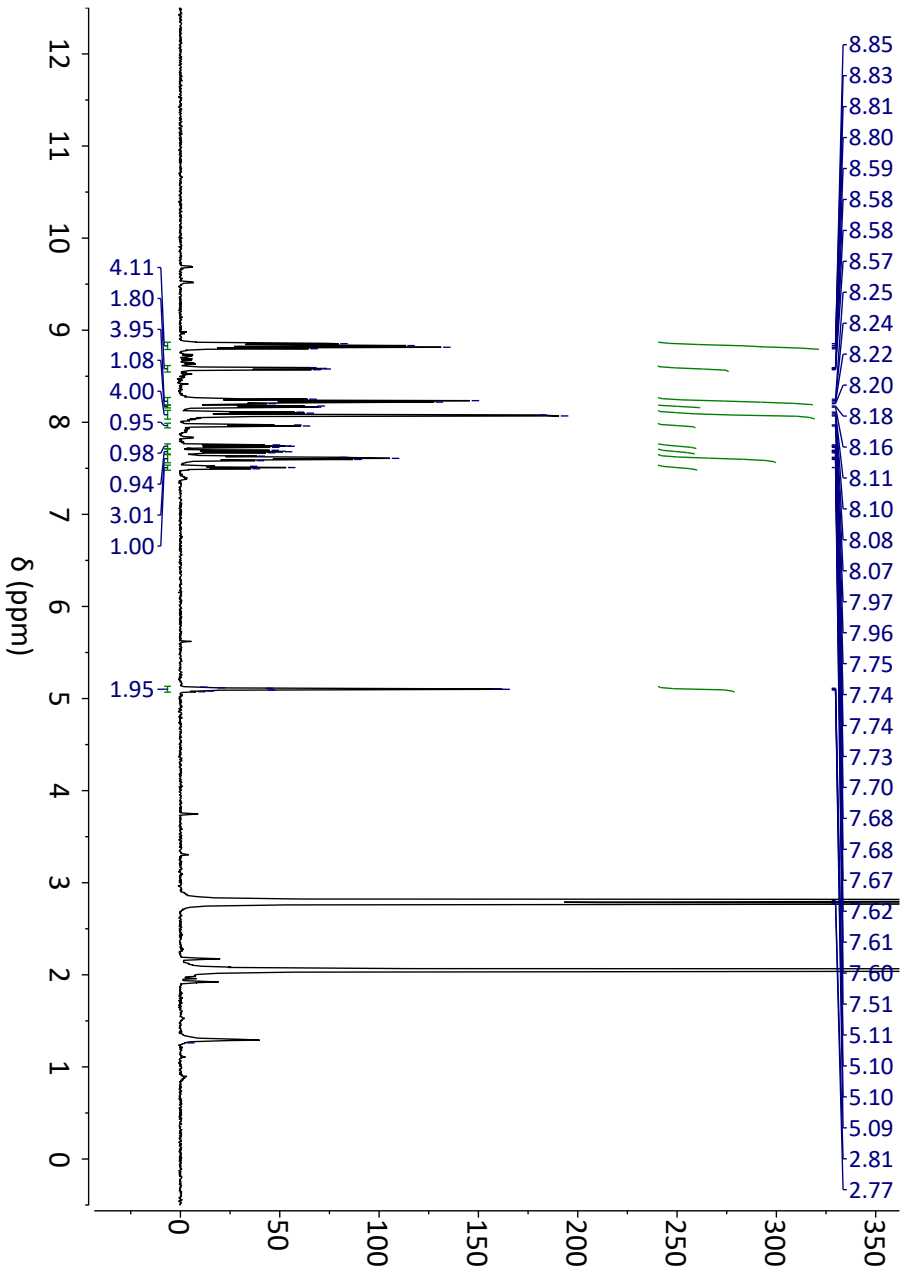

Figure B.23. ^{1}H NMR spectrum (500 MHz) for [Ru(2,2´-bipyridyl)$_2$(5,6-epoxy-5,6-dihydro-1,10-phenanthroline)](PF$_6$)$_2$ in acetone-d_6.

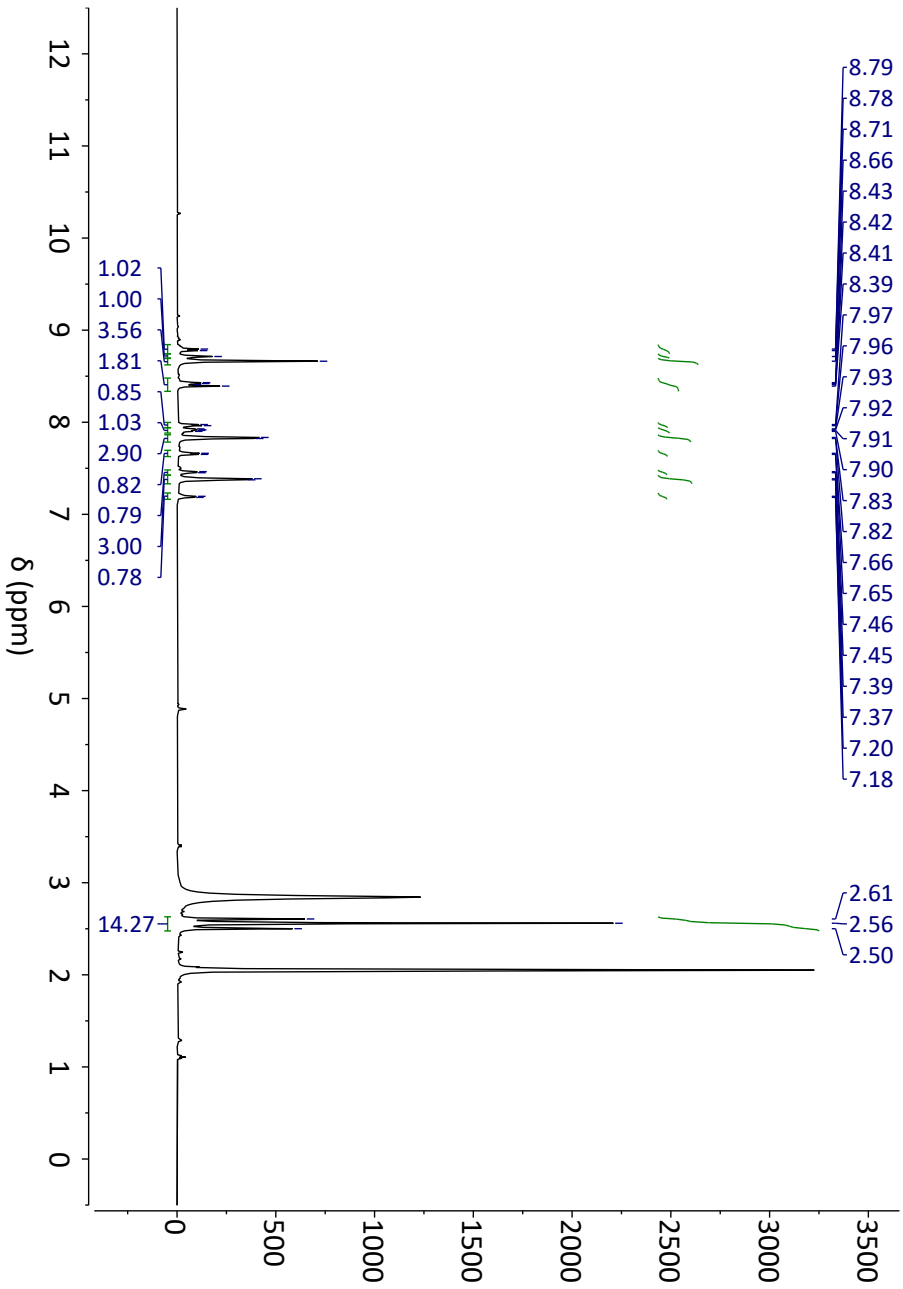

Figure B.24. ^{1}H NMR spectrum (500 MHz) for [Ru(4-4´-dimethyl-2,2´-bipyridyl)$_2$(1,10-phenanthroline)](PF$_6$)$_2$ in acetone-d_6.

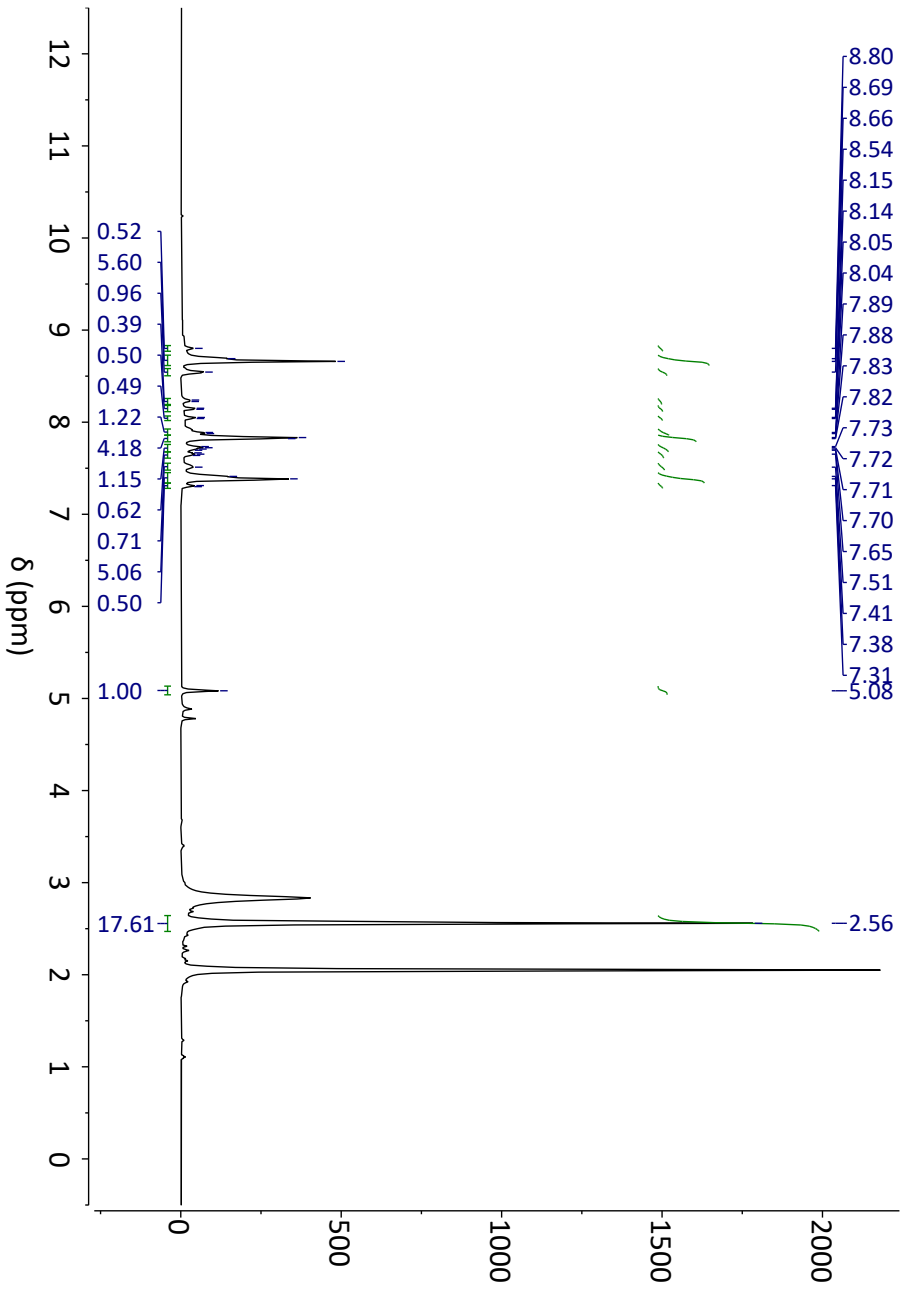

Figure B.25. ^{1}H NMR spectrum (500 MHz) for [Ru(4-4´-dimethyl-2,2´-bipyridyl)$_2$(5,6-epoxy-5,6-dihydro-1,10-phenanthroline)](PF$_6$)$_2$ in acetone-d_6.

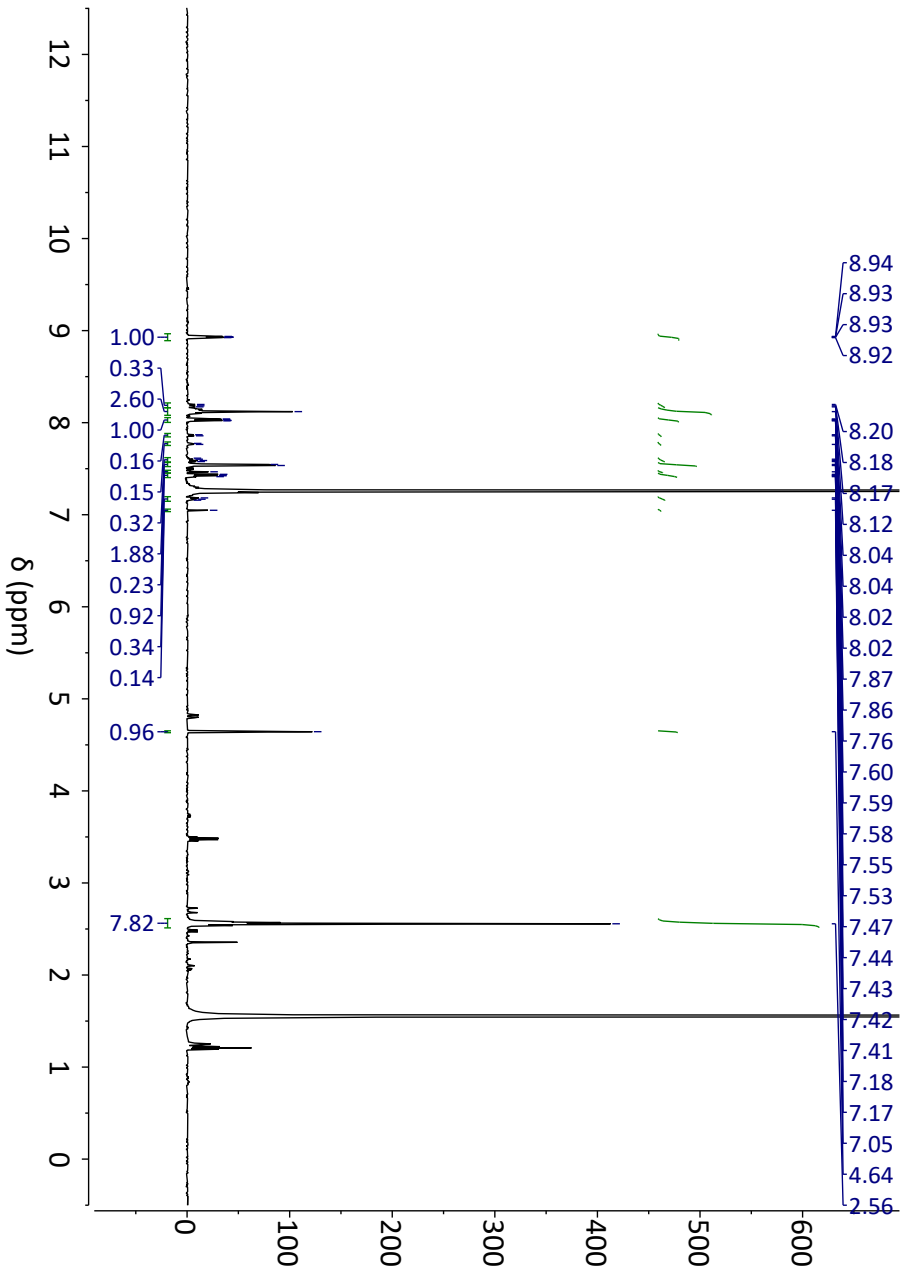

Figure B.26. ^{1}H NMR spectrum (500 MHz) for [Ru(4-4´-dimethyl-2,2´-bipyridyl)$_2$(5,6-epoxy-5,6-dihydro-1,10-phenanthroline)](PF$_6$)$_2$ in chloroform-*d*.

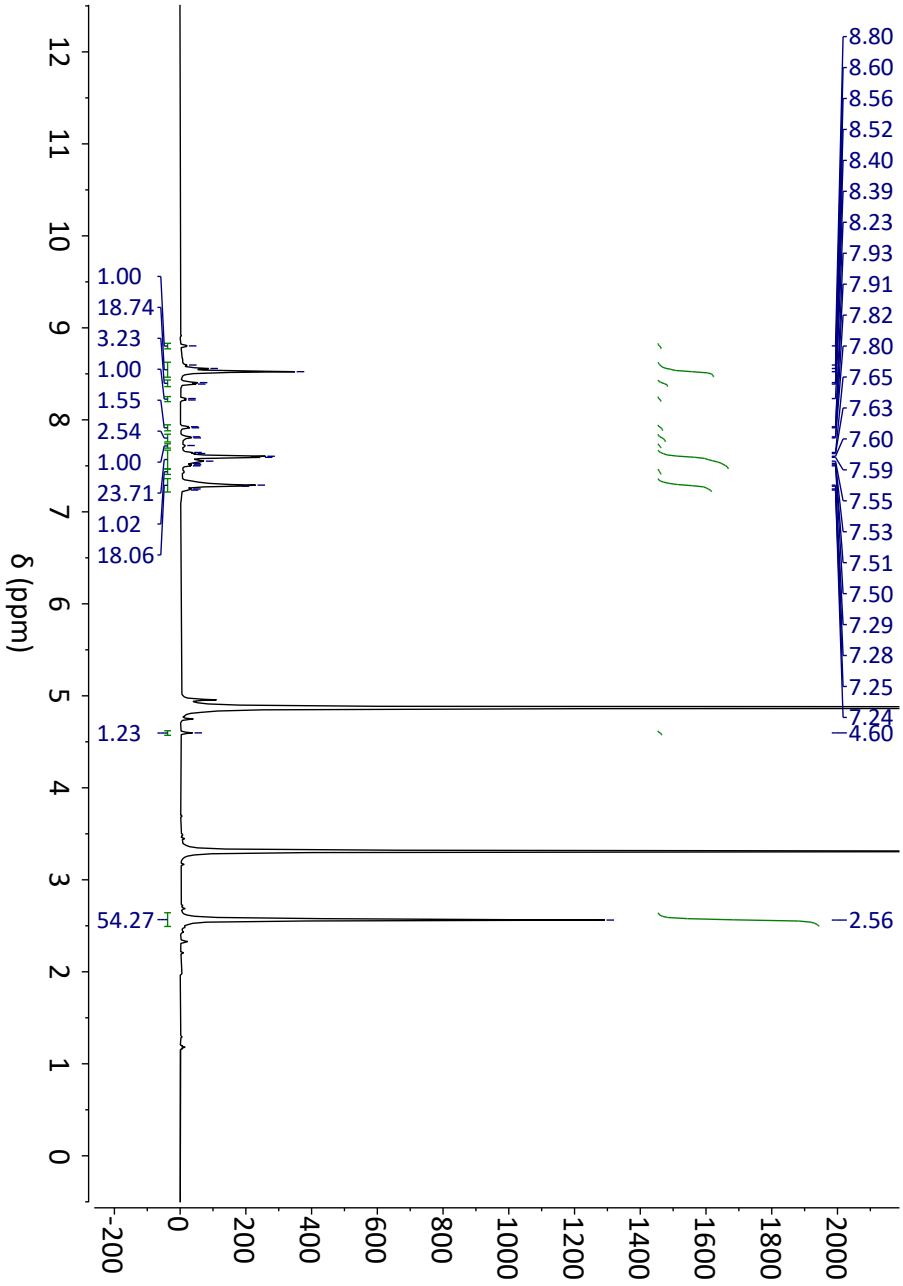

Figure B.27. ^{1}H NMR spectrum (500 MHz) for [Ru(4-4´-dimethyl-2,2´-bipyridyl)$_2$(5,6-epoxy-5,6-dihydro-1,10-phenanthroline)](PF$_6$)$_2$ in methanol-*d*$_4$.

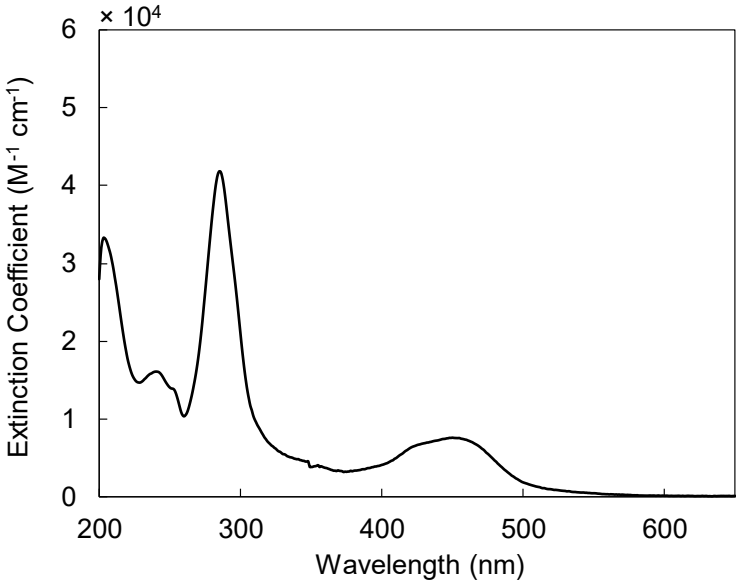

Figure B.28. Optical spectrum for [Ru(2,2´-bipyridyl)$_2$(5,6-epoxy-5,6-dihydro-1,10-phenanthroline)](PF$_6$)$_2$ in 100 mM sodium phosphate at pH 7.0.

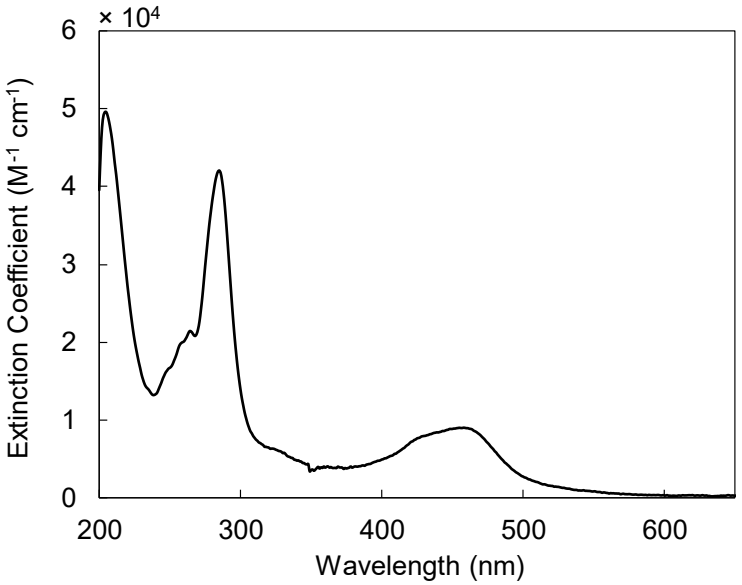

Figure B.29. Optical spectrum for [Ru(4-4´-dimethyl-2,2´-bipyridyl)$_2$(1,10-phenanthroline)](PF$_6$)$_2$ in 100 mM sodium phosphate at pH 7.0.

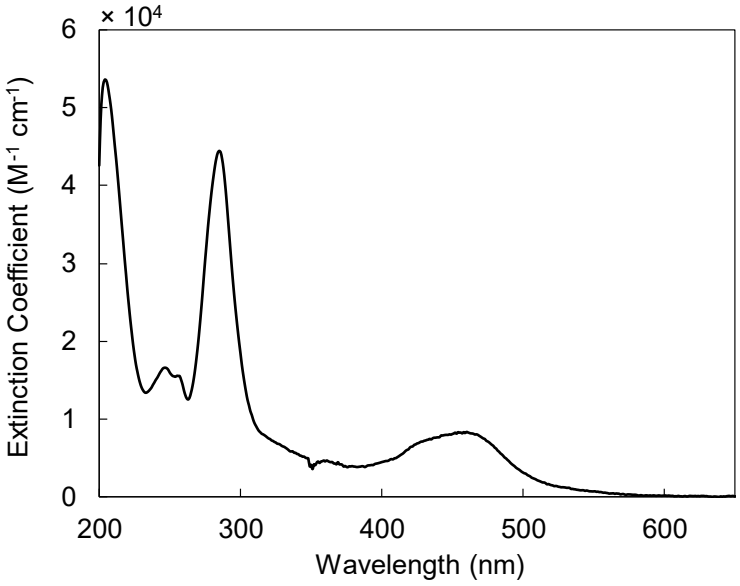

Figure B.30. Optical spectrum for [Ru(4-4´-dimethyl-2,2´-bipyridyl)$_2$(5,6-epoxy-5,6-dihydro-1,10-phenanthroline)](PF_6)$_2$ in 100 mM sodium phosphate at pH 7.0.

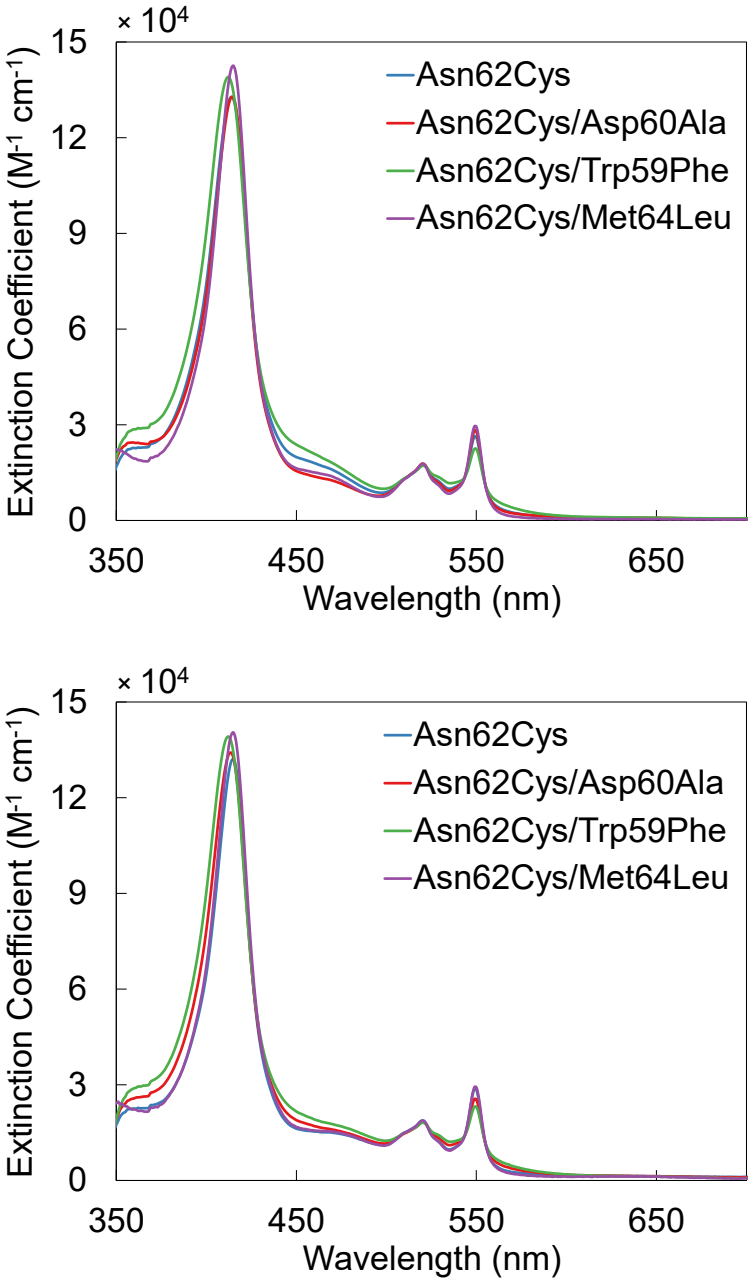

Figure B.31. Optical spectra of Fe(II)Ru-Asn62Cys, Fe(II)Ru-Asn62Cys/Asp60Ala, Fe(II)Ru-Asn62Cys/Trp59Phe and Fe(II)Ru-Asn62Cys/Met64Leu for $Ru(bpy)_2(phen)$ labelled (top) and $Ru(Me_2bpy)_2(phen)$ labelled (bottom) in 100 mM sodium phosphate at pH 7.0.

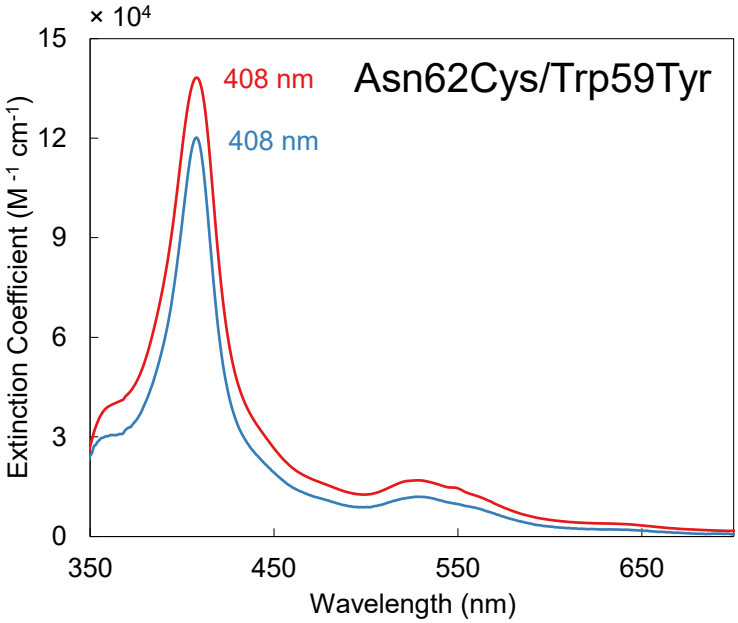

Figure B.32. Optical spectra of Fe(III) (blue trace) and Fe(II) (red trace) Asn62Cys/Trp59Tyr labelled with $Ru(bpy)_2(phen)$ in 100 mM sodium phosphate at pH 7.0.

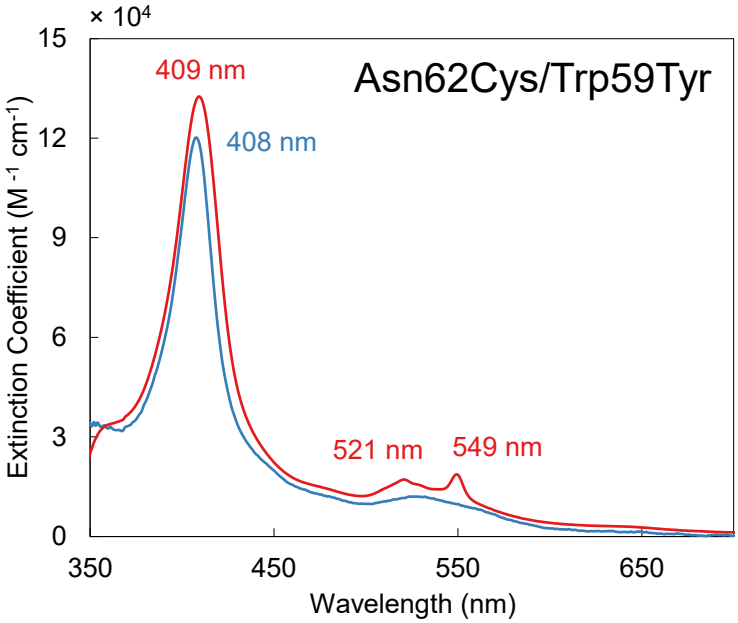

Figure B.33. Optical spectra of Fe(III) (blue trace) and Fe(II) (red trace) Asn62Cys/Trp59Tyr labelled with $Ru(Me_2bpy)_2(phen)$ in 100 mM sodium phosphate at pH 7.0.

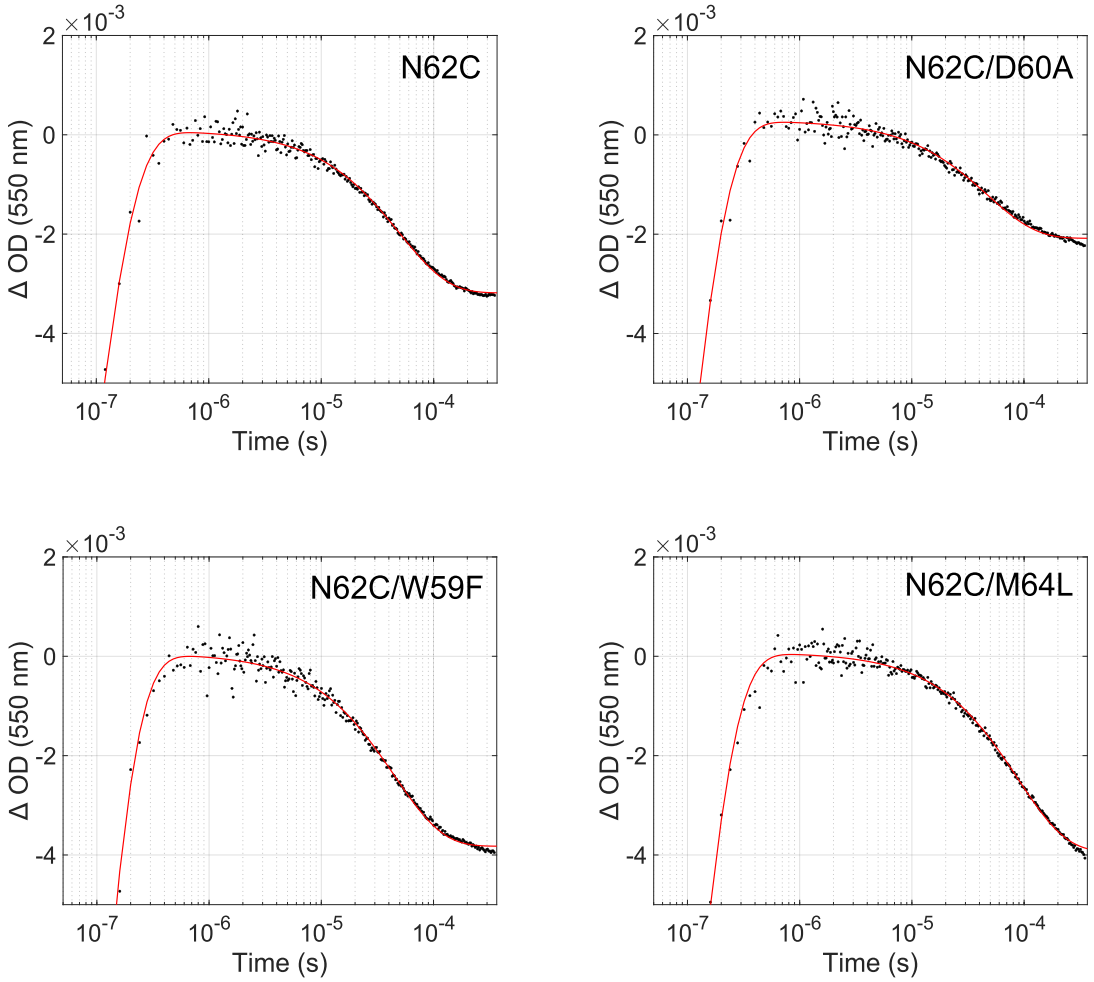

Figure B.34. Transient absorption traces (550 nm) for Fe(II) oxidation in (2,2´-bipyridyl)$_2$(5-cysteinyl-1,10-phenanthroline)Ru(II)-modified yeast iso-1 cytochrome *c* variants. Buffered in 100 mM sodium phosphate at pH 7.0 with biexponential fits (red line).

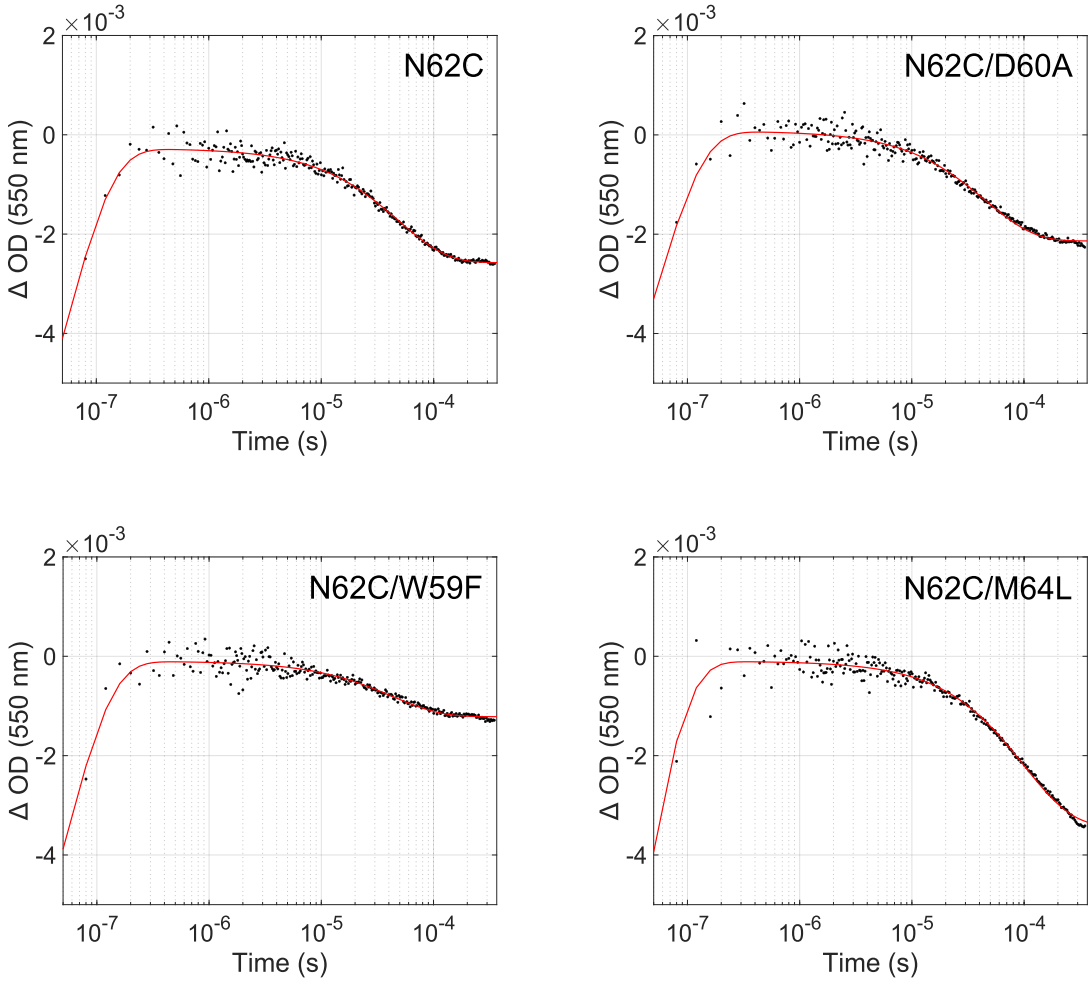

Figure B.35. Transient absorption traces (550 nm) for Fe(II) oxidation in (4-4´-dimethyl-2,2´-bipyridyl)$_2$(5-cysteinyl-1,10-phenanthroline)Ru(II)-modified yeast iso-1 cytochrome *c* variants. Buffered in 100 mM sodium phosphate at pH 7.0 with biexponential fits (red line).

Appendix C.

Supporting information for Chapter 4

Table C.1 Primers for azurin mutants.

Mutation		Sequence (5' → 3')
Az_STOP	Forward	CTGAAATAAAGATCCGGCTGCTAACAAAGC
	Reverse	GCAGCCGGATCTTTATTTCAGAGTCAG
Trp48TAG	Forward	CAACTAGGTTCTGTCCACCGCGGC
	Reverse	GAACCTAGTTGTGACCCATAACGTTCTTCGG

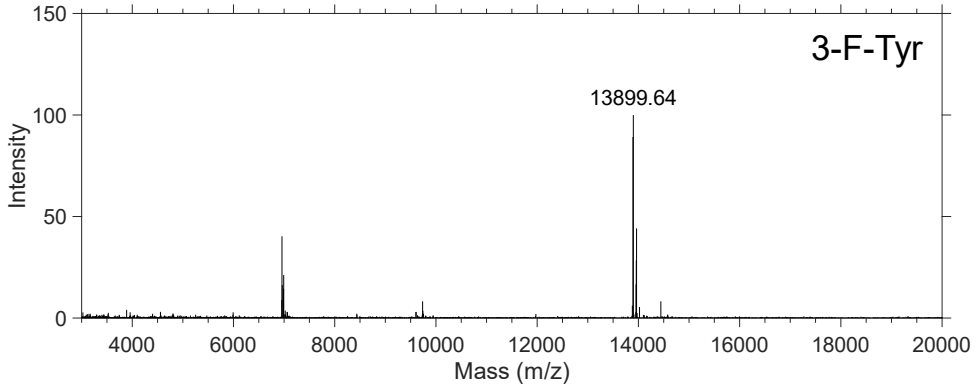

Figure C.1. MALDI-TOF mass spectrometry of azurin Trp48-(3-F-Tyr). Expected mass: 13900 Da; observed mass: 13900 Da.

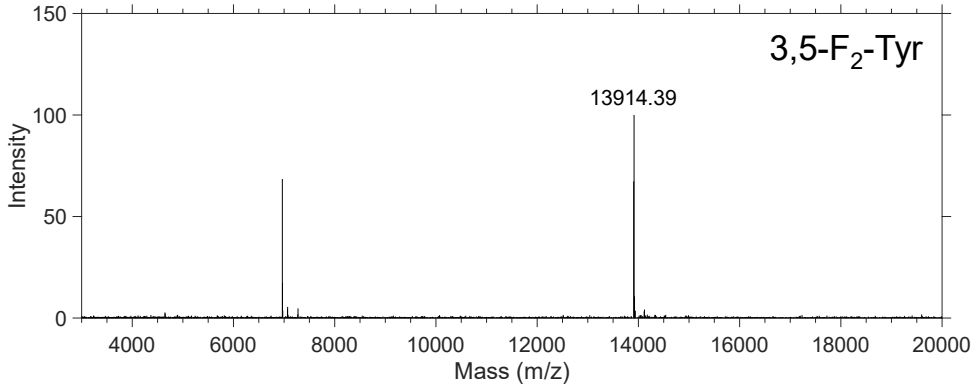

Figure C.2. MALDI-TOF mass spectrometry of azurin Trp48-(3,5-F_2-Tyr). Expected mass: 13918 Da; observed mass: 13914 Da.